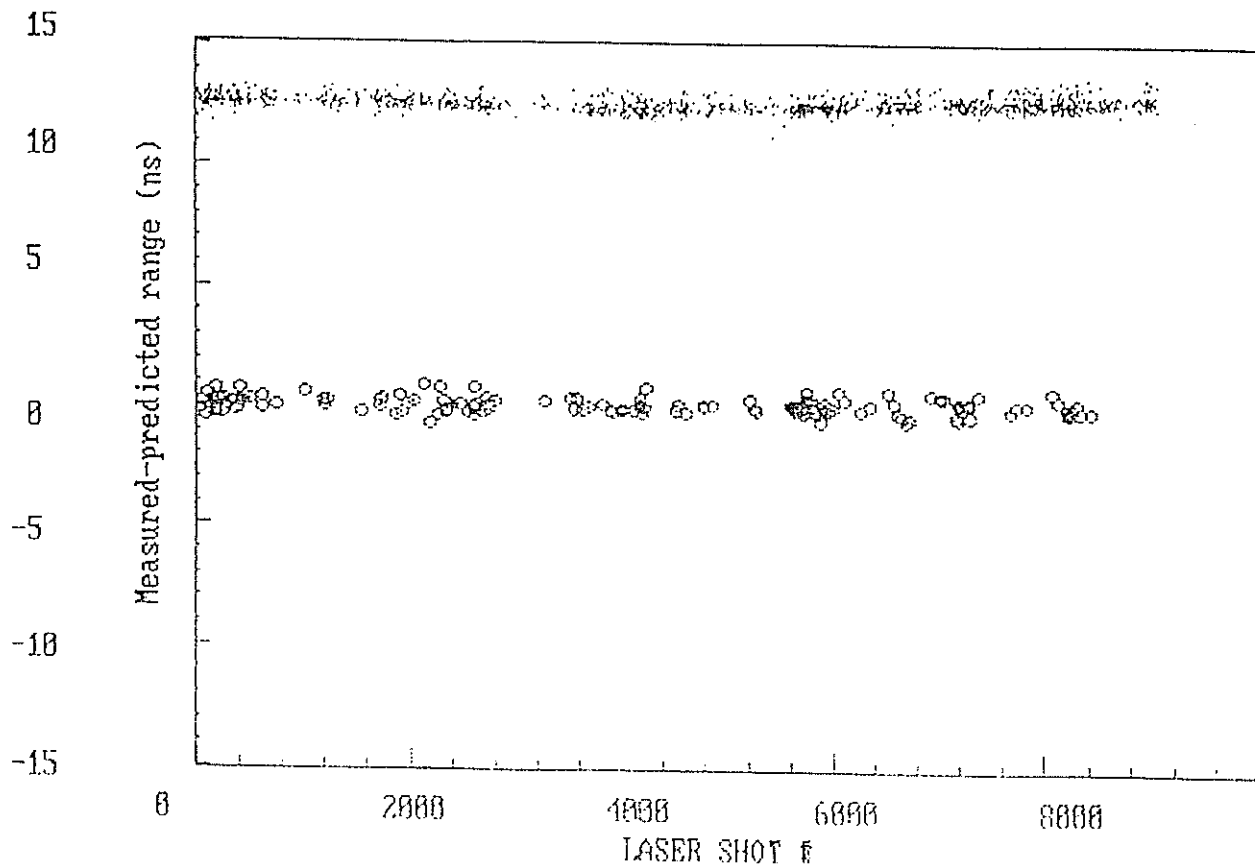**Figure 2a:** Satellite Ranging Results, 532 nm [upper trace] and 1543 nm [lower trace]. Lageos 2 satellite, mean distance 6000 km,

Figure 2b: Satellite Ranging Results, 532 nm [upper trace] and 1543 nm [lower trace]. Ajisai satellite, mean distance 2000 km.

Timing Devices

and

Calibration

Instrumentation Development and Calibration for the Matera Laser Ranging Observatory

Tenth International Workshop on Laser Ranging

Shanghai Observatory, Chinese Academy of Sciences

November 11-15, 1996

AlliedSignal Technical Services Corp.
Charles Steggerda, C. Bart Clarke, J. Michael Heinick, David McClure,
Michael Selden, Ray Stringfellow,

Italian Space Agency (ASI)
Dr. Giuseppe Bianco

Abstract

Three instruments are being developed for use with the Matera Laser Ranging Observatory (MLRO). These are: an event timer with picosecond resolution and less than 5 picosecond RMS jitter (after calibration), an eight-channel range gate generator with 20 picosecond resolution, and an eight-channel peak amplitude measurement device with 1 GHz bandwidth for each channel. These have been integrated with a calibration assembly to form the heart of the MLRO data measurement system. Initial results from testing of the event timer and range-gate generator will be described here. The peak amplitude detector prototype is still under development and no test data are yet available; however, its design properties will also be described here.

The MLRO system design required three instruments with performance not commercially available. These were an event timer with picosecond level resolution and accuracy to support time interval measurements to most SLR / LLR targets, a multi-channel range gate generator capable of providing range gate and simulation signals that can change dynamically at a high rate, and a multi-channel peak amplitude measurement device to allow for real-time laser diagnostics and modeling of amplitude-dependent systematic errors.

Event Timer

The event timer project was started in 1995. The development has been divided into two main phases: 1) the prototype development phase, which focused on developing a single-vernier prototype unit, and 2) the commercial instrument phase, currently in progress, which will result in a commercial-quality unit capable of supporting from one to four parallel verniers. Phase two will be completed by late spring 1997.
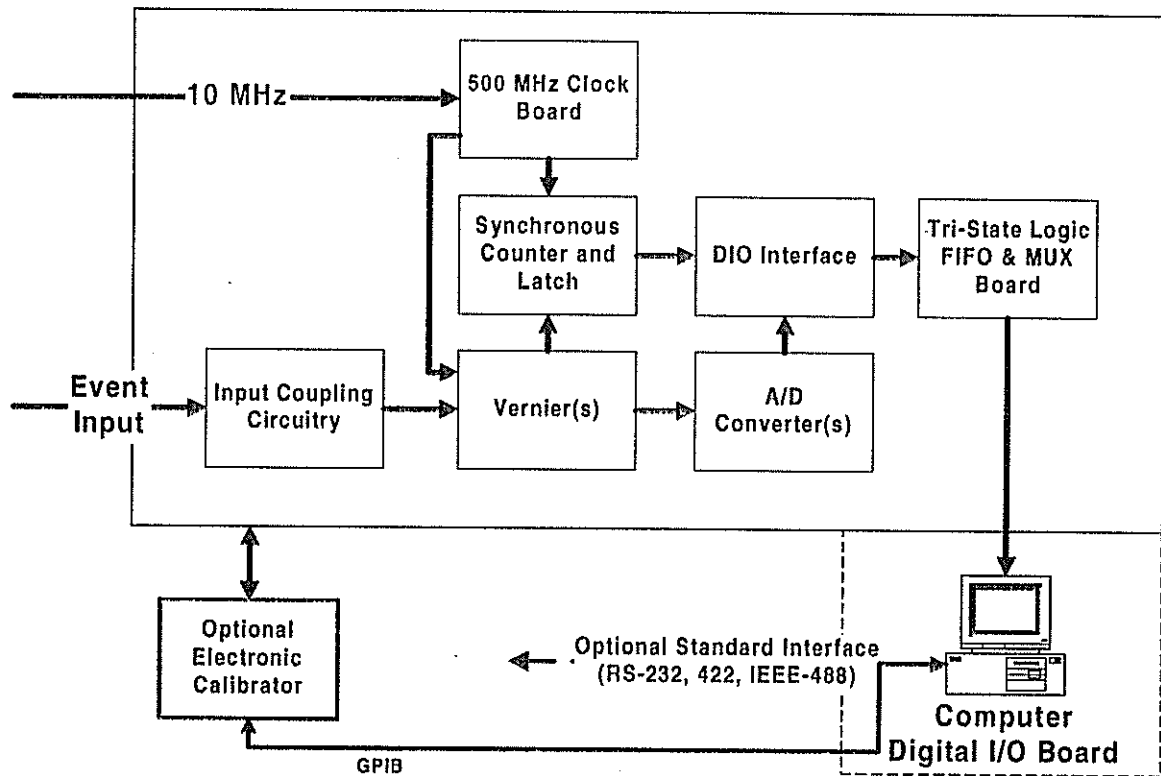
Figure 1: Event Timer Block Diagram

Event Timer Functional Description

A block diagram depicting the event timer as it will be offered in Figure 1. The event timer has been designed using predominantly ECL logic. It requires a high-quality 10 MHz input from a Cesium, Rubidium, or disciplined quartz standard. The event timer uses this input frequency to develop its internal 500 MHz clock. The internal clock drives a 26-bit synchronous counter resulting in a coarse count of 2 ns.

When an input event is received by the event timer, the vernier sweep is started and a synchronizer circuit is activated to select out the second 500 MHz pulse after the event. The selected 500 MHz pulse is used to sample the sweep for the A/D converter and to latch the count of the 26-bit synchronous counter. The resultant data from the two measurements provides ephemeris data with a resolution (for one vernier) less than 2 ps. The measurements are stored in 512-deep FIFO storage to be read by the computer. The system is capable of reading data at a 10 MHz rate until the FIFOs overflow. The speed of data flow is thus dependent on the computer I/O transfer speed, which is currently in the multi-kHz rate. Each vernier provides a measurement for each event, thus for 4 verniers the resultant resolution is 500 femtoseconds.

The event timer and its software are designed to allow for calibration of the small non-linearity of the vernier sweep. The MLRO system is equipped with an optical calibration and diagnostic assembly capable of modeling and testing the small non-linearity of the event timer vernier sweep. An electronic calibration assembly will be available (as an option) with the event timer to allow for automated calibrations.

Event Timer Features and Characteristics

Clock Speed (Internal)	500 MHz, 2 Nanosecond course counter
Channels	1 This is a single-stop event timer which uses the same electronics to measure each event. It can measure events in bursts of up to a 10 MHz rate.
Resolution	Better than 2ps per vernier, for a 4-vernier event timer the resolution is 500 femtoseconds.
Dead-Time	100 Nanoseconds (Minimum time between events measured)
RMS Jitter	Conservatively <10 picoseconds / vernier, however the vernier is capable of measurements of 3 to 4 picoseconds RMS jitter per vernier if calibration is provided. For a 4-vernier event timer we expect to see a 2-fold improvement of this number.
FIFO Depth	512 events can be stored internally to the event timer before being read by the computer.
Interface	Application-Dependent (Parallel I/O, IEEE-488, or RS-232)
Software	Measurement, Calibration, and Diagnostic software available for UNIX, MS Windows.

Event Timer Testing

The event timer testing has taken place in several stages using several techniques in both synchronous and asynchronous modes.
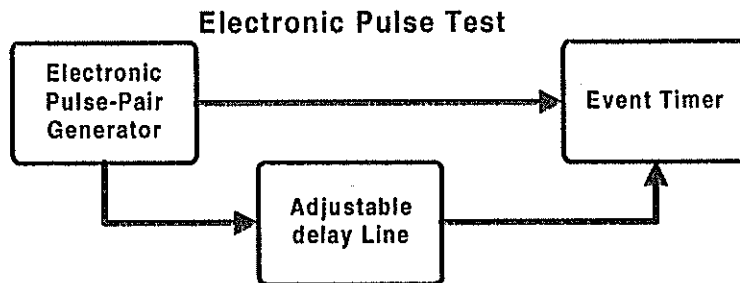

Figure 2: Event Timer Electronic Signal Testing

Electronic Signal Testing

The electronic signal testing is done in a synchronous fashion. One of the 500 MHz ECL clock signals is transmitted through an adjustable electronic delay line under computer control. A number of samples are taken at the various delay-line positions (delay-values). These allow us to map the linearity of the sweep signal over the 2 nanosecond dynamic range used for the measurement and to determine the single-event measurement jitter. This technique is the simplest test used and is especially effective for mapping the sweep linearity since it involves no external error sources.
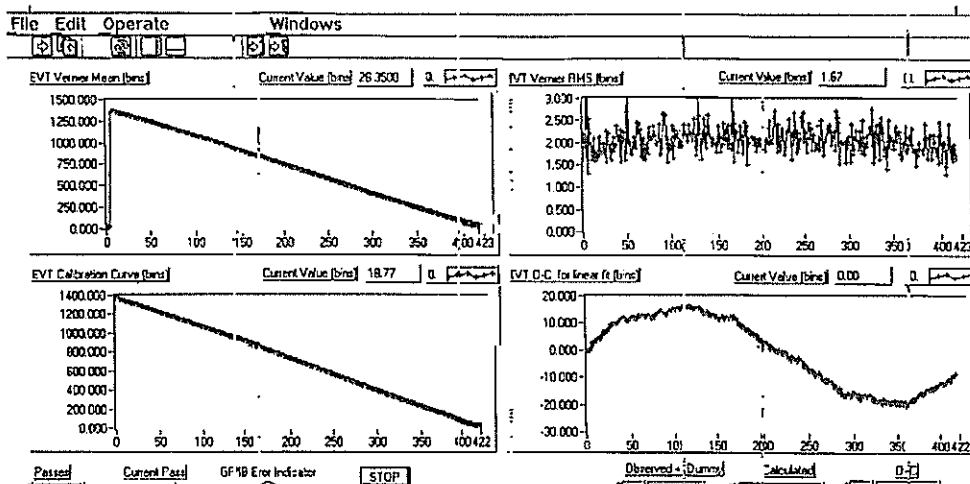
Figure 3: Event Timer Vernier Calibration Screen-Dump

The salient features of Figure 3 are the calibration offset and the RMS jitter. The lower right-hand panel displays the offset of the vernier measurement from the calculated range. The y-axis units are "bins" which represent a single bin-change of the vernier A/D converter truncated by the software (about 2 picoseconds). The upper right-hand panel displays the RMS jitter of the same data described in the offset plot. Forty samples were taken at each point along the curve and there is no data filtering -not even 3-sigma.
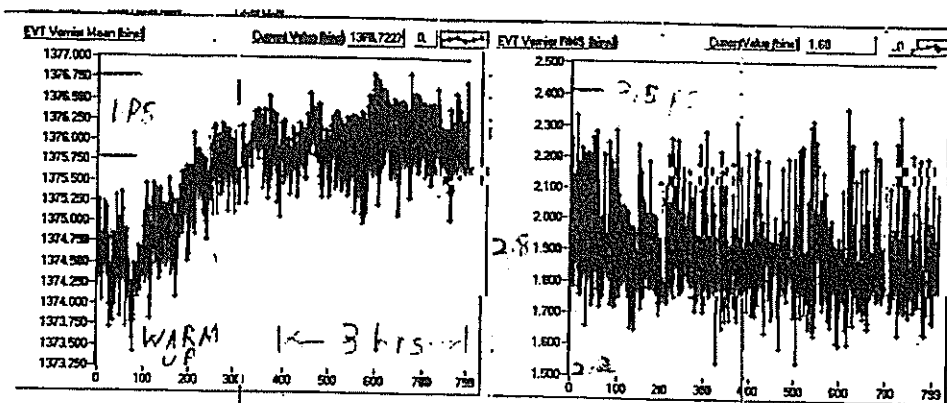

Figure 4 Screen-Dump from Event Timer Warm-up Stability Test

Figure 4 is a plot of the data acquired during a warm-up stability test. The most important features of this plot are the range stability plot (on the left) and the RMS jitter plot (on the right). For this test, the range measured was held constant and the event timer was switched-on from a cold start. The data were acquired over a six-hour period and 500 samples were taken for each plotted data point. The left-hand plot shows an increase in measured range as the event timer was warmed-up over a three-hour period. The total change in the measured value was less than 3 picoseconds. After the first three hours (the warm-up period) the measured range was stable. A hand-drawn pair of lines on the plot provides a scale factor of 1 picosecond. The right-hand panel shows the RMS jitter of each of the 500-point samples. Hand drawn figures indicates the scale where the y-axis

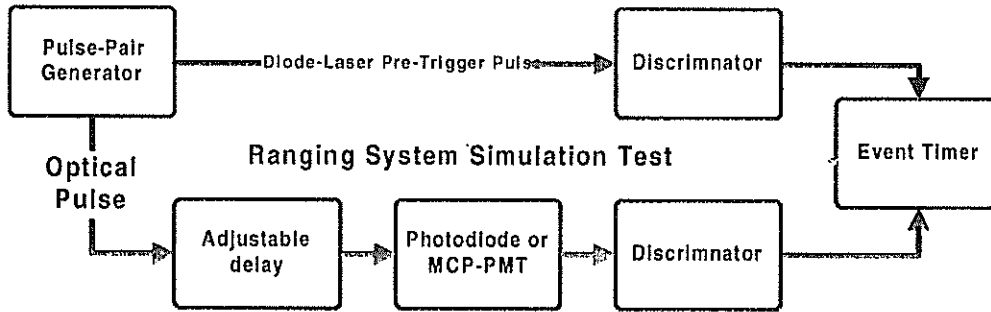value is 2.2 picoseconds and 3.5 picoseconds. The average RMS value was less than 3 picoseconds for the test.

Figure 5: Optical Test Set-up

Optical Signal Testing

Optical signal testing is asynchronous and closely simulates the mode of operation experienced during laser ranging. A diode laser is used to provide a pair of pulses. The first pulse is generated by the diode laser electronics and is used to fire the diode laser. This pre-trigger signal (a simulated "start" event) was processed through a tennelec (Oxford) discriminator to provide an input signal consistent with the expected "stop" event; it was then coupled to the event timer. The diode laser optical pulse was sent through a computer-controlled optical delay, then coupled to an optical detector. The detector output signal was processed by a second discriminator channel, then coupled to the event timer. The Diode laser contributes 5 picoseconds of RMS jitter and the discriminator contributes about 7 picoseconds RMS jitter.
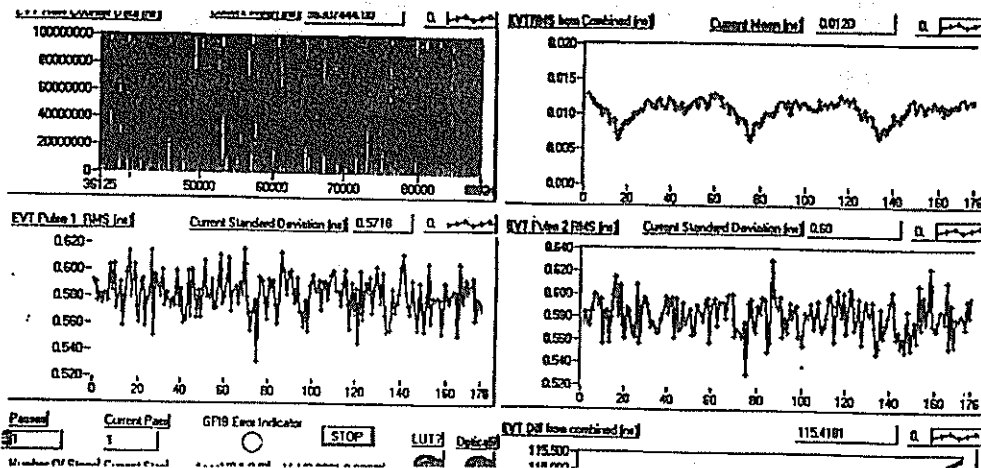

Figure 6 Event Timer Asynchronous Optical Test

Figure 6 shows an event timer test using an optical diagnostic cycle. For this test, the optical calibrator provides a series of different ranges under computer control and the event timer is used to measure the changing range. Each point represents one position and

500 samples. The most important panel of this screen-dump is the upper right-hand plot which shows the RMS jitter for the entire measurement system. For this test a rough (obsolete) calibration file was used and the resulting episodic pattern of the RMS jitter (between 6 ps and 12 ps) is a result of an obsolete calibration. The RMS jitter on this plot achieves a minimum when the point of the vernier sampled for the start signal is identical as the point sampled for the stop signal. Under these conditions (2 nanoseconds - or 1 clock-cycle apart) there is no calibration required to achieve maximum accuracy. This panel is representative of one of the types of diagnostics available for the event timer. This test provides data to show when it is necessary to recalibrate the event timer. A decision to recalibrate is based on a pre-determined threshold of error tolerance.
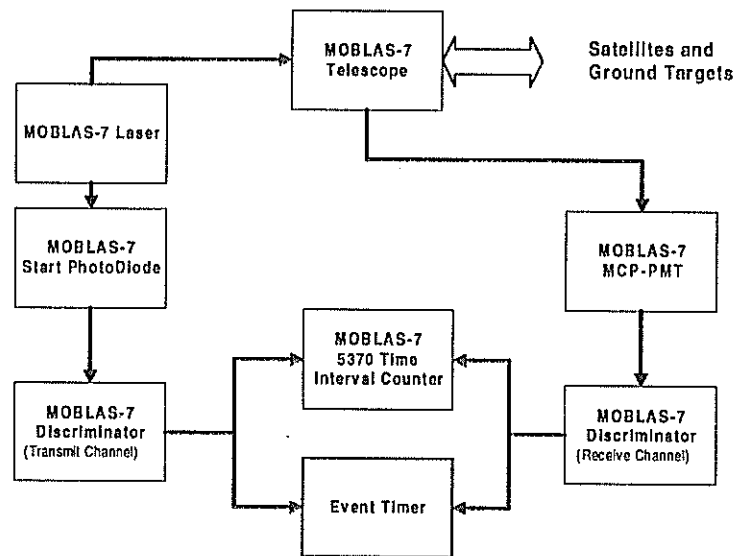

Figure 7 Event Timer SLR Testing

Satellite Laser Ranging Testing

Regardless of successful results from laboratory testing, the true test of an instrument or system is how it behaves in actual operations, rather than laboratory simulations. To provide a good understanding of the event timer performance, we placed the prototype into MOBLAS-7 as illustrated in Figure 7 and connected it in parallel with the operational HP5370 time interval unit. A number of satellite passes and ground target data were collected over a period of a week (on a periodic non-dedicated basis). Throughout the tests no calibration data were applied to the event timer; no corrects were made for systematic non-linearity of the vernier sweep circuit. A pure linear sweep was assumed through the sweep interval.

A summary of the results for the event timer SLR testing is shown in Figure 8. The event timer resulted in a 30% to 40% improvement in the overall single-shot RMS jitter for those satellites that were tracked. This feature can also be seen in Figure 9, which shows a comparison of the data scatter between the HP5370 and the event timer using single-shot residual plots for a LAGEOS-1 pass. The MOBLAS-7 counter data showed a 9 mm RMS jitter while the event timer measured a 5 mm RMS jitter. Figure 10 shows that the event

timer and the HP-5370 agree on the value of the range measurement. The scatter of the data is limited by the HP-5370 random error (jitter). Although there was also a significant improvement for ground target data, the overall improvement was masked by the MOBLAS-7 operational procedures. The operators deliberately vary the amplitude of the receive signal using an adjustable neutral-density filter wheel to simulate the full range of signal amplitudes experienced during ranging. This operational procedure results in a variable range dependent on the received amplitude. However, when the calibration data were divided into time-sequenced segments, the improvements became more evident.
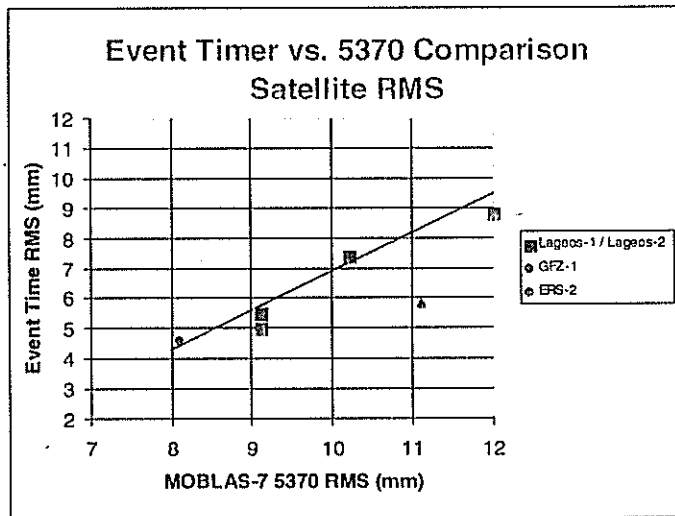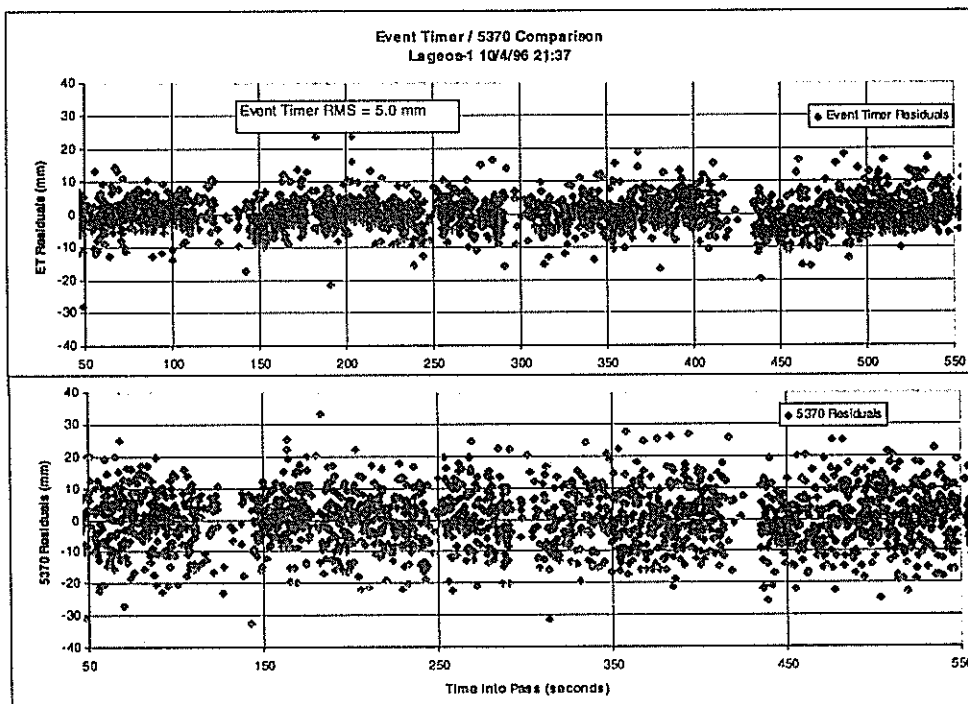

Figure 8 Summary of Satellite Laser Ranging Results

Figure 9 Shot-for-shot comparison of HP5370 and Event Timer SLR data for a LAGEOS-1 pass
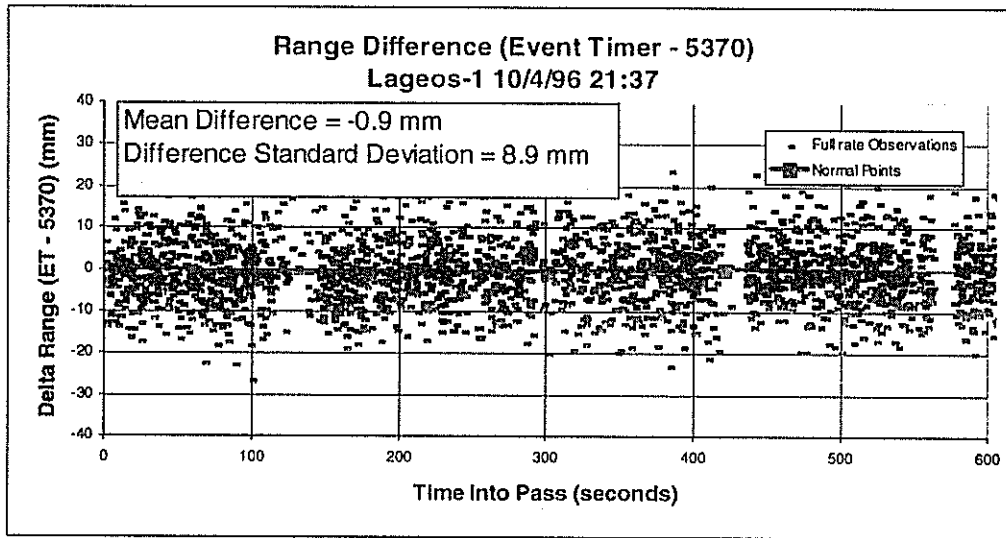
Figure 10 Plot of the bias range between the HP5370 and the event timer

Range-Gate Generator (RGG)

The range-gate generator has been developed to provide signals for gating and simulation. The MLRO will be equipped with two RGG units. A block diagram of the RGG is illustrated in Figure 11. The unit is provided a 10 MHz clock and a beginning-of-frame signal. Data for the next frame is loaded from the computer during the current frame. When the frame-clock signal is received by the RGG unit, the data is latched to the counter and verniers and the various channels each count until they reach their assigned time delay for 1) the start-of-pulse then 2) the stop-of-pulse. This allows for eight independent pulse delays and widths each frame from each RGG unit. The computer software determines which channels must receive start and/or stop signals each frame. This method allows for gating and simulations with ranges and widths varying each shot up to Multi Mega-Hertz frame-rates, only limited by the speed of the computer and its digital interface.
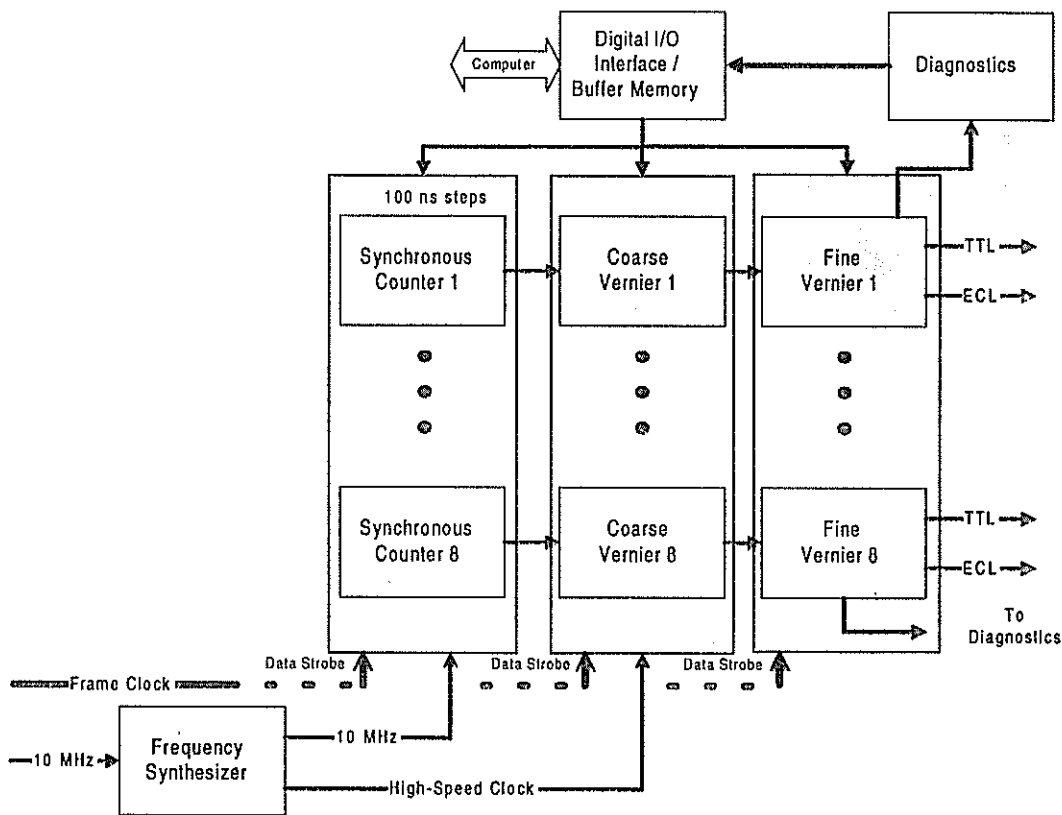
Figure 11: Range-Gate Generator Block Diagram

The RGG unit is equipped with an internal diagnostic circuit to check for the functionality of each channel upon request by the computer. Each of the vernier channels outputs both a TTL and ECL pulse each frame. The user may select which pulse is needed for a particular channel. The RGG

Range-Gate Generator Characteristics

Clock Speed (Internal)	250 MHz
Channels	8 Independent Channels with independently variable range and pulse width.
Resolution	20 picoseconds (leading edge), 500 ps (trailing edge)
Range	20 ns to Infinity (under computer control)
Output Levels	TTL, ECL
Maximum Repetition Rate	10 MHz (or limited by computer interface)
RMS Jitter	< 50 ps
Interface	Parallel Digital I/O, Can be provided with a PC for standard interfaces
Software	Measurement, Calibration, and Diagnostic software

Peak Amplitude Detector

The peak amplitude detector (PAD) is being developed to allow the MLRO system to calibrate and model amplitude-dependent systematic errors in the ranging data. In addition

to improving the data accuracy, the PAD will support real-time diagnostics of the laser and transmit/receive optics alignment.

The PAD is designed contains eight channels, each with a 1 GHz bandwidth. Each channel will measure the peak amplitude of a pulse with eight-bit resolution. The channels will be periodically calibrated using a 1 GHz waveform digitizer. Each channel also contains flags to indicate over-range and under-range values. The PAD is currently in the prototype development stage.

Summary

Three instruments are being developed for use with the Matera Laser Ranging Observatory (MLRO). These are: an event timer with picosecond resolution and less than 5 picosecond RMS jitter, an eight-channel range gate generator with 20 picosecond resolution, and an eight-channel peak amplitude measurement device with 1 GHz bandwidth for each channel. As part of the development process ATSC is thoroughly testing each unit to ensure that the instruments indisputably meet or exceed their design

MultiCounter Operation at SLR Graz

G. Kirchner, F. Koidl
Institute for Space Research / Austrian Academy of Sciences
Observatory Lustbühel; A-8042 GRAZ / AUSTRIA

1.0 Introduction

In the process of measuring distances to satellites with lasers, we found that at the moment the Time Interval Counter is the weakest point; the jitter contribution to the overall measurement jitter is the highest of all single elements, and there are essential bias problems hidden in counter non-linearities and counter temperature drifts, which are difficult and tricky to detect with a single counter. We therefore added additional SR620 counters - we were happy to have access to 3 pieces - to our HP5370A, operating them all in parallel (Fig. 1).

2.0 Hardware Setup for MultiCounter Operation

Instead of using only our old HP5370A counter to measure the time of flight of the laser pulse, we added up to 3 additional SR620's, connected just parallel to the HP5370A; all of them are thus measuring the same time interval (Fig. 1). All counters are supplied with identical start and stop pulses, which are generated with ultrafast comparators; this also ensures constant pulses (duration, amplitude, risetime etc.) for the counter inputs.
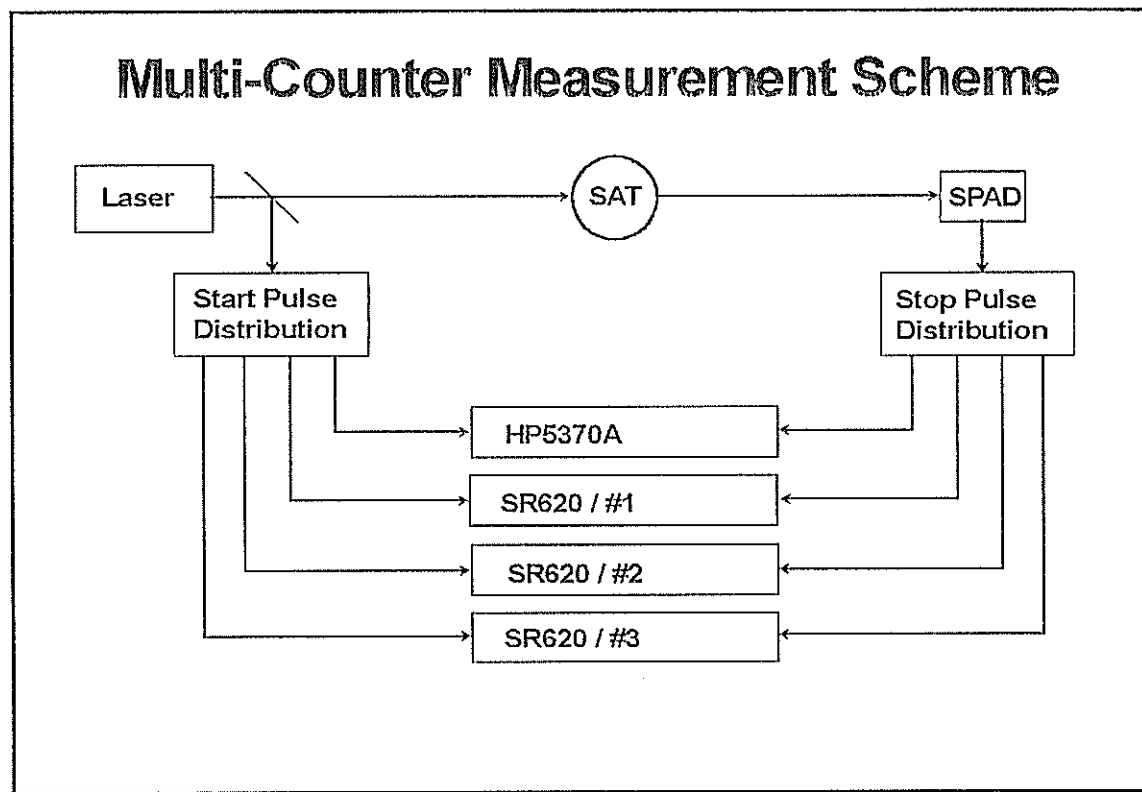

Fig. 1: Hardware Scheme for MultiCounter Operation

Although all counters get similar signals, and are measuring the same time interval, the results are different: the offsets between the counters are in the order of some Nanoseconds, due to non-identical trigger levels, different sensitivity of inputs etc.; this is no problem for Single-Counter-Operation (it is part of the calibration), but has to be handled with multiple counters. In addition, these offsets are not constant; their values are changing due to different temperature effects, cable or setup changes etc. We therefore decided to evaluate all relevant counter offsets automatically during calibration, ranging and post-processing.

In calibration, the result of all 4 counters are stored for each shot; after getting the desired number of valid target returns (usually 500), the differences between the HP5370A and the SR620's are calculated for each shot, averaged, and smoothed (iterative Sigma elimination); with the resulting mean offsets of the Stanford's with respect to the HP5370A, all Stanford results are corrected; for each shot, we then calculate the mean value of all counters; these values are then used for evaluation of the calibration constant.

One of the counters (SR620/#1) showed a typical non-linearity of almost 150 ps in a limited range (Fig.2); if the routine calibration would be done with this counter only and in this range, the calibration would result in a - difficult to detect - bias of more than 2 cm.

Due to such non-linearity problems, it would also be dangerous to use only valid target returns for counter offset determination; we therefore use ALL recorded points, including the intrinsic noise stops of the SPAD (covering a range of up to some ten μs), for this counter offset determination procedure.

COUNTER NON-LINEARITIES

Counter Differences [ps]

GRAZ Calibration Value: 206.500 [ns]

HP5370A - SR620/#1
HP5370A - SR620/#2
SR620/#1 - SR620/#2

SR620/1 has
a 150 ps big
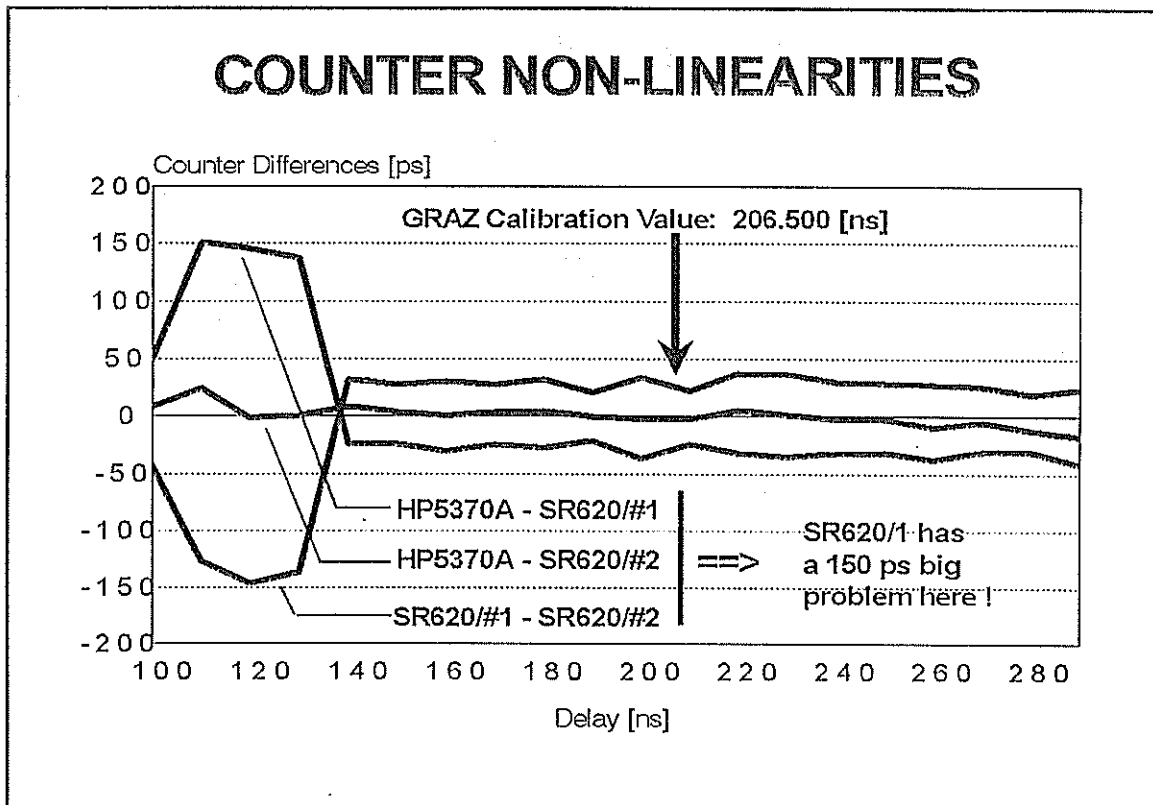problem here !

Delay [ns]

Fig. 2: Non-Linearity of SR620/#1

All counter offsets and corresponding RMS are stored and kept in log files for later access, checks, and comparison with similar counter offsets calculated during post-processing.

During actual ranging, the readings of all 4 counters are just stored on disk, without doing any calculations, offset determination etc. To form the residuals required for the real-time-display, return identification etc., it is sufficient to use the result of one counter only.

In post-processing, the program mainly performs the same sequence for counter offset determination, as in the calibration program: It reads all stored counter values, determines all offsets of the Stanford's to the HP5370A, averages and smoothes them, and subtracts these offsets from each single Stanford reading; then, for each return, the mean of all counters is calculated, which is then used for all post-processing. Due to the wide spread of measured time intervals (over the full range of each satellite pass), any non-linearities are more or less eliminated, and have almost Zero influence on offset determination.

As in the whole Graz software, theMultiCounter operation is made as flexible and easy to handle as possible; the number of counters to be used for any program is defined in an ASCII setup file; this makes it easy to add or remove additional counters. For each counter, there is also an ASCII setup file, where all specific programming codes are defined; thus it is easy to change/optimize e.g. trigger levels etc.

4.0 Experiences and Results with MultiCounter Operation

As example of another single counter problem, which was easily identified with the MultiCounter
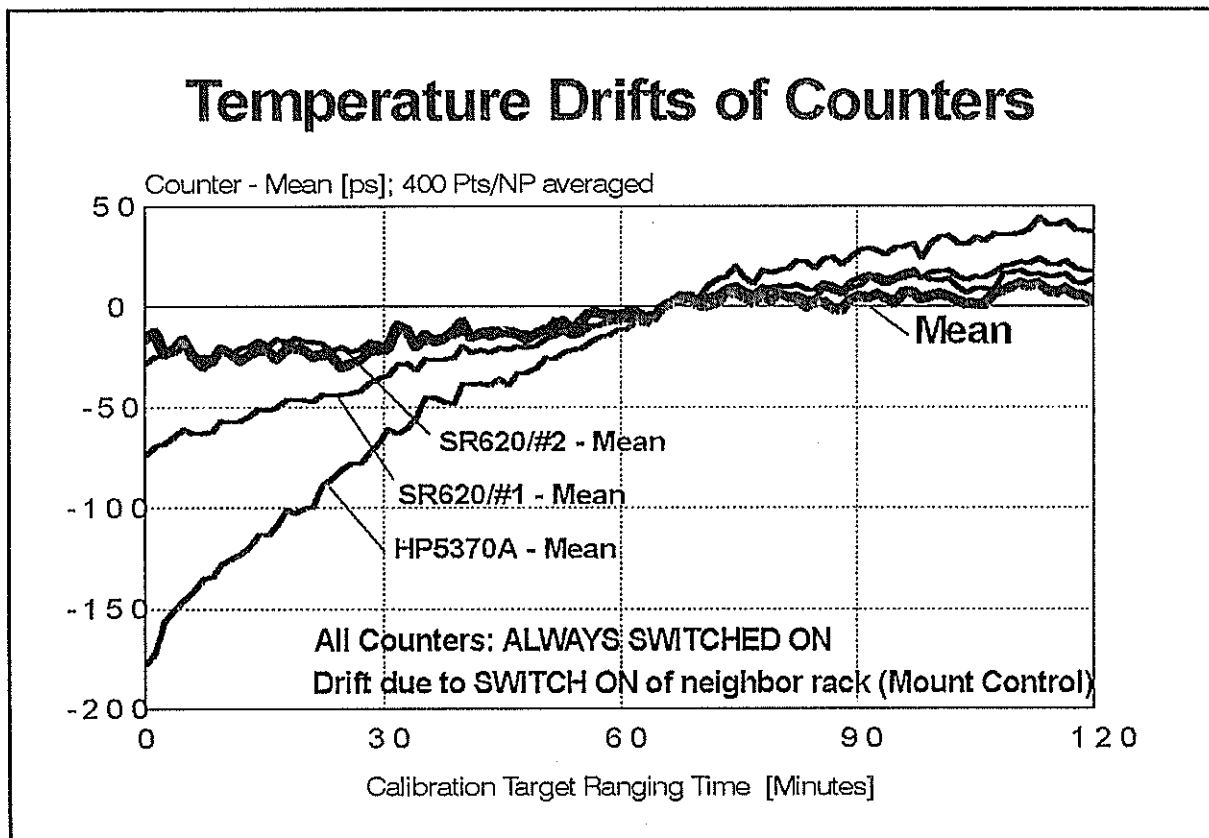

Fig. 3: Temperature drift of HP5370A, identified with MultiCounter Operation

operation, Fig. 3 shows a temperature problem of our HP5370A; although operated in an air-conditioned environment, the switching ON/OFF of the neighbored mount electronics rack at begin and end of ranging sessions caused a slow change of the counters cooling air temperature of up to 4° C (within 1 or 2 hours); this caused a corresponding drift of about 200 ps (more than 3 cm in range!) of the HP5370A measurements; although the major part of such a drift is eliminated by pre-/post calibrations, small portions of this error always remain, and are in general highly undesirable.

Another - more tricky to detect - problem was identified also with the MultiCounter system; as mentioned above, all counter offsets - evaluated in calibration and ranging/post-processing - are stored in log files; as there is no change in setup between calibration and ranging to all satellites, all corresponding counter offsets should give the same values; however, there appeared a significant difference between low satellites and LAGEOS (Fig. 4).
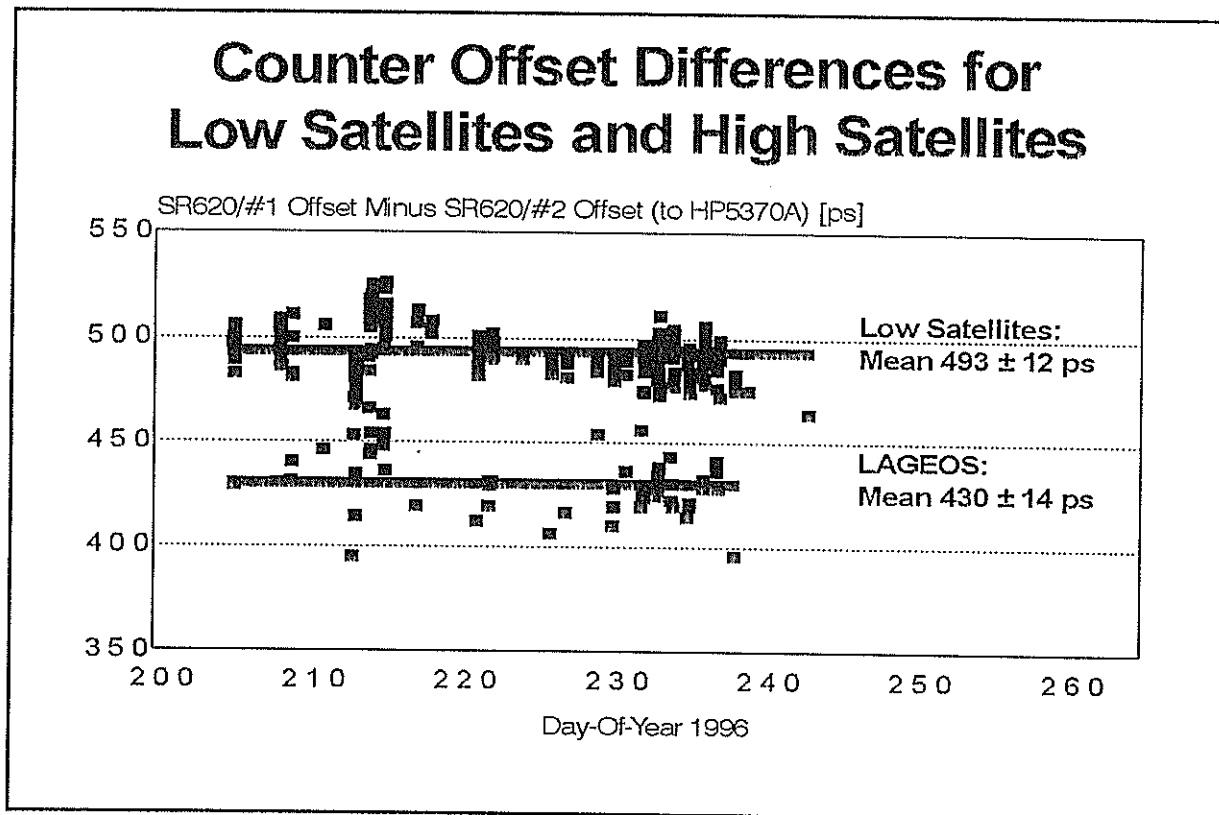

Fig. 4: Counter Offset Differences for different satellites: Should be the same ....

After some more tests we found the reason (although not the explanation): We always used some form of daisy-chaining to supply the external 10-Mhz frequency to the counters; with the single counter system (HP5370A only) of last years, we supplied our range gate generator (HP5359) with the external 10 Mhz, and used its output (its internal quartz oscillator, slaved to the external reference) as external frequency source for our HP5370A. With the MultiCounter system (up to 4 counters), we supplied the first counter with the external 10 Mhz, using its slaved quartz oscillator output for the next counter, and so on. This caused a variable bias in the whole LAGEOS range (38 to 60 ms) of up to more than 2 cm, for the first counter; for the second

counter, the effect was smaller; for the next counters, it disappeared; for the low satellites range (5 to 15 ms), these effects were much smaller.

Realizing these problems (although we still do not have an explanation), we started to supply each counter with its own, independent, external frequency source (October 1996); as a preliminary result, the SLR Graz range bias, as published by the University of Texas, changed significantly [1]: Before October 1996, it was unstable, and ranging from -20 to -30 mm; since October 1996, it is more or less fixed at -13 mm, with weekly variations of less than ± 2 mm.

In conclusion, we found the following advantages of using multiple counters to measure the time-of-flight:

- Any possible biases caused by a single counter are detectable, can be minimized or can be avoided completely with a MultiCounter system;
- The improvement in Single Shot RMS is significant (Fig. 5); including our Automatic Time Walk Compensation Circuit, we get now below 5 mm RMS from ERS-2;
- Compared to the total cost of the SLR station, or to the cost of currently developped epoch timers, the cost of MultiCounter operation is relatively low, fully scalable, and helps to avoid or at least to minimize all - possibly undetectable - bias problems;
- Due to a flexible software, it is easy to install or remove - borrowed - additional counters.
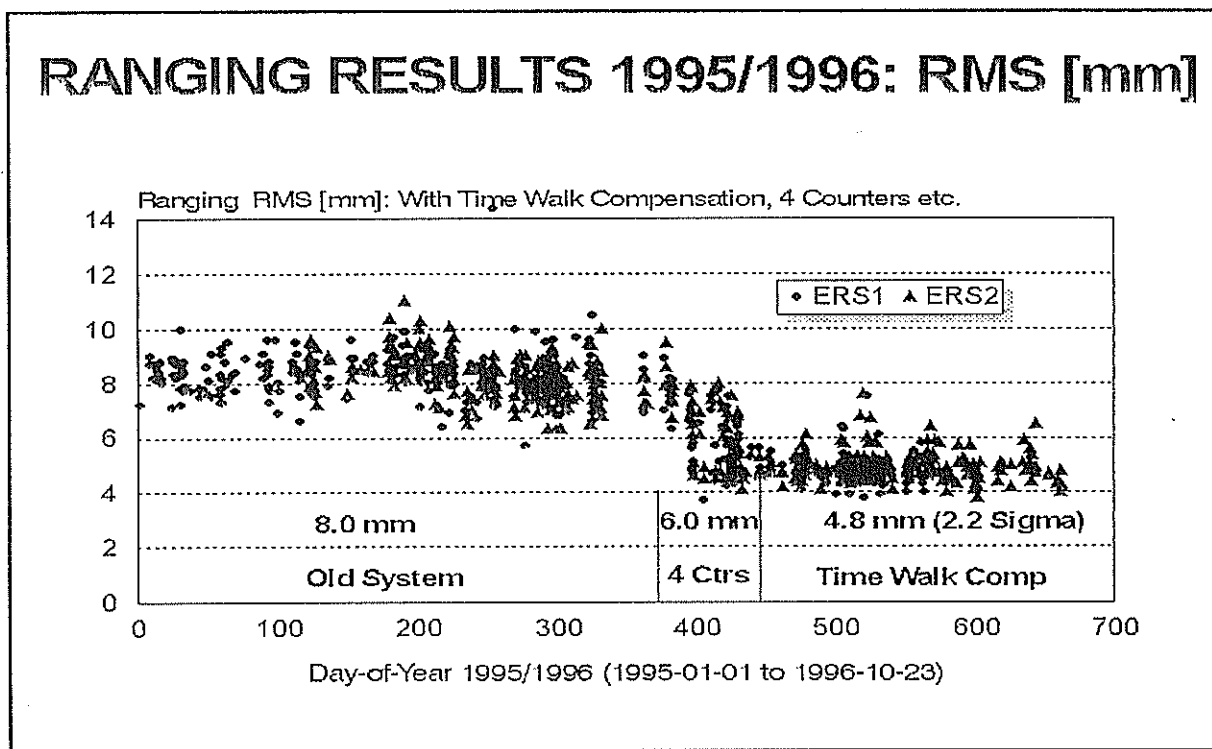

Fig. 5: Single Shot RMS Improvement of ERS-Ranging, using MultiCounters etc.

References:

[1]   EUROLAS Cluster Stations: Bias Workshop Results. G. Kirchner, F. Koidl; in these Proceedings.

Femtosecond Timing of Electronic Pulses for SLR

Ben Greene, Leigh Dahl,
Electro Optic Systems Pty Limited, Australia
Josef Kölbl
Electro Optic Systems Gmbh, Germany

Abstract

A system methodology for the electronic timing of pulses with 100 femtosecond resolution and 300 femtosecond accuracy is presented. The calibration and timing systems to achieve such performance are also discussed.

1. INTRODUCTION

Advanced technology componentry provides significant benefits to the performance of electronic timing systems. Electro Optic Systems (EOS) has developed new products which supersede the traditional timing systems and their architectures, and these are now being incorporated into our Satellite Laser Ranging systems such as the Keystone network in operation in Japan. Work is currently being undertaken which should take the performance of such timing systems below the picosecond threshold before the turn of the century. Timing system development at EOS has achieved the performance levels shown in Table 1.0. Current developments will soon produce systems for electronic timing of pulses with 100 femtosecond resolution and 300 femtosecond accuracy.

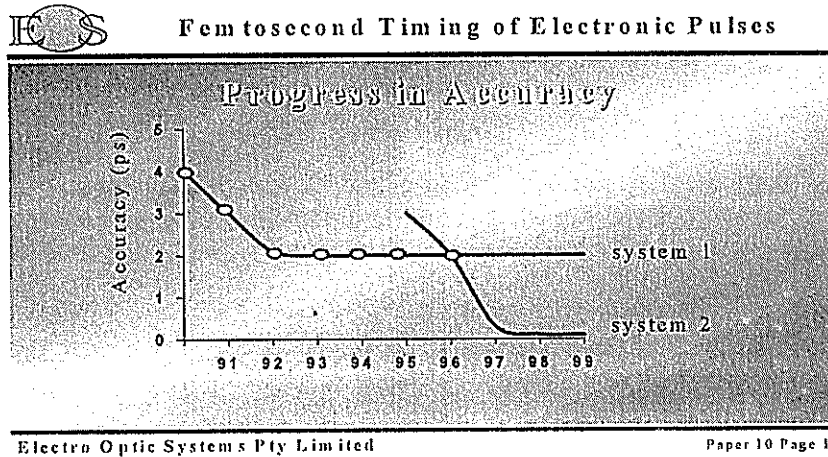|		1985	1990	1995
Precision	(ps)	40	20	10
Accuracy	(ps)	6	2	2
Stability	(ps/hr)	5	1	1

Table 1.0 : Progress in Electronic Timing Systems

Although the terms referred to in the table above are commonly used by the SLR community, it is important that they are clearly understood. The **accuracy** of a laser ranging measurement is the *absolute correctness of a measurement* which is an error term defining the difference between the true range and the measurement obtained. The **precision** is a parameter describing the error distribution of a set of samples, usually the standard deviation of a Gaussian distribution. It is used specifically to define the distribution of individual measurements relative to their mean and is dependant on the measurement resolution and stability. The measurement accuracy of the single sample will comprise of the summation of the random errors described by the system precision plus the systematic range biases. The system bias will be produced from a combination of a number of system error sources with finite stabilities, and these will produce a deviation from an accurate value. The "jitter" of a timing pulse is a reflection of the signal noise, and this parameter can be quantified from an analysis of the standard deviation of a signal's delay measurement. A list of the timing terms used in SLR is documented in the Appendix .

A timing system measurement precision can be improved by obtaining more samples, but this compromises the effective data rate of the system. To achieve the desired accuracy in realtime, the precision of the measurement must also improve down to picoseconds. Timing systems performance of this order, and simultaneous developments in the design of next generation

satellites, atmospheric modelling techniques and data analysis will give significant benefits to earth science and geodesy.

The following graph shows the predicted development path over the next three years ("System 2").

Femtosecond Timing of Electronic Pulses

Progress in Accuracy

Electro Optic Systems Pty Limited   Paper 10 Page 1

Such improvements will gained in electronic timing system performance and just as significantly the calibration standards by which they are measured, by advances in technology. In particular, by addressing design issues in the following areas:

- a reduction in parasitic and other effects by component size reduction in both die and package technologies

- improvements in the bandwidth of commercially available (low cost) electronic components

- thermal compensating techniques in real time microprocessing

- the close component tolerancing in readily available in low and high densities

- power supply stabilities which are achievable with better design practices.

2. TIMING OF ELECTRONIC PULSES

2.1 SOURCES OF ELECTRONIC SIGNAL JITTER

Jitter is a random displacement of a signal from its true location in time. These displacements can occur in amplitude, phase, and pulse width, and are generally categorised as either deterministic or random. Jitter results in a time-domain deviation of a repetitive signal generally following a normal Gaussian distribution. The deviation from the "ideal" or "true" time of an event is determined by the mean of the distribution. By considering jitter sources as incoherent, the total random jitter is calculated as the square root of the squared sums.

The jitter of a timing pulse measurement and hence the system precision, is a product of the electronic noise in the system. The source of this noise can be from the within the detector sources, the timing system, the system environment coupled through mechanisms such as the cabling, power supplies or any combination of the above. The result is a quantifiable uncertainty in the pulse time position for a single sample due to an electronic noise on either the signal itself or the threshold level on the electronic gate or component through which it passes.

Each of the electronic component elements in an electronic timing system have defined trigger level or threshold settings that are not infinitely stable, whether TTL, CMOS, ECL, or NIM. The noise on each threshold will contribute to the overall system jitter. As well as noise these thresholds are affected by environmental changes such as temperature, so it is desirable to minimise the uncertainty of these trigger thresholds by:

- minimising the number of critical path components ie. thresholds.
- reducing component noise by decoupling, regulation and filtering
- and maintaining fast risetimes on the transitions thereby reducing the probability time distribution of the uncertainty period.

This must be achieved without impacting on the performance through unwanted side effects such as increased RF noise levels. As well as the threshold noise any electronic circuit will have a noise produced from the resistive elements. These are well characterised as shot, Johnson, and flicker noise. The discussions and equations for calculating the noise from such sources is well documented in texts describing electronic design theory.

There are other causes of a signal jitter besides that of the threshold and signal noise. For example, the simultaneous switching of a circuit's outputs which induce a "ground- bounce" on the component and introduce an indeterminate offset in the resultant waveform. Metastability is another problem in logic design which is produced when asynchronous timing signals are presented to synchronous logic inputs. Other issues which must be considered are signal line reflections due to finite impedance matching tolerances, any impedance discontinuity in a circuit (such as Printed Circuit Board PCB tracking), signal under and/or overshot, cross talk, and electromagnetic interference.

Following examination of the issues identified above, the design engineer can set about to reduce the contributors of limited system performance, through application of RF and high-speed design techniques. The techniques which should be employed in system design include:

- the use of low impedance PCB grounding achievable with multilayer PCBs
- the use of differential signal drivers whenever possible
- controls on PCB design and fabrication to ensure the controlled matching of signal line impedances
- the use of low ohmic impedances hence a reduction in resistive noises
- the exclusive use of system components with low noise figures
- employing fast transitions and slew rates to minimise the jitter probability function

Miniaturisation in fabrication processes which lead to an integration and subsequent reduction in the size of the design also improve timing system performance. This is because medium scale integration (MSI) device designs do not achieve matched line impedance terminations without finite tolerances. They also have longer signal propagation delays and higher skew, which limits bandwidth and are subject to larger temperature dependencies. If the rise-time t_r of a pulse is less than twice the propagation delay of a track t_{PD} , then the track has to be terminated with the characteristic impedance of the line according to the transmission line theory:

$$t_r \leq 2 \cdot t_{PD}$$

As an example, consider the following: when transmitting a pulse with 100 ps rise-time the design requires a matched termination at the receiver end when it is transmitted along a PCB track as

short as 7.5 millimetres of length (for typical FR4 PCB material with $\varepsilon_r \approx 4$). Hence, circuit integration technologies should be employed in both the analogue and digital domains through high density programmable gate arrays, multichip modules (MCM), flipchip and, full-custom application specific integrated circuits (ASICs). This digital integration permits an increase in the clock frequency at the same time reducing the dynamic range of the analogue vernier component of the timing systems. Hybrid analogue design techniques not only reduces propagation delay and skew but allows for laser trimming of discrete components. ASIC and analogue hybrid technology does require an engineering investment, but by observing such issues and using general components with tight tolerances performance improvements can still be made.

The sources of signal jitter can be identified and categorised into different types, such as: synchronous modulated, asynchronous modulated, cycle to cycle, input/output, long term, and systematic jitter. Increases in the precision of the electronic timing modules can be achieved by reducing system noise from signal and thresholds and maintaining the rise and fall times in all electronic pulses. By using the maximum circuit bandwidth available for the transmission of these signals the probability of distribution of trigger uncertainty is reduced. The SLR range measurement error consisting of the measurement precision plus the systematic bias, can be reduced by minimising the electronic pulse jitter.

2.2 MEASUREMENT TECHNIQUES FOR QUANTIFYING CIRCUIT JITTER.

High bandwidth digitising and sampling oscilloscopes can be used to quantify the jitter inherent in an electronic circuit by using a test signal source which is repetitive in nature. These instruments use sequential repetitive or random repetitive sampling techniques to acquire the jitter histogram of the pulse. There are a number of vendors marketing equipment in the order of 10 Gsamples per second, for example LeCroy with the Model 9362, HP with the 54750, and Tektronix's CSA803. Jitter analysis equipment can also by utilised from the optical and RF communications fields. One such device is from the US company Wavecrest who have a dedicated jitter and pulse analyser (Models DTS2070 and DTS2075) for the time and frequency domain. This type of instrument is designed with the internal trigger jitter requirements which otherwise limit the measurement accuracy.

The time interval counters from Stanford Research Systems (SR620, SR625) which are commonly used in the SLR community also incorporate features to measure signal jitter. The internal jitter of the SR620 when used in time interval measurement mode with a signal risetime of 500ps is in the order of 20ps rms. Any such jitter measurement must also be analysed in terms of the statistical processes under which it was made and for any timing system be referenced appropriately back to the circuit input. This last point is important as the test signal used will also have a finite jitter which is not a part of the timing system under test and may vary from that used in ranging systems ie. Rubidium, Caesium or other high stability oscillator source.

3. Timing Circuit Calibration methodology

	Stability	Precision	Accuracy	Continuum
Passive Cable	✓	✓		✓
Optical Delay	✓	✓	✓	✓
Electronic Delay	✓	✓	✓	✓

Table 3.0 : Calibration Systems for Electronic Timing

There are a number of calibration methods which can be used to calibrate electronic timing systems, and some of these are shown in Table 3.0. It is important to address terms like stability, precision (see jitter above), accuracy and continuum in calibration. Stability is defined as the repeatability of controlled delays over a specified time interval. The stability of passive cable delays for instance, is poor due to changing following connector mating cycles. When implemented correctly all three calibration techniques can be made to produce continuum delays, which means the adjustable calibrator reference delays are never subject to discontinuities.

3.1 THE OPTICAL CALIBRATOR TECHNIQUE

The optical calibration setup is traceable to the International Standard (the speed of light as defined by the metric standard), but must be implemented in the correct manner to attain these performance requirements. The following diagram demonstrates the basic concept of the optical calibration setup implemented in our developments:
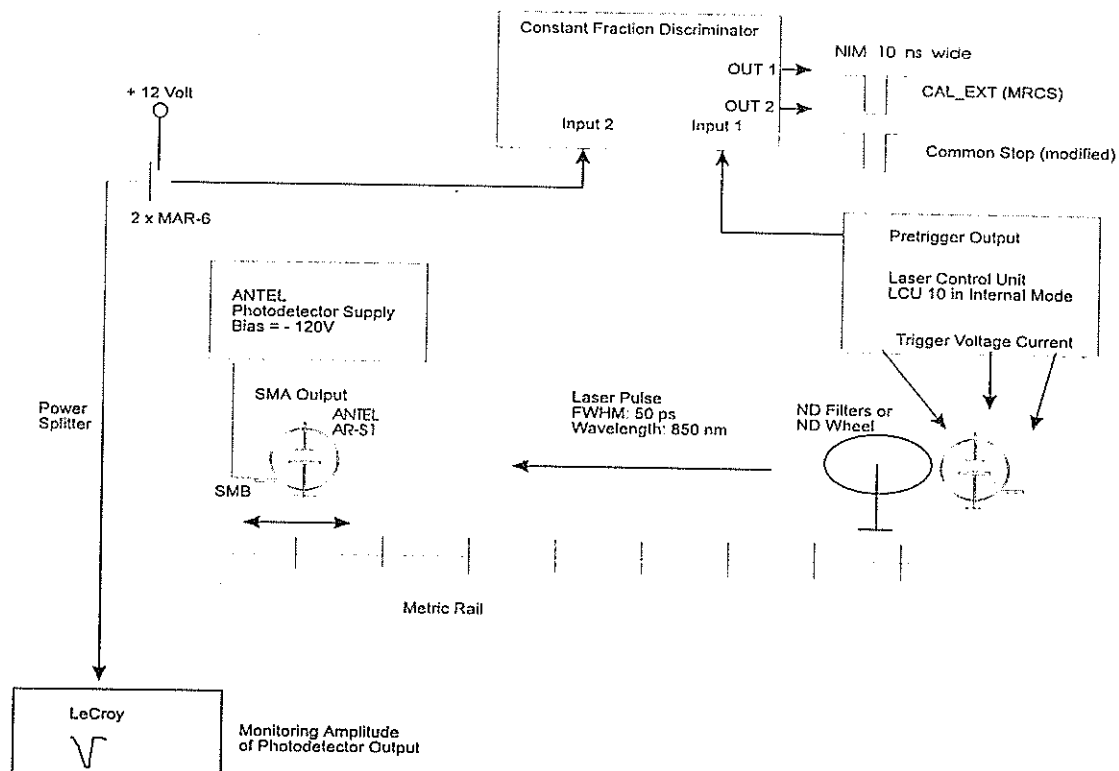
In this example, a picosecond laser is used to produce short laser pulses (FWHM 50 ps) at a repetition rate of about 1 kHz. The wavelength used is 850 nm. A standard silicon photodetector is placed on a movable micrometer screw along a metric rail. The maximum distance must be sufficient to cover the operating dynamic range of the timing system.

The problems we encountered in the early development of this setup included a change in the output amplitude of the detector diode along the rail. This introduced a time error which was reduced by the constant fraction discriminator but not eliminated. The adjustable natural density filter wheel was then introduced to keep the photons seen by the detector diode at the same amount. The result being that the output of the photodetector diode will stay at a constant voltage

along the rail. The output was monitored by the oscilloscope for verification. The jitter between start and stop pulse with the original configuration was typically less than 20 ps rms. Calibrating the timing system down to 1 ps is then a statistical process achieved by acquiring at least 400 samples.
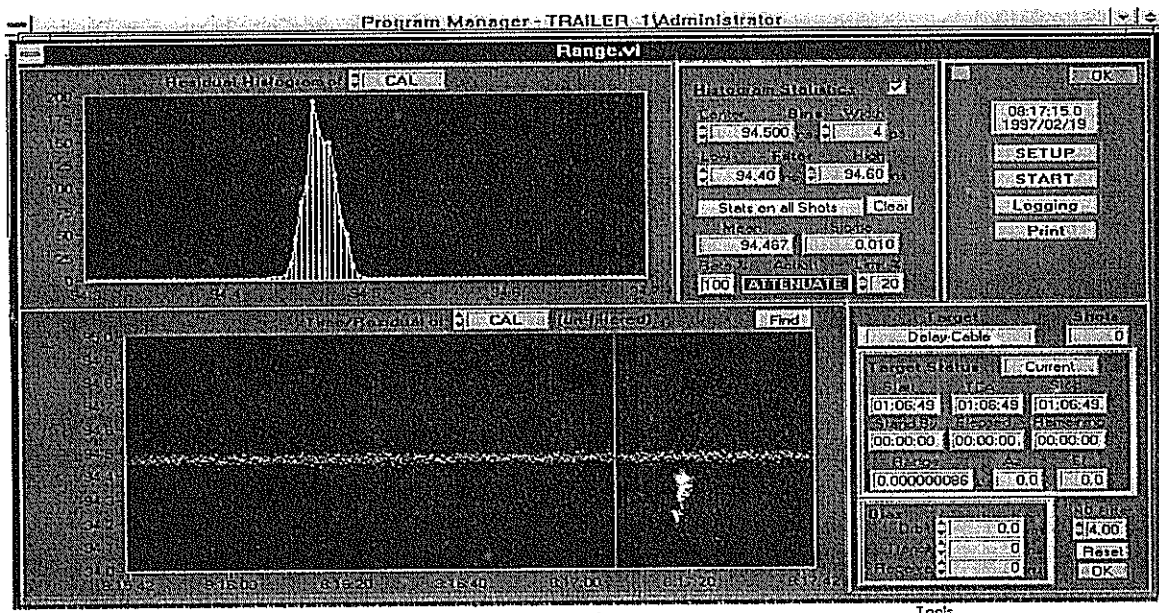
3.2 THE ELECTRONIC CALIBRATOR TECHNIQUE

Electronic calibrators are less expensive to produce, easier and faster to set up and operate, and allow calibration as the routine rather than the exception. Full automation of calibration procedures eliminates human error. Nevertheless, each electronic calibrator has to be calibrated against the International Standard.

First generation electronic calibrators employed were based on a programmable controlled crystal oscillator driven by a stable reference frequency. The implementation of such a system is based on programming the oscillator to produce precise time delays which are then offered into the timing system through electronic switches. These calibration pulses are provided via the same path to the timing system as that used by the real detectors for symmetric ranging systems.

Second generation calibrators are based on charge controlled switch devices. Delays from a few picoseconds to over 10 nanoseconds, adjustable in hundreds of femtosecond steps, have been shown to be possible with this system. The time jitter associated with these type of electronic calibrators is typically less than 5 ps rms. In the process of developing electronic calibrators and an optical calibration setup it is extremely important to consider ultra-low noise design and RF design techniques.

4. SUMMARY

Using such design principles and methodologies we shall be able to improve the performance of the SLR timing system beyond the state of the art currently available in commercial timing instrumentation. Subpicosecond accuracies are attainable due to advances to the technology available and by following the design methodologies outlined. As can be seen in the following screen capture from the Keystone system the 10 ps (one-sigma un-filtered) timing system precision has already been achieved.

5. APPENDIX : DEFINITION OF TERMS

ACCURACY
A quantative term for the measurement to the true value of a parameter within declared probability limits. Range measurement accuracy is the measurement error. That is the difference between the true range and the measured range to within a specified measurement tolerance.

RESOLUTION
Range measurement resolution is the minimum differential measurement which can be made irrespective of accuracy or precision. Resolution is the difference between two adjacent measurement points or the smallest element in a measurement reading.

PRECISION
Range measurement precision is the standard deviation of the measurement about the true measurement or the root mean square variation of measurement.

SENSITIVITY
Sensitivity is the measure of the dependency of one parameter on another or the ratio of particular output parameter to corresponding input change

STABILITY
Repeatablity of a process over a certain time otherwise the variation of measured output under specified constraints.

JITTER
Jitter is a random displacement of a signal from its true location in time. These displacements can occur in amplitude, phase, and pulse width, and are generally categorised as either deterministic or random. This term applies to the time of an event often start and stop times which the uncertainty of rise and fall times may then affect.

BIAS
Offset to a quiescent point (ie zero voltage) or in SLR bias can be used to describe systematic deviation from an accurate value. Particularly common in statistical estimates of parameters

DETERMINISTIC
Deterministic means non-random ie determined or initiated by a known or controlled event. This refers to an action or event. ie it is determined or initiated by a known or controlled event

SYMMETRIC RANGING
Measurement of related events (T1 T2) via the same optical and semiconductor (vernier) path to cancel systematic errors.

WLRS Timing System Aspects

Ulrich Schreiber
Forschungseinrichtung Satellitengeodäsie
Fundamentalstation Wettzell
D - 93444 Kötzting
Germany

Karl Heinz Haufe, Nikolaus Brandl, Reiner Dassing,
Günther Herold, Günther Pochert, Dieter Feil
Institut für Angewandte Geodäsie
Fundamentalstation Wettzell
D-93444 Kötzting
Germany

Abstract

One of the most crucial elements in a laser ranging station is the timing system. It determines the achievable resolution in the time of flight measurement of the laser pulse in general. However, quite often the timing system is responsible for small scale systematic errors in the range measurements. These errors can be the cause of persisting bias effects for a station. Therefore the properties of the timing system [1] of the WLRS (Wettzell Laser Ranging System) have been studied in detail. This paper discusses some of its characteristics.

1. DESIGN OF THE EVENT TIMER

The 5 MHz output of a hydrogen maser source is multiplied to 50 MHz and fed to the master ranging controller. This clock signal represents a stable coarse epoch of 20 ns granularity. The fine epoch, which interpolates between these intervals is generated on the occurance of a stop event. The estimation of this fine epoch is based on the charged capacitor principle, where the short timespan between the recorded event and the next clock signal is used to charge a capacitor. This capacitor is discharged at a constant rate over a far longer time interval (approx. 2000 times longer) afterwards, so that the time of the electrical discharge is easy to measure. This means that time is proportional to the voltage on the capacitor and the timer must have a very linear relationship between time and voltage. The WLRS uses 3 time to digital converters (LeCroy 2229) for this purpose and their respective non linearity was found to be below 10 ps over the entire operating range.

Since the WLRS uses a realtime calibration along with the range measurement, it is an absolute necessity to have the same electrical path for both signal sources, down to the level of individual circuit components. This demand results from the effect, that the travel

time of say the rising edge of an electrical signal through the timer circuit is of the order of roughly a hundred nanoseconds, while differences in the timing of events are significant at the level of less than 10 ps.

2. CALIBRATION AND STABILITY

For ranging operation, it is absolutely mandatory to perform a precise calibration of these fine epoch timing devices now and again. This is preferably done by using an optical rail, where increments in the time of flight are achieved by increasing the distance between the pulse laser and the detection device, as a retroreflector is pushed along a rail. Figure 1 sketches the principle of the optical setup. The high energy laserpulse passes through a wedged window on its way towards the telescope. The return from one of the antireflection coated window surfaces is guided along a rail, where it bounces back from a corner reflector. The returning light passes through the window again and passes a diffusing window, before it is detected by an avalanche diode, operated in linear mode. Even under non saturated conditions this diode responds with a very sharp risetime of less than 200 ps. The repeatability of a measurement was shown to be less than the resolution of the timing unit, once the diffusive window was inserted. Without this window there were numerous miscounts obviously due to spurious contributions from the laser signal.

Usually this calibration of the slope of the fine epoch generator is very stable, so there is no requirement for frequent updates. On the other hand one finds significant variations in the time of flight measurement for a geometrically constant reference path. This can be as much as 4 cm over a period of a few weeks, down to a few mm within an hour. The cause of this is temperature variations in the ranging electronics. Ideally all the timer electronics should be temperature stabilized to the level of a tenth of a degree over a few days. Since there are a number of heat dissipating units inherently part of the timer, the temperature level is not very well maintained. Figure 2 shows the behaviour of the temperature on the sensitive part of the timing board of the Master Control Ranging unit. One can see changes in the temperature of the electronics of up to 3 degrees within less than 20 hours. The duty cycles of the airconditioning system are also clearly visible in this time series. Since the timer is built such that it frequently performs a new slope calibration of the verniers by the use of internal electronic delay lines, a similiar temperature dependence was expected. Figure 3 shows how the observed variations in the temperature affect the calibration of the time to digital converters. Taking into account, that the shown calibration runs are only taken during two time intervals of the temperature sequence of figure 2 marked with A and B on the plots, a very strong correlation is evident. For example, calibration run A yielded an offset of $0.0001 \frac{ns}{count}$, which corresponds to change in the range measurement of 130 ps. A comparison between a number of these internal calibrations and some intermediately done absolute optical calibrations showed that these changes can be basically related to the temperature behaviour of the internal delay line electronics. Therefore the internal calibration feature was disabled.

Since the temperature dependence of the signal transit time through electronic components is a general problem, similiar behaviour was found for two crucial sections within the event timer. These sections are the time to digital converters for the fine epoch and the control circuit, which directs the detection signal to its respective receive channel. A sudden

increase in temperature of about 3 degrees was introduced to the respective circuits. A drastic effect of far more than 100 ps were found for both as one can see from figure 4 and figure 5.

The effect on the range measurements however is not as dramatic as discribed above, since it affects both calibration and range. On the other side it causes a floating value for the (constant) calibration measurement from pass to pass, which in turn makes a clear diagnosis of the system's operational state impossible. A general remedy for the addressed problems for the given event timer can not be made easily, since all the timing related components are made from individual logic circuits, which are mixed with non critical logic on the same circuit board. A sufficiently stable temperature control could not be realised, due to high heat dissipation of many of the electronic parts. In order to keep the probability of instrument introduced biases low on the WLRS, a normal point binwise correction for the ranges was implemented.

References

[1] Electro Optic Systems Pty Ltd.; "Design manual of the Wettzell Laser Ranging System", (1988)
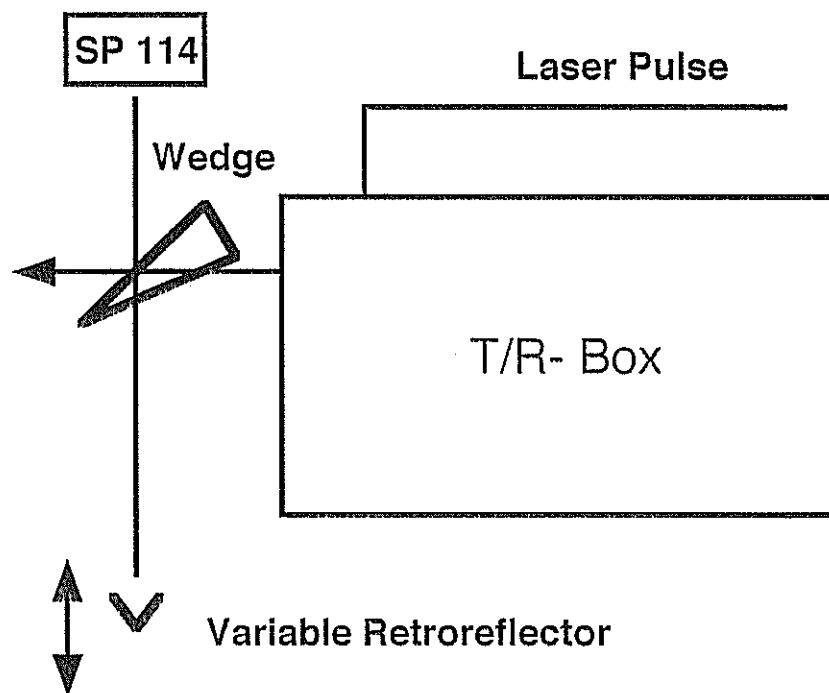
Figure 1: The principle of the optical setup of the calibration of the time to digital converters
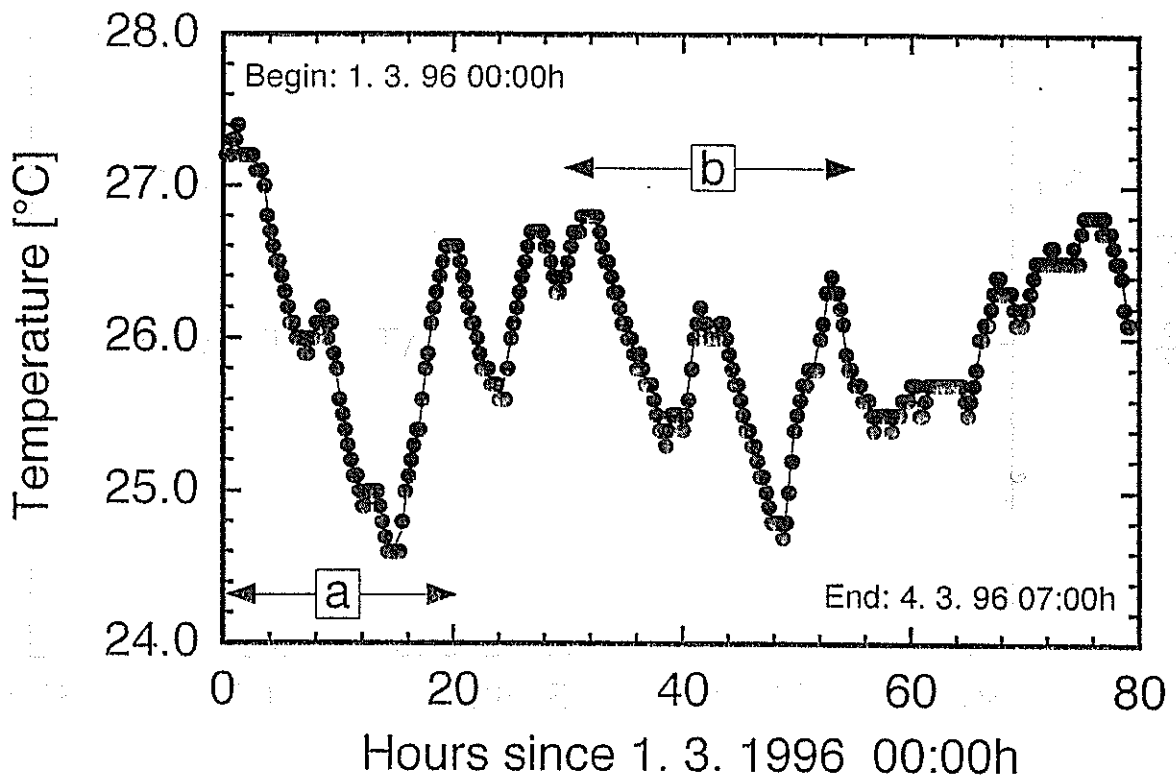
Figure 2: Temperature variation on the Master Ranging Controller board under normal ranging conditions over a weekend
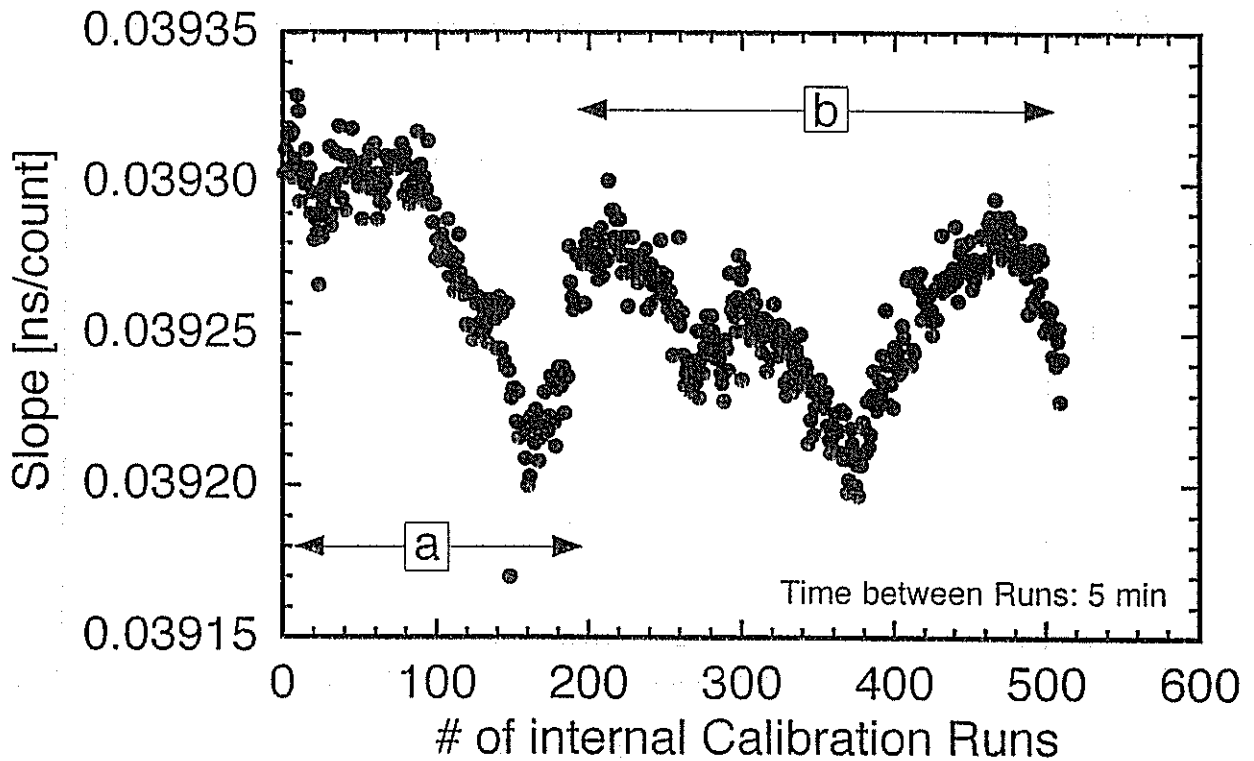

Figure 3: The effect of temperature variations on the slope calibration of the MRCS event timer. On average there are 1300 counts to a fine epoch. Therefore one has a change of roughly 130 ps due to 3 degrees of change in the ambient temperature
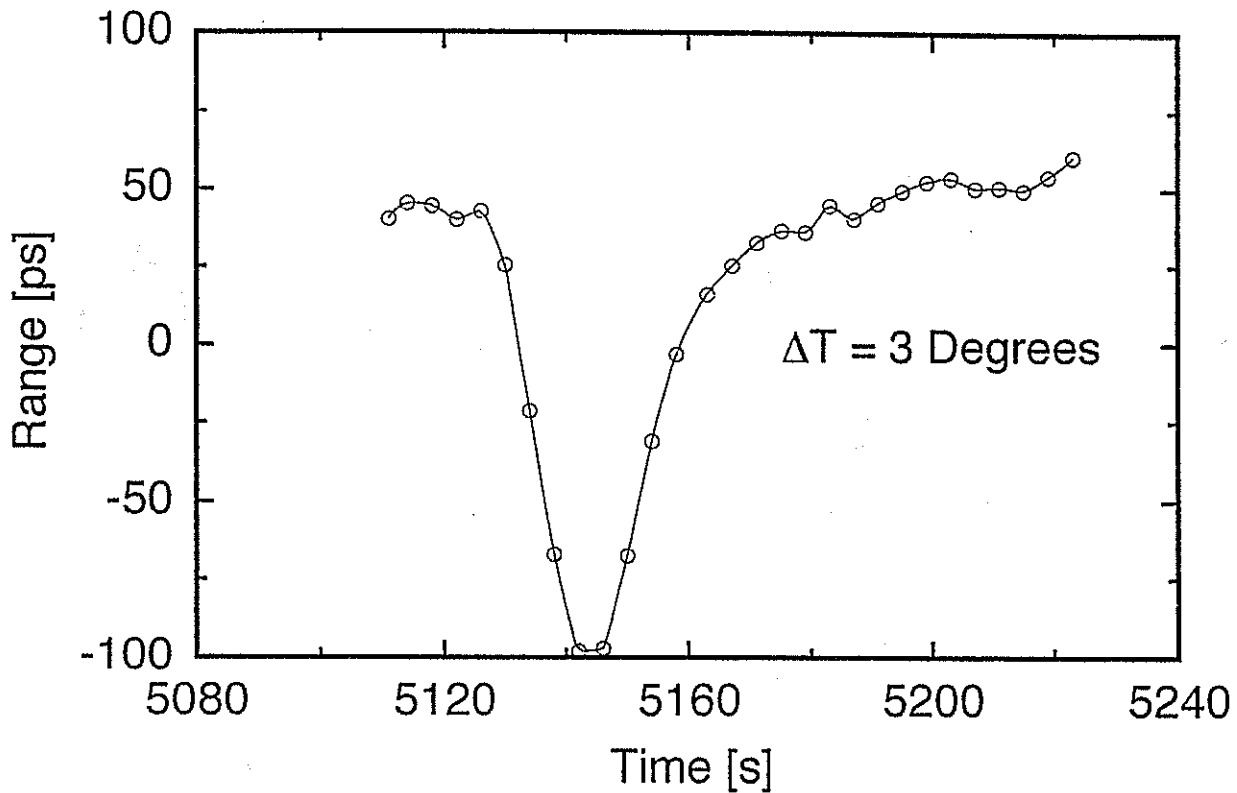
Figure 4: Variation in the range measurement for a constant range under the application of a temperature change of 3 degrees to a LeCroy 2229 unit over a short period of time
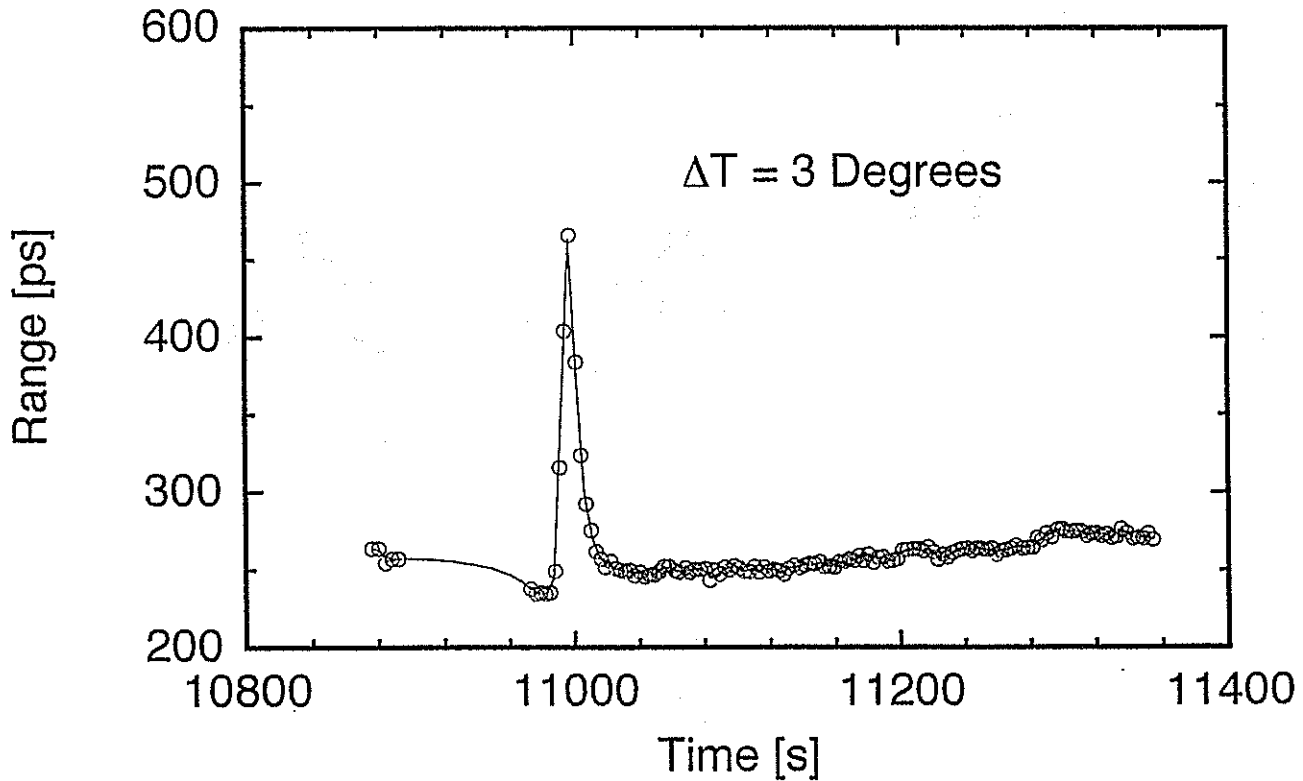

Figure 5: Variation in the range measurement for a constant range under the application of a temperature change of 3 degrees to the signal control unit of the MRCS over a short period of time

Short Distance Calibration

G. Kirchner, F. Koidl
Institute for Space Research / Austrian Academy of Sciences
Observatory Lustbühel; A-8042 GRAZ / AUSTRIA

1.0 Introduction

The target used for external calibration at SLR Graz during the last 16 years was a simple flat plate, located in a distance of almost 400 m; the transmitted laser beam was attenuated by insertion of 2 mirrors into the transmit path; although easy and convenient for routine operation, we realized many disadvantages, potential hazards for range biases, and inherent accuracy problems. To avoid all possible drawbacks, a new, very-short-distance, external target was designed, build and installed within the laser dome. The total error sum due to the new target is now below 1 mm, and its contribution to measurement jitter now is close to Zero.

2.0 Disadvantages of the old system

Approaching ranging results of below 5 mm single shot RMS for ERS satellites, and below 1 mm Normal Point RMS for LAGEOS, such a simple target became totally inadequate:

- The distance, dictated by the transmit/receive parallax, is difficult to measure to Sub-mm;
- Due to the necessary effort, re-measurements were rare, and not accurate enough;
- The influence of meteorological uncertainties could be up to 2 mm;
- Tilting of the attenuation mirrors could cause errors of up to 2 mm;
- Misalignment of the flat plate caused biases (up to 3 mm), and increased the jitter;
- The target was not accessible in bad weather conditions;
- Due to the long atmospheric path, the target was not acceptable for MultiColor Calibration.

3.0 Design of the new target

A new target was designed (Fig. 1, 2) which now fulfills the following specifications:
- The distance is very short (about half a meter in front of the telescope); this allows very accurate distance measurements, which are also easy to repeat and to check;
- The short distance eliminates any meteorological uncertainties; it allows also calibration and tests even when there is rain or fog outside (everything is within the dome);
- The optical path is identical for calibration and ranging; there are no filters etc. inserted;
- There are no restrictions for MultiColor Calibration;
- We tried to avoid any possibility to add bias or jitter by the target;
- Changes of target position / distance are indicated by a low-cost CCD to sub-mm accuracy.

Due to the short distance, and due to the location of the target within the dome, the laser has to be attenuated BEFORE leaving the laser room, to avoid heavy backscatter in the dome, which would create serious problems for any Single-Photon Detector; this is done by changing the delay time of the laser amplifier flashlamps relative to the oscillator flashlamps (done automatically by

the real-time PC); due to the location of the start pulse detector before the amplifiers, this does not affect the timing at all.

GRAZ SHORT DISTANCE CAL TARGET

1742.3 mm

DIFFUSOR PLATE

0.1 %

Receive-

Transmit-

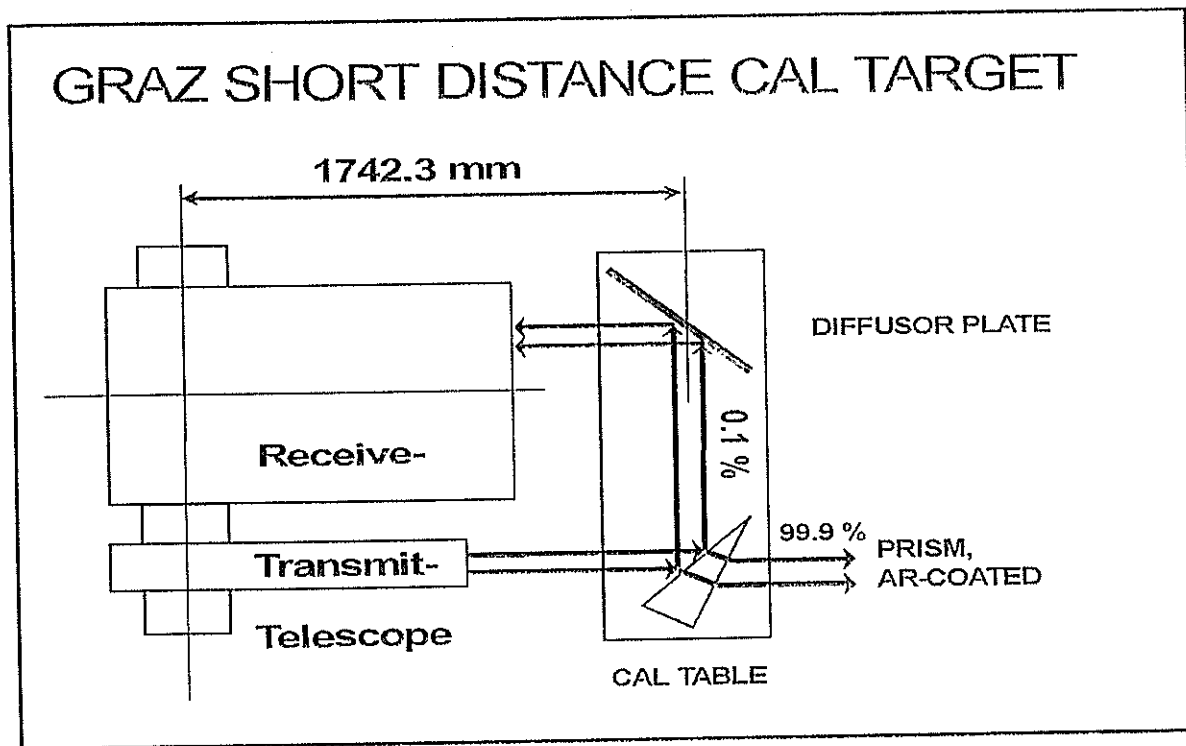99.9 % PRISM, AR-COATED

Telescope

CAL TABLE

Fig. 1: The new short distance calibration target .....

Also due to the short distance, the standard gate pulse - derived from the standard start pulse for ranging operation - would arrive too late at t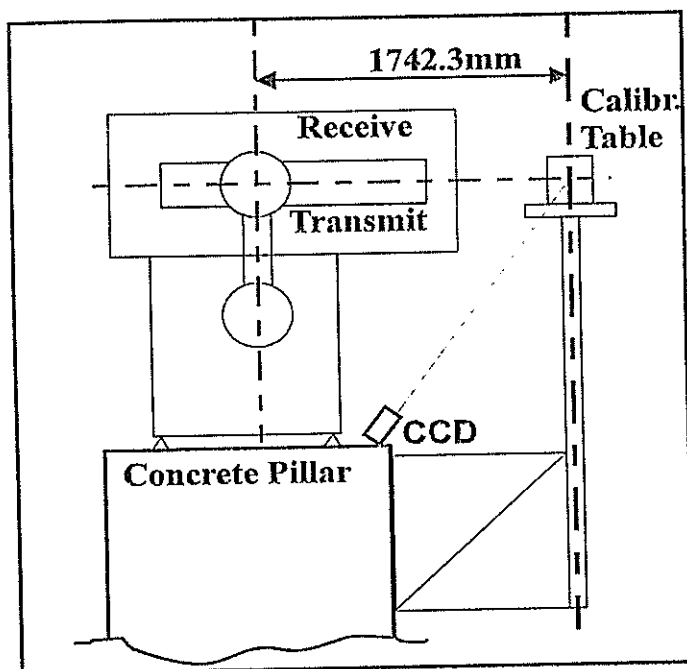he SPAD unit to gate it. Thus we use a separate gate pulse detector for generation of the calibration gate pulse, which detects the pre-pulses of the mode-locked train about 300 ns before the actual laser pulse. Because this gate pulse is slightly fluctuating relative to the actual laser pulse - due to the uncertainty of detecting one out of many rather small pre-pulses - the position of the calibration return pulse within the calibration range gate is also fluctuating slightly; this eliminates automatically any possible bias problems related to a fixed position of return pulse within the cal range gate, or would indicate it at least by increasing the jitter.

1742.3mm

Calibr. Table

Receive

Transmit

CCD

Concrete Pillar

Fig. 2: ..... is mounted on the telescope pillar

The target itself consists of a prism and a diffusor (Fig. 1) to redirect the beam into the receiver; both items are aligned for perpendicularity - using auxiliary penta prisms etc. - and to keep all parts of the calibration beam in the same horizontal plane, avoiding any geometrically induced biases and jitter.

The prism is AR-coated for 532 nm to reduce the reflected energy to 0.1%; the AR-coating is chosen for higher reflection for the 683 and 435 nm, to compensate here for lower energies. The use of the prism avoids any secondary reflections. The diffusor is just a flat piece of black anodized aluminium, to attenuate the laser once more.

The beam is additionally attenuated by using the standard small Field-of-View for day-light ranging; small changes of this FOV allow fine adjustment of the received energy, giving return rates between 1% and 100%. Significant higher - or also lower - received energies (for tests only) can be easily selected by manually changing the laser amplifier delays.

The whole target is mounted on the same concrete pillar as the telescope mount (Fig. 2); in this way the relative distance between mount and target is fixed. To protect the target, its mounting rod is enclosed by an additional protective rod.

The position, distance and alignment of the whole target is checked with a CCD camera down to the sub-mm range: A small hole in the diffussor directs a portion of the calibration beam to a small auxiliary mirror, which reflects this beam - with an angle of 45° - down to a CCD at the bottom of the telescope mount. Thus even sub-mm movements of the target, its distance or its position relative to the telescope are visible as big offsets on the TV screen.
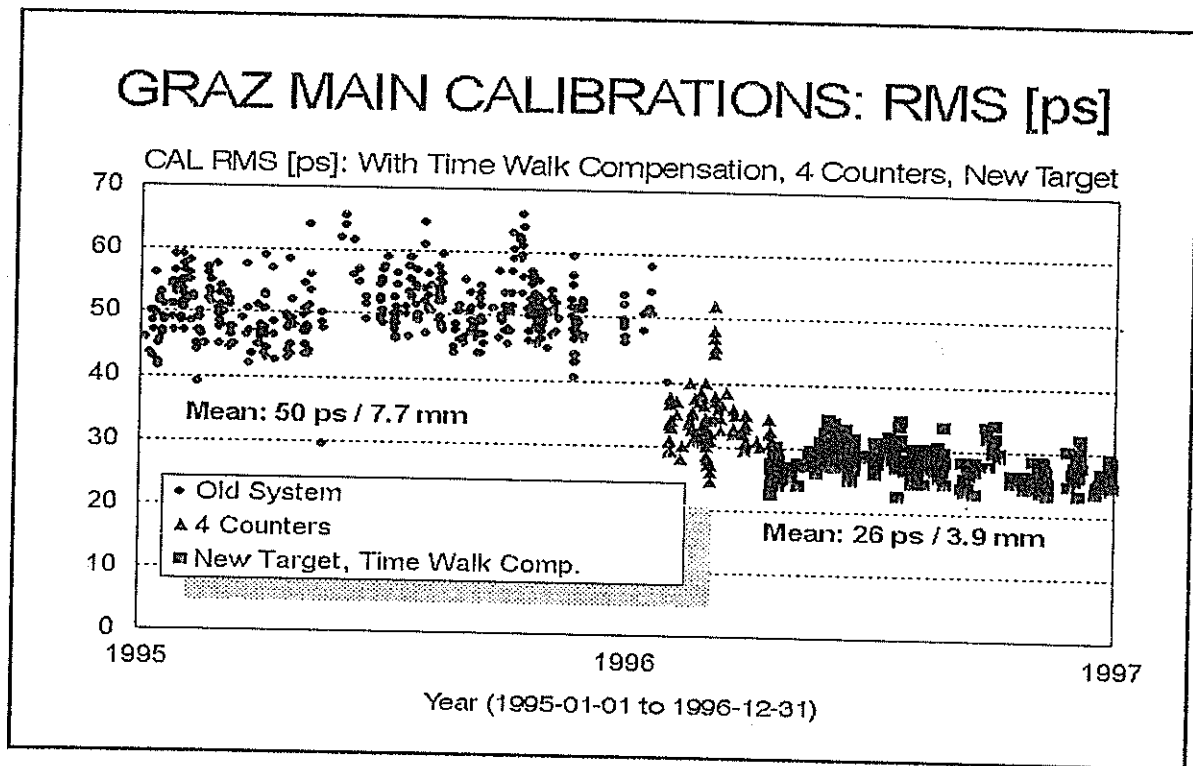

Fig. 3: Single Shot RMS Improvements

4.0 Results

The new calibration path was measured multiple times. using different persons, methods, scales etc.; resulting in a corresponding target distance of 1742.3 ± 0.3 mm. The single shot RMS of the routine calibrations to the new target now is below 4 mm (Fig. 3), which is also due to the use of up to 4 counters parallel, Time Walk Compensation for the SPAD etc.

At the same time - April 1996 - the calibration procedure was changed; before this time we used pre- and post-calibrations for each single pass; now we make more extensive calibrations (at least 500 returns) whenever a time slot between satellite passes allows, but at least once each hour; all results (calibration values, meteorology values, counter offsets etc.) are stored in a main calibration file; during post-processing, all relevant values are interpolated linearly for the epoch of each return (Fig. 4).
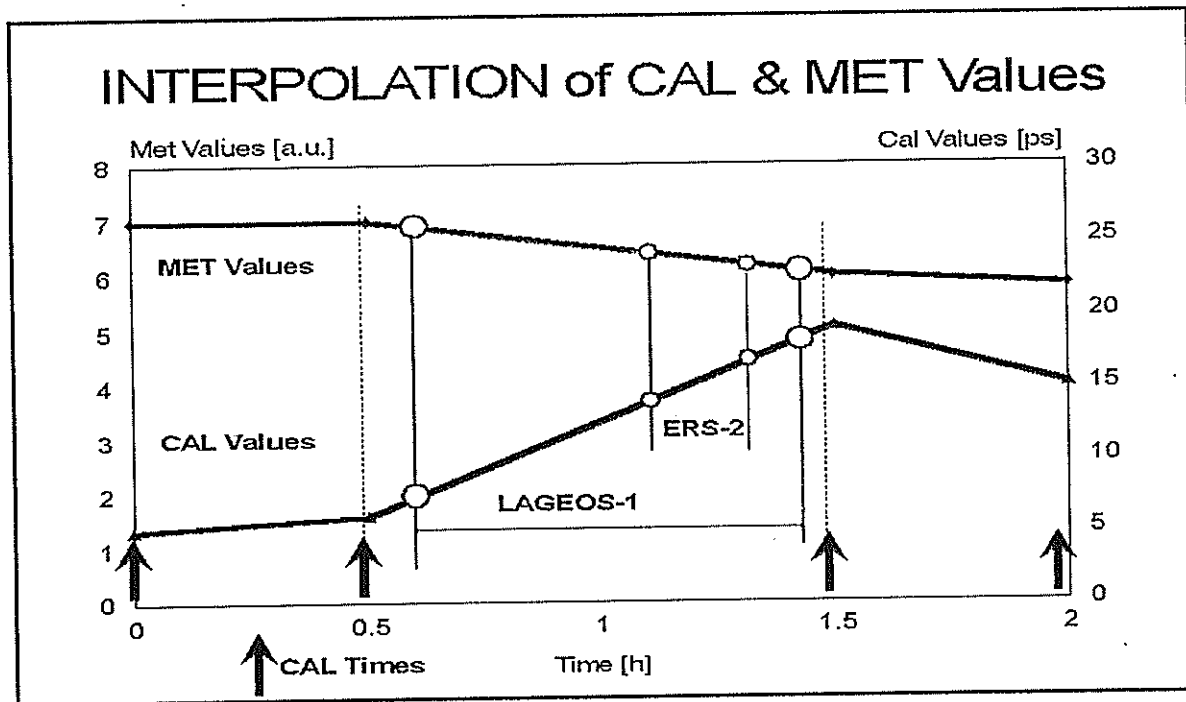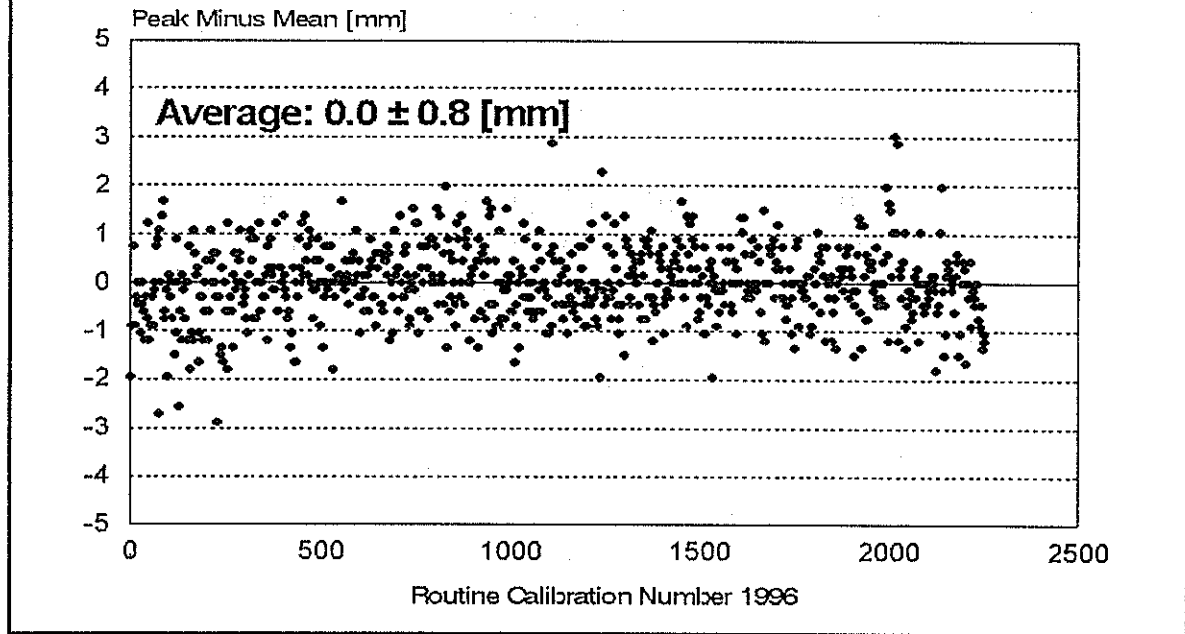

Fig. 4: Calibration Procedure / Sequence

Fig. 5: Peak-Minus-Mean of Calibration Runs

The sum of all improvements (very short distance cal target, SPAD Time Walk Compensation, SPAD gating with 10 V above Break, MultiCounter Operation) now gives a very symmetric distribution of the returns from the target (in spite of the inherent tail of SPAD return distribution); this can be seen in the Peak-Minus-Mean Statistics (Fig. 5) of the routine 1996 calibration runs:: There is no skew, and average Peak-Minus- Mean is Zero.

435

PORTABLE SLR CALIBRATION STANDARD

I. Prochazka, K.Hamal

Czech Technical University, Brehova 7
115 19 Prague 1, Czech Republic
fax +42 2 85762252, prochazk@mbox.cesnet.cz

H. Kunimori

Communication Research Laboratory, Tokyo, Japan

B. Greene

Electro Optics Systems, PtyLtd, Queanbeyan,NSW, Australia

Range bias is the key issue facing SLR in the next years. Since system standardization will not overcome this problem fully in the foreseeable future, there is a need for a means of calibrating the individual SLR system for range and time biases. The most rigorous calibration would involve a complete SLR portable standard, which would collocate with the system under test. A more economical approach allows the laser and telescope of the system under test to be used.

We are presenting a concept and design of a portable calibration standard for Keystone Project satellite laser ranging systems. It consists of the reference time interval counter, epoch counter, independent standards of frequency and epoch, meteorological sensors, control electronics and software package. All the crucial parts are enclosed in an air-tight box maintaining the temperature within 50 milli Kelvins. The only inputs to the Standard are the Start and Stop signals of the SLR under test. Due to the Keystone Project SLR systems design ['zero offset calibration scheme' among others] the Portable Calibration Standard will be able to identify most of the biases in the SLR system under test. The range and time bias resolution is 1 millimeter / 100 nanoseconds respectively on a single satellite pass basis. The Standard is enclosed in a hand transportable box, it may be easily and quickly relocated within the SLR network.

PORTABLE CALIBRATION STANDARD
PHILOSOPHY

- Range bias is the key issue facing SLR.

- There is a need for a means of calibrating the individual SLR systems for range and time biases.

- The most rigorous test procedure is a collocation with an independent SLR system.

- A more economical aproach allows the laser, telescope and detectors of the system under test to be used.

Prochazka.Hamal,Greene,Kunimori, Shanghai '96

PORTABLE CALIBRATION STANDARD
CONCEPT

- Independent - ranging hardware (start/stop NIM inp.)
    - epoch & frequency reference
    - noise reduction, data processing SW
    - meteo sensor (pressure)
    - temperature control
    - RF protection
    - AC power filtering
    - grounding

- Compact design, hand transportable

- One calibration standard rotated regularly through KSP SLR systems will form an independent ranging refference.

Prague. February '96

PORTABLE CALIBRATION STANDARD
PARAMETERS

Time of flight	Stanford Research SR620
Epoch & frequency ref.	GPS Hewlett Packard
Climabox	airtight, +/- 0.05 K
Control	notebook size PC
Air pressure sensor	0.01 mB
Dimensions	50 x 40 x 30 cm
Mass, power	25 kg , 200 W
Setup time / warm up	1 hour / 1 day

Prague, February '96

PORTABLE CALIBRATION STANDARD
PARAMETERS 2

Time of flight resolution	25 psec RMS /SR620/
Frequency accuracy	10E-12 /GPS/
Laser fire epoch resolution	100 nsec
Epoch reference	110 nsec /HP-GPS/
Measuring repetition rate	10 - 5 Hz low satellites/GPS
Control	notebook size PC
Prediction	Integration IRVs time bias on-site update
Data analysis	noise filtering, data reduction normal points, full rate..
Data comparison	Range and time biases frequency, epoch, meteo

Prague, February '96

PORTABLE CALIBRATION STANDARD
ACCURACY

RANGE
resolution / single shot   ‹ 10 mm RMS
stability   0.5 mm / hour
frequency   10E-12 /GPS/

RANGE BIAS
resolution / pass   ‹ 1 mm
stability   0.5 mm / hour

EPOCH
resolution / single shot   100 nsec
refference   110 nsec /GPS/

TIME BIAS
resolution / pass   ‹ 50 nsec

Prague, February '96

Portable Calibration Standard (PCS)
CONCLUSION

- Portable Calibration Standard is a powerful tool
  to identify most of range and time bias sources
  introduced by   – ranging machine
                 – calibration
                 – on-site data processing
                 – operator error

- Due to high mobility, short setup time and shot
  by shot comparison scheme, the result is available
  within days at any SPAD based SLR site.

- Considering the existing and foreseen SLR network
  status and the SLR data quality requirements,
  the Portable Calibration Standard seems to be
  worth considering as an option to a true collocation.

Prochazka,Hamal,Greene,Kunimori '96

SLR bias sources
Ranging machine contribution

source		identification
Frequency & epoch		PCS
Calibration	survey	minicollocation
	mount ecc.	minicol.partially
	correlated RF	PCS partially
		minicol.partially
	stability	PCS
Signal strength/time walk		low rate / SPAD
Instrumental errors		PCS
Data processing		PCS
Meteo data		PCS
Operator errors		PCS

Prochazka,Hamal,Greene,Kunimori '96

PORTABLE CALIBRATION STANDARD
DESIGN OBJECTIVES

- Determination of range and time biases
  of the satellite laser ranging system.

- Identification of contributors to these biases.

- Alternative to the collocation using the mobile
  SLR system :
  - simple deployment to the site
  - short setup time
  - fast 'feedback' on site
  - shot by shot comparison available
  - based on proved technology HW/SW

Prague, February '96

PORTABLE CALIBRATION STANDARD

METEO

GPS time & frequency

CLIMA box +/- 0.05 K

RF shield

SLR system under test

START STOP

1 pps 10MHz

PCE

SR620

notebook

GND

AC pwr

MERIT2 / NPT output data

Data comparison

MERIT2 / NPT output data

RESULT
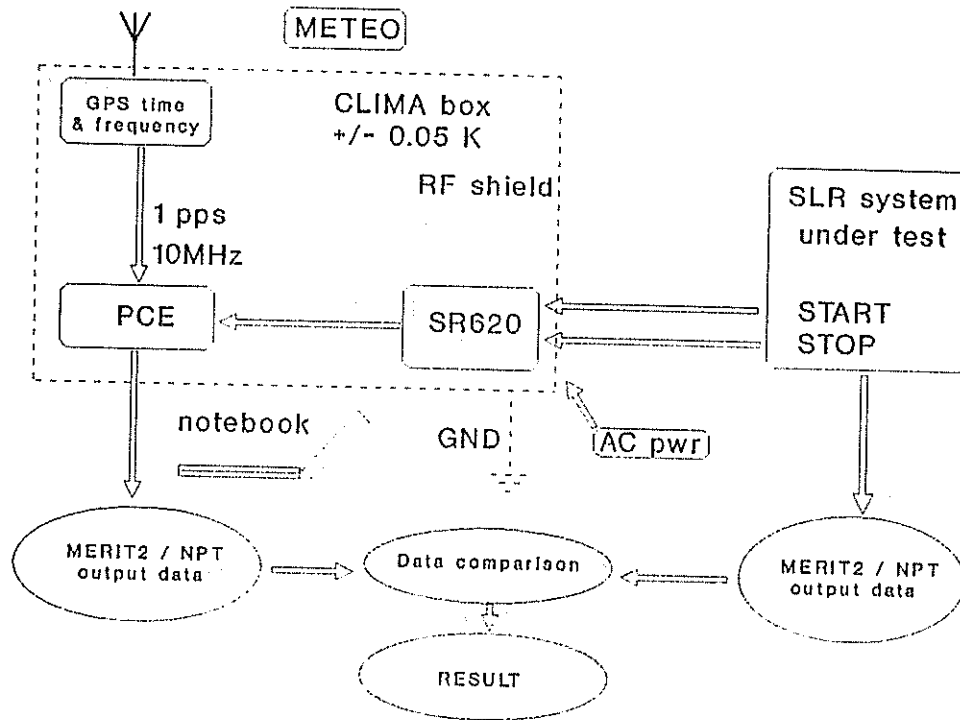
Prague, February '96

CLIMABOX TEMPERATURE CONTROL
Device mainframe temperature
Dissipated 100 W, ambient +20.. +24C

device temperature [Centig]

SR620 drift 5psec/Centig.

time [min]
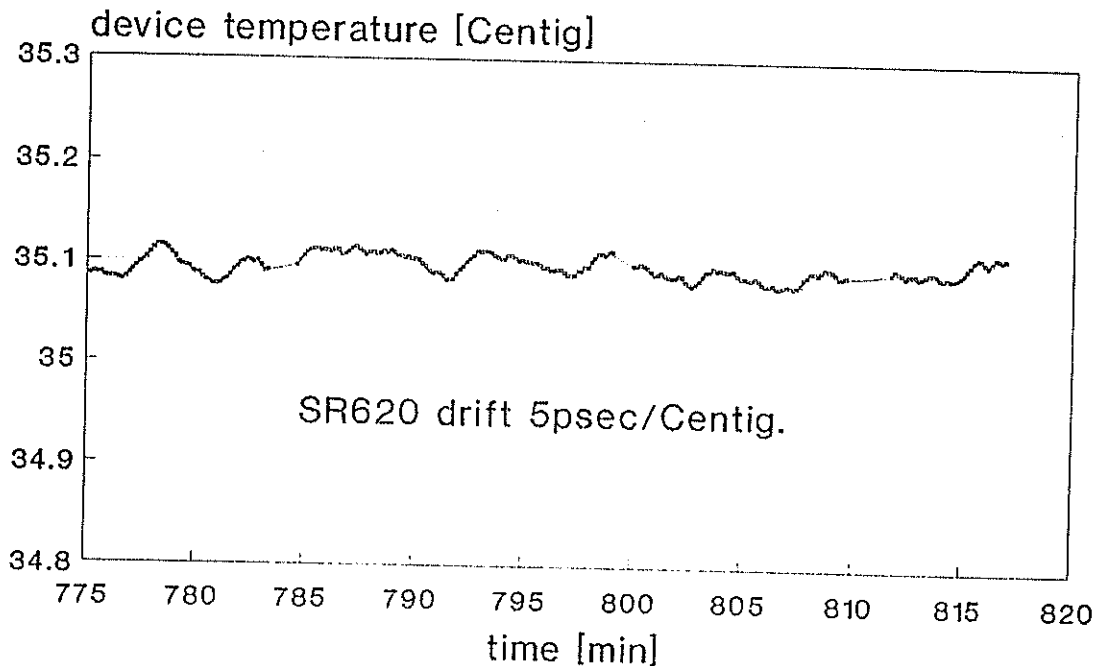
J..Blazej, I.Prochazka, Shanghai '96

CALIBRATION SETUP FOR HELWAN STATION
TWO DETECTORS COMPARISON EXPERIMENT

M.Tawadros

National Research Institute of Astronomy and Geophysics
Helwan, Egypt
fax +20 2 782683

I.Prochazka, M.Cech, K.Hamal, H.Jelinkova, A. Novotny

Czech Technical University, Brehova 7
115 19 Prague 1, Czech Republic
fax +42 2 85762252, prochazk@mbox.cesnet.cz

The Helwan Satellite Laser Station is been upgraded under the joint effort of the National Research Institute of Astronomy and Geophysics, Egypt and the Czech Technical University. Among others, the additional guiding / receiving telescope 280 mm in diameter equipped with the solid state detector SPAD have been added to the existing system. Due to the optical setup of the new receiver and detector, the new calibration target and procedure had to be developed. To guarantee the satellite ranging data continuity and to preserve the low range bias of the station, both receivers and detectors were operated simultaneously. Due to the single photon ranging, both the detector output signals could be combined into the single ranging electronics, the echoes corresponding to different detectors were identified by their delays. Completing a satellite laser ranging pass, the appropriate calibration constants are applied to corresponding echoes. The range bias of the new receiver/detector/calibration setup versus the original one is evaluated by a simple substraction of measured ranges. The first results based on limited number of low satellites passes indicate the range bias +18+/-10 mm. It is expected, that the comparison scheme will be operated for the entire 1997 laser ranging mission to tune the new calibration procedure.
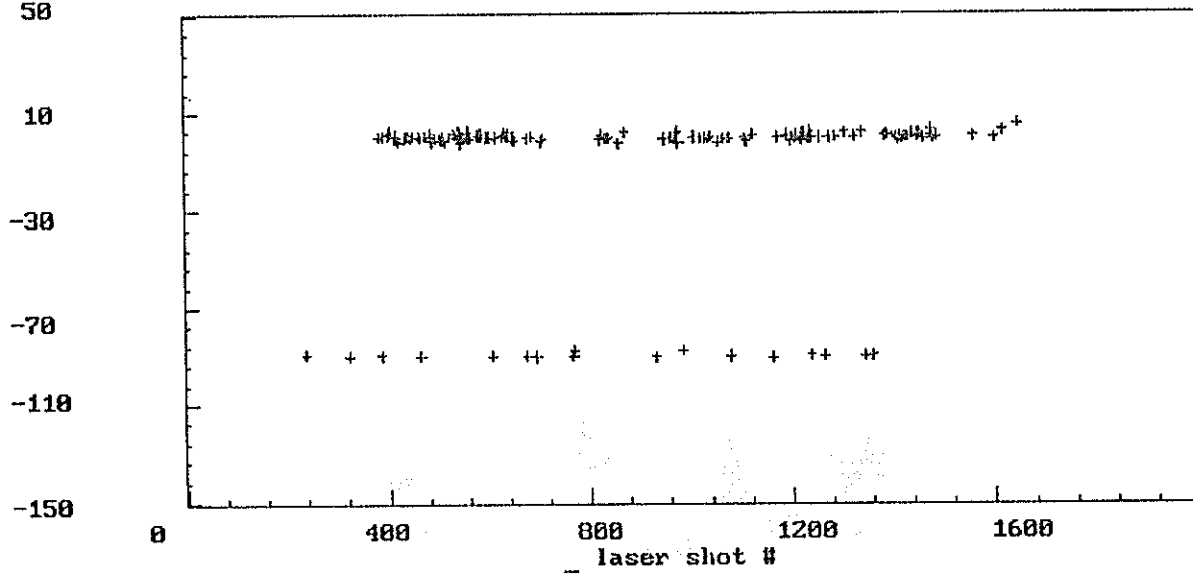
HELWAN 2 SATELLITE LASER STATION

Mount, DC motors, encoders, guiding telescope

O-C (ns)

Helwan 96 0 17 7501001.

50

10

-30

-70

-110

-150

0   400   800   1200   1600

_ laser shot #

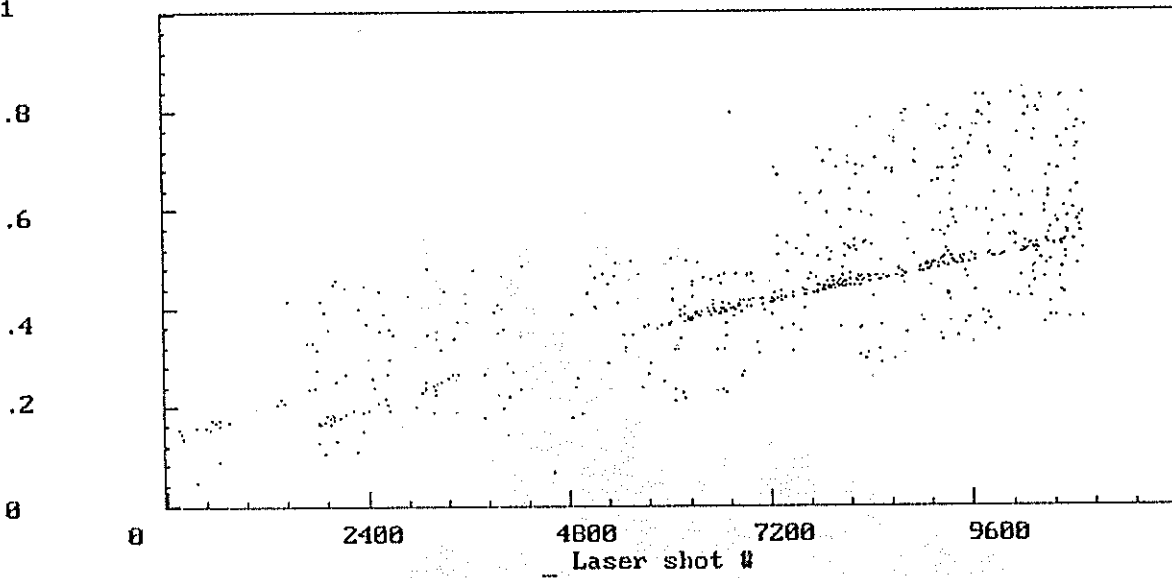**Starlette ranging, the first pulse within the semitrain selected, only.
Data used for range bias evaluation.**

O-C (us)

Helwan 95 9 10 9207002.

1

.8

.6

.4

.2

0

0   2400   4800   7200   9600

_ Laser shot #

**Lageos 2 ranging, due to optical axes alignment problem, the SPAD
data rate is elevation dependent. Note the dark count contribution of
SPAD and the ratio of return rate of both detectors. The average
data rate for well aligned SPAD was about 7x the PMT.**

Multiwavelength Ranging

/

Streak Cameras

STREAK CAMERA
and
Two Color Laser Ranging

JEAN GAIGNEBET, JEAN-LOUIS HATAT, JEAN-LOUIS ONETO
OCA/CERGA, AVENUE COPERNIC - 06130 GRASSE - FRANCE

Goals of Two Color Laser Ranging (TCLR)

TCLR is able to measure *in situ* the index correction caused by the double crossing of the atmosphere with an accuracy of 5 mm shot by shot. This correction could be considered a white noise only for very long integration time. This time has yet to be determined.

The discrepancy between the two color measurement and the existing models for a given epoch, fixed meteorological conditions and in a limited solid angle, could be considered as constant. This upper limit of this angle has to be defined by stations with a shot by shot ability to perform TCLR. My feeling is that a value has to be measured at least each 5° along the satellite track (geocentric angle).

Two Color Laser Ranging

TCLR is by essence a multiphoton process. It could be implemented along two different concepts.

◊ **Single photon counting (SPC)**. The differential flight time is computed by difference of the flight times obtained in each color, averaging a great number of relatively inaccurate measures. One have to keep in mind that :
- As the precision is increasing, a multiphoton event has a greater bias effect on the average value. To maintain a true SPC operation the ratio of returns over shots as to be kept very low. It could be in the 1 % range.
- The differential value has to be accurate within a few picoseconds. Reaching this level with individual measures at a shot by shot noise of 20 to 50 ps implies hundreds or thousands of detected returns.

Combining this two remarks, we see that the two color correction can be obtained only each 10^4 to 10^5 shots. Obviously the method is adequate only for very long passes on very high satellites with already very weak link budgets. As LLR is limited to true SPC operation this field is constrained to this approach.

◊ **Mutiphoton record (MPR)**. The differential flight time of each shot is deduced from the record of the arrival time of each photon in multiphoton collected light pulses. Today the equipment to implement the concept is limited to Streak Cameras (SC). We will see that with the pulsewidth optimized, without pulse processing, the number of photons is in the order of a few hundreds per wavelength for a single corner cube target.

Streak Camera limitation.

A Streak Camera is a time to space transformer. Statistically a photon extracts an electron from a photocathode. After acceleration of this electron and its deflection by two electrodes, it reaches a phosphor screen where it could be seen (Fig. 1). The position of the light spot is related to the arrival time of the photon on the photocathode. As in any detection device, the electron emitted from the photocathode is quite slow (a few eV), with spread energy and direction. An electrostatic field (kV.mm^{-1}) accelerates it and imposes a velocity parallel to it. This electrostatic field is limited by the breakdown field of the vacuum. As the energy of the photon reaches one keV, the speed is such that the jitter of the travel time of the electron during its flight is negligible versus the initial time spread. This intrinsic limit caused by the process of the detection itself is in the order of 2 ps RMS (narrower than for a SPAD 5 ps).

PHOTOCATHODE

FOCUS GRID

ANODE

SCREEN

FIBER OPTIC WINDOW
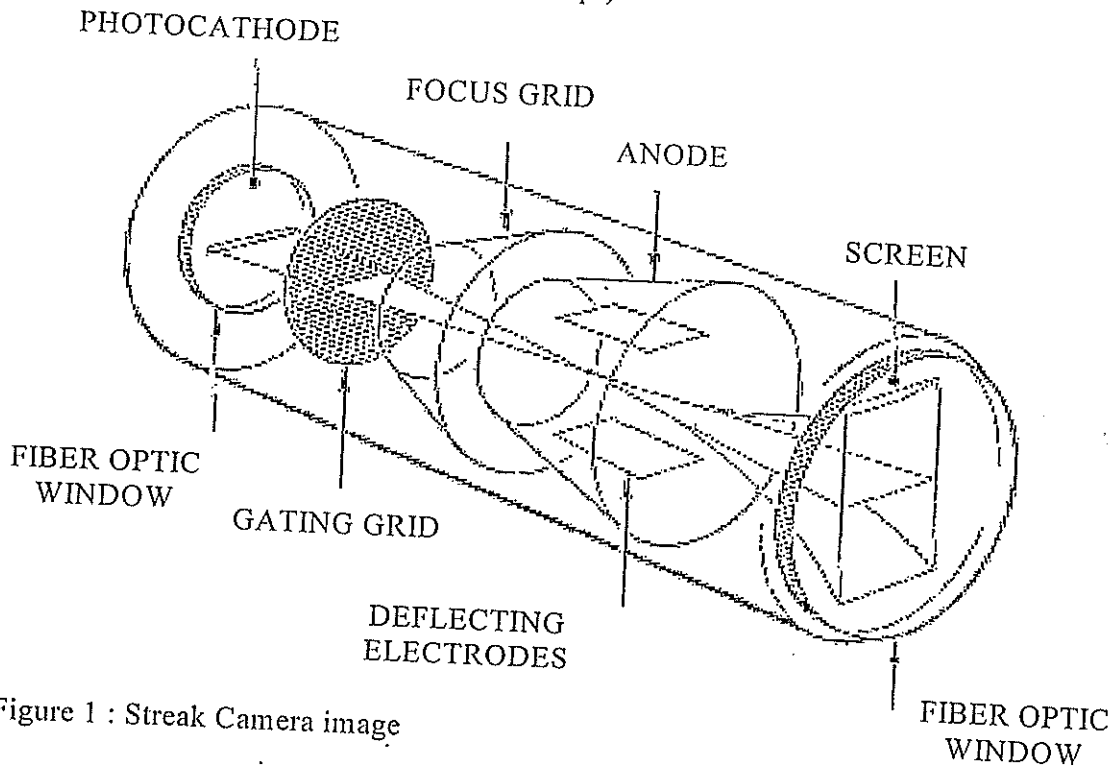
GATING GRID

DEFLECTING ELECTRODES

FIBER OPTIC WINDOW

Figure 1 : Streak Camera image

The following formula explicits the effect of the Streak Camera timing errors, and laser pulsewidth on the range measurement.

$$\sigma^2{}_D = \frac{(0.15)^2}{N} A^2 \left(\frac{\sigma_0^2 + \sigma_{\lambda_1}^2}{n_{\lambda_1} Q_{e\lambda_1}} + \frac{\sigma_0^2 + \sigma_{\lambda_2}^2}{n_{\lambda_2} Q_{e\lambda_2}} + \sigma_S^2 \right)$$

where

σ_D (mm)	= error on the distance correction
σ_{λ_i}	= 0.4242 the FWHM λ_i pulselength
σ_0	= intrinsic resolution (2 ps)
n_{λ_i}	= incident number of photon @ λ_i
$Q_{e\lambda_i}$	= photocathode quantum efficiency @ λ_i
N	= number of measures
σ_S	= camera readout errors
A	= sensitivity factor of the two color measurement (9 to 40)

447

Some remarks could be made :

- σ_S is smaller than σ_0 so σ_S^2 could be neglected.

- $\dfrac{\sigma_0^2 + \sigma_{\lambda_1}^2}{n\lambda_1 + Q_{c\lambda_1}}$ is the same order of magnitude as $\dfrac{\sigma_0^2 + \sigma_{\lambda_2}^2}{n\lambda_2 + Q_{c\lambda_2}}$.

The formula could then be approached by the simplified one :

$$\sigma_D^2 \approx \frac{(0.15)^2}{N} A^2 \left(2 \frac{\sigma_0^2 + \sigma_\lambda^2}{n\lambda Q_{c\lambda}} \right)$$

In order to reduce σ_D one has to minimize $\dfrac{\sigma_0^2 + \sigma_\lambda^2}{n\lambda Q_{c\lambda}}$. As σ_0 is a fixed value, two possibilities remain :

◊ Decrease of σ_λ :

If one decreases the emitted pulselength, the received one decreases to a minimum then increases again. This effect is caused by the dispersion induced by the bandwidth of the narrow pulse. For straightforward emission-reception schemes, the minimum received pulselength is around 14 ps (10 ps emitted, 10 ps broadening by dispersion). The number of photons needed to reach a defined accuracy is $\dfrac{2^2 + 14^2}{2^2 + 2^2} = 25$ times greater than the number needed for a 2 ps pulse. By pulse processing (chirp and pulse compression) it is possible to go down to received pulses in the ps region. If one designs a SC with a subpicosecond intrinsic resolution, the number of photons in each color, needed for a given accuracy, could be reduced by a factor of 200 versus the best systems available today.

◊ Increase of $n\lambda Q_{c\lambda}$

This is an increase of the link budget. Any of its elements is concerned :
- laser energy
- emission divergence
- retroreflector efficiency
- collector area
- filter transmission
- detector quantum efficiency

Subpicosecond timing devices.

Today the intrinsic limit of a SC is at the detection interface (photocathode). Getting down under this limit is bypassing this bottleneck. Out of a few possible principles, two are already tested.

◊ **Statistical event timer**

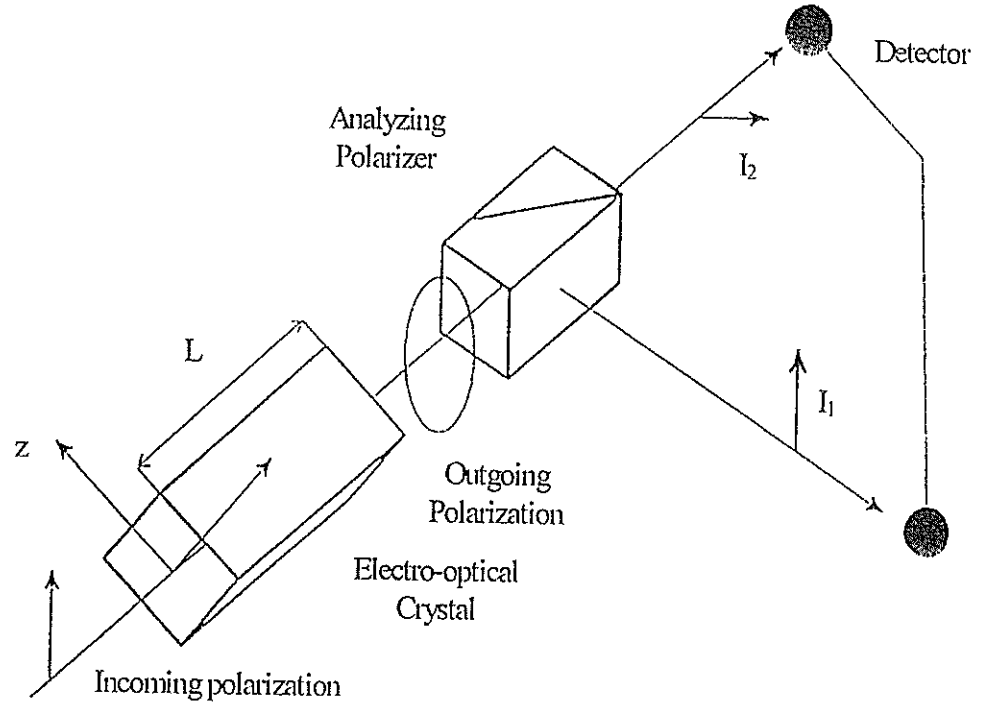Electro-optic crystal coupled with an analyzing polarizer (Fig. 2)

Figure 2 : Statistical event timer

The vertically polarized light pulse crosses the electro-optic crystal. A sinusoidal modulating voltage changes the crystal indexes and therefore the polarization state of the outgoing light pulse. An analyzing polarizer, here a Glan prism divides the outgoing light pulse in two components respectively polarized horizontally and vertically. The number of photons I_1 and I_2 allows to determine the polarization status of the crystal at the crossing moment and to determine this moment related to the sinusoidal modulation voltage.

Obviously this event timer is a multiphoton device and thus to be used in pair outphased by $\frac{\pi}{2}$ to avoid ambiguity. Around 500 photons are needed for a 50 ps time uncertainty. As such this kind of event timer could be used as an emission timing device where the number of photons could be very important.

The variations of the mirror reflectivity (electro-optic crystal and analyzer) could be achieved by other means.

As an example the ratio between the straight beam and the deflected one changes periodically as the fringes appear and disappear in an acousto-optic modulation. An event timer could be conceived around such devices.

◊ **Optical sweep**

The system could be described as a streak camera without the detection stage and the temporal dispersion of this photon to electron conversion. The propagating optical beam itself is deflected with a direct space to time relation. This deflection could be done by a prism whose indexes change with an electric field (Fig. 3). Already some crystals present this electro-optical sensitivity as lithium niobate (LiNbO$_3$) or strontium and barium niobate (SBN). Up to now the sensitivity is rather low ($\dfrac{\delta n}{n} \approx 10^{-3}$ kV.mm^{-1}).
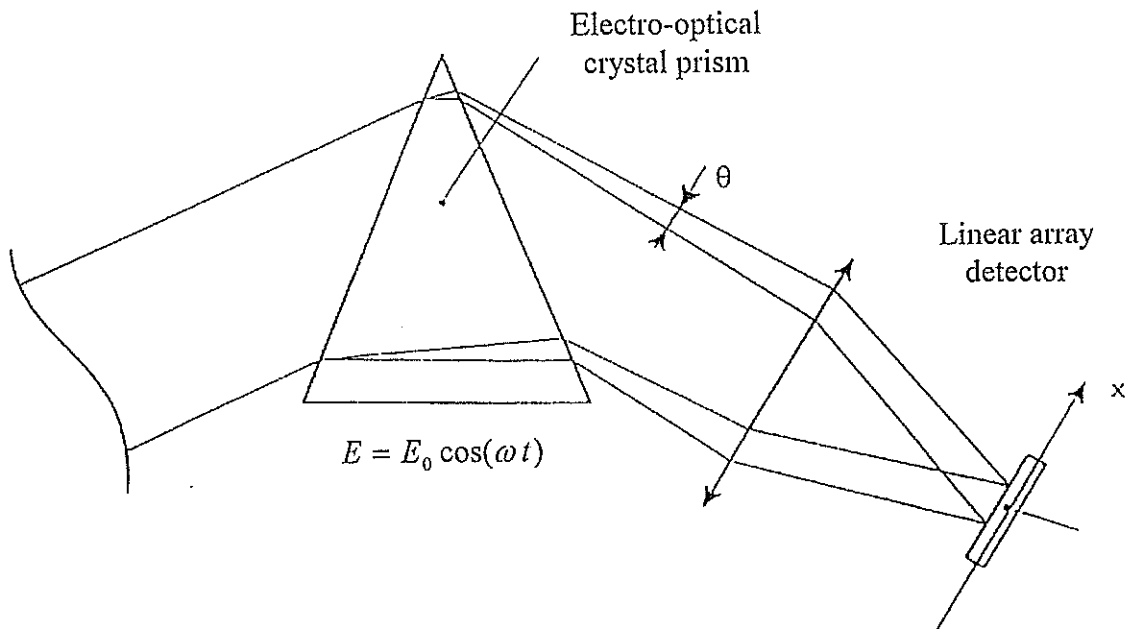
Figure 3 : Electro-optical Streak Camera

Conclusion

Two color laser ranging being a multiphoton process and needing a very high differential timing accuracy, very few stations are able to implement it.

Reducing the number of photons to achieve a good index correction is needed.
Two ways to achieve this are foreseen :
   ◊ Enhance the accuracy of the timing device
   ◊ Use the information potentially provided by each received photon.

The Circular Streak Camera Experiment of the WLRS

Stefan Riepl, Ulrich Schreiber
Forschungseinrichtung Satellitengeodäsie
Fundamentalstation Wettzell
D - 93444 Kötzting, Germany

Wolfgang Schlüter
Institut für Angewandte Geodäsie
Fundamentalstation Wettzell
D - 93444 Kötzting, Germany

Abstract

The Circular Streak Camera Experiment at Wettzell is nearing routine operation. By means of synchronizing the deflection voltage of the streak camera with the mode locking frequency of the Nd:YAG laser and locking both to a stable frequency standard, the streak camera represents a complete timing system allowing simultanous measurement of absolute pseudo ranges with an ambiguity of roughly $1m$ in the infrared and green wavelength domain. In addition to that the laser can be operated in semi train mode compensating the shortcomings of the relative insensitive S1–Photocathode, by integration of succeeding pulses. In order to calibrate the device, ranging to a local ground target was carried out. It is shown that a standard deviation of about 10 ps can be reached operating the device in multi photon mode, despite the fact that the laser is operated with 200 ps FWHM pulses. The analysis of the satellite laser ranging experiments show that this high precision can be reached as well in the earth to space propagation channel. Receiving the backscattered intensity distribution over time, the optical impulse response of the satellite can be reconstructed by further analysis of the data. Moreover, looking at the shot by shot detected signal strength in both wavelengths, atmospheric propagation and transmittance characteristics can be derived via time series analyses, showing agreement with theoretical results of electromagnetic wave propagation in turbulent media.

1 INTRODUCTION

There have been several attempts [5] [2] [1] to utilize streak cameras in satellite laser ranging in order to derive the atmospheric correction. As their time resolution can

be pushed beyond 1 ps, these devices seem to offer a good approach to improve the accuracy of laser ranging instrumentation. One major drawback of the up to now published techniques is that this precision is not obtained for the absolute range information but only for the range differences of two simultaneously emitted laser pulses of different wavelength. This drawback forbids the evaluation of streak camera measured differential ranges in terms of atmospheric delay corrections, assuming equal intensity distributions at both wavelengths, which doesn't hold for cross atmospheric propagation due to turbulence induced scintillation. The experimental setup allows both, the determination of absolute ranges, as well as the detection of range differences between laser pulses of the fundamental (1064 nm) and second harmonic (532 nm) Nd:YAG frequencies. Figure 1 illustrates the principle of operation. On the right hand side there is a schematic representation of an active and passive q-switched oscillator, emitting pulse trains of nominal 200 *ps* FWHM pulses. The driving frequency of the acoustooptic modelocker is generated by a synthesizer which is synchronized to a frequency standard. As a result the temporal separation of any two pulses is precisely an integer multiple of the reciprocal driving frequency. The streak camera sweep frequency is derived from the same synthesizer in order to synchronize the detector unit with the laser output pulses. The laser pulse train passes the slicer and several amplifiers and is frequency doubled before it is transmitted from the 75cm aperture WLRS telescope. After reflection by a target the laser pulses are collected by the same telescope and guided along the receive path. After passing the spatial filter the laser pulses are imaged onto the streak camera cathode. The resulting photoelectrons are deflected in two dimensions while being accelerated from photocathode to the microchannel plate. This plate emits secondary electrons that are detected at the phosphor screen by a CCD array. If t denotes the round trip time of a laser pulse, then the angular location Φ (see figure 1) can be expressed in terms of the driving frequency F by

$$\Phi = 2\pi t \bmod T, \quad T = \frac{1}{F}.$$ (1)

Expressing t in terms of a whole number N and the sweep period T, i. e.

$$t = T(N + \frac{\Phi}{2\pi}),$$ (2)

the round trip time can be measured by determination of N and Φ. In case of satellite ranging N is of the order of one million. So for round trip time measurements of 5 ps accuracy, the driving frequency of 140 MHz has to be known to 0.1 Hz. This requirement is met by the equipment. To moderate the drawback of the relative insensitive S1 photo cathode of the streak camera, the laser can be operated in semi train mode. This gives four times the intensity as operation in single pulse mode. The temporal spacing of the laser pulses equals exactly the sweep period of the streak camera. Therefore the succeeding pulses are imaged onto the same angular location

Φ on the phosphor screen, if the optical path can be considered as constant within 50 ns. This holds for all earth orbiting satellites.

2   RANGING TO GROUND TARGET

In order to test and calibrate the device with respect to the reference point of the telescope, ranging to a local ground target was performed. Figure 2 shows a histogram of detected peak locations. The abscissa is plotted in units of picoseconds, with an arbitrary origin. The ordinate shows the number of events in each bin. An event is obtained by averaging the CCD signal, which is proportional to the time varying intensity given by a laser pulse. An accuracy of 14 ps is obtained, although the laser pulses are 200 ps FWHM. However this timing performance is only reached when the intensity of the detected signal is quite high, i.e. the device is operated in multi photon mode. This is because the pulse shape of the laser is reproduced quite well, thus allowing a good determination of the centre of the pulse. The achievable accuracy, dependent on intensity, can be written as

$$\delta t = \sqrt{\delta t_i^2 + (\delta t_l e^{-\frac{I\eta}{a}})^2},\tag{3}$$

where δt_i refers to the intrinsic resolution of the streak camera, i.e. beam spread inside the tube etc., δt_l is the FWHM of the laser pulse, I its intensity, η the cathode's quantum efficiency and an empirical constant a which equals 2 in this case. From equation 3 one can see that a downgrade of the intensity to the detector's single photon mode ($I\eta = 1$) results in a loss of accuracy. This is shown in figure 3. The standard deviation is spread by a factor 8 in contrast to figure 2, but the RMS is still half as much as the laser pulse half width. Therefore it is assumed that reducing the laser pulse half width to 30 ps ensures an accuracy of 15 ps in single photon mode, as δt_i is always much smaller than the contribution of the laser to the error budget.

3   STREAK CAMERA SATELLITE RANGING

When ranging to satellites the effect of speckle patterns must be considered. In case of ground target ranging, the propagation distance is not large enough to develop proper phase fluctuations and the image is relative undistorted. When ranging to satellites two effects related to the turbulent atmosphere must be considered:

- The transmission of a laser pulse with homogenous intensity distribution results in a speckle structured intensity distribution at the location of the satellite (see

TATARSKI [10]). The mean diameter of a speckle is of the order of a Fresnel zone

$$d_0 = \sqrt{\lambda L}, \qquad (4)$$

where λ denotes the wavelength and L the propagation distance. Thus the intensity distribution has a random spatial modulation resulting in a wavelength dependent intensity scintillation of the backscattered laser light.

- Imaging a laser beam reflected by a satellite results in a speckle pattern comparable to those you get by imaging unresolved stars with short exposure time (see DAINTY [11]). The turbulent atmosphere introduces phase fluctuations in the electromagnetic phase fronts of the laser beam, which results in spatially spread images according to the current seeing conditions. The wavelength dependence of phase fluctuations is given in STROHBEHN [7]

$$D_S(\rho) \doteq 1.46 \frac{4\pi^2}{\lambda^2} C_n^2 L_{tur} \rho^{\frac{5}{3}}, \qquad (5)$$

where C_n denotes the refractive index structure constant, L_{tur} the propagation distance in turbulence and ρ corresponds to the separation between two points where the phase is evaluated. This also results in a random speckle pattern where one can find a characteristic size of the speckles, which is known to be of the order of a diffraction limited image of a point source (see DAINTY [11]).

In summary one can conclude that the satellite backscattered intensity is not necessarily correlated for two different wavelengths. Furthermore one has to bear in mind, that the satellite image, generated by laser illumination, is random spatially spread. Rigorous spatial filtering as suitable for high resolution streak cameras will lead to large attenuation of the transmitted intensity. So one ends up with a trade off between speckle induced pulse broadening and less representative pulse shape reconstruction due to a lower photoelectron level arising from spatial filtering. Keeping in mind that the spatial frequency of the satellite speckle image is higher for shorter wavelengths one introduces an additional wavelength dependent effect on the transmitted intensity by spatial filtering.

As experimental evidence, figure 4 shows a sample plot of a two color laser pulse reflected by satellite STELLA. The field of view was chosen wider than the seeing limit (5 arc seconds for Wettzell) so that there is no discrimination of the spread image intensity. The solid line shows the intensity as measured by the streak camera, the dashed line is a fit of the theoretical impulse response. The pulse on the left hand side refers to the infrared wavelength and shows good agreement with the theoretical impulse response, whereas the laser echo in the green wavelength on the right hand side shows a total different shape. The convolution theorem, as applied in speckle interferometry (DAINTY [11]), provides theoretical proof that speckle images of unresolved

stars can be deconvolved resulting in a nearly diffraction limited image. Given that the undistorted satellite image refers to an object intensity $O(\rho)$, which is a function of the two dimensional vector ρ in the image plane. Then a distorted short exposed image of the object taken at time t_n can be expressed as a function of intensity

$$I_{t_n}(\rho') = \int O(\rho)G_{t_n}(\rho',\rho)d\rho, \tag{6}$$

where G_{t_n} denotes the point spread function, which characterizes the random turbulent state of the atmosphere at time t_n and the imaging capability of the optical system. The latter is not discussed here. To apply this formalism to streak camera satellite laser ranging it is convenient to formulate the problem for a one dimensional object intensity. This is reasonable because the streak camera output is one dimensional too, representing a temporal intensity profile. By averaging over the spatial dimension being perpendicular to the deflection direction, validates the object intensity transformation from space to time according to

$$O(\rho) = O(tc) = o(t) \tag{7}$$
$$G_{t_n}(\rho',\rho) = G_{t_n}(t'c,tc) = g_{t_n}(t',t) \tag{8}$$

where c denotes the speed of light in vacuum. This leads to a temporal intensity distribution

$$i_{t_n}(t''') = \int \int \int o(t)p(t',t)s(t'',t')g_{t_n}(t''',t'')dtdt'dt'', \tag{9}$$

where convolution functions for the satellite temporal impulse response $s(t'',t')$ and for the laser pulse shape $p(t',t)$ have been added. In this case the streak camera is not able to resolve the spatial object intensity $O(\rho)$ of the satellite, now mapped onto a temporal scale by $o(t)$. So one can express $o(t)$ in terms of an infinitely narrow delta function leading to the simplified equation

$$i_{t_n}(t'') = \int \int p(t)s(t',t)g_{t_n}(t'',t')dtdt'. \tag{10}$$

Following REINECKE [4] a fourier transform to equation 10 is applied, which yields

$$\begin{aligned}
\tilde{i}_{t_n}(f) &= \int \int \int p(t)s(t',t)g_{t_n}(t'',t')e^{-2\pi i f t''}dtdt'dt'' \\
&= \int \int \int p(t)e^{-2\pi i f t}s(t',t)e^{-2\pi i f(t'-t)}g_{t_n}(t',t)e^{-2\pi i f(t''-t')}dtd(t'-t)d(t''-t') \\
&= \tilde{p}(f)\tilde{s}(f)\tilde{g}_{t_n}(f).
\end{aligned} \tag{11}$$

The point spread function is a random function of time. So its power spectrum approaches a time independent value when averaged over enough samples. For n samples taken at times t_n the intensity power spectrum is

$$\sum_n |\tilde{i}_{t_n}(f)|^2 = |\tilde{s}(f)|^2|\tilde{p}(f)|^2 \sum_n |\tilde{g}_{t_n}(f)|^2. \tag{12}$$

So with a known laser pulse shape $p(t)$, a given satellite impulse response function $s(t)$ and their Fourier transforms respectively, one can calculate the power spectrum of the point spread function by

$$\sum_n |\tilde{g}_{t_n}(f)|^2 = \frac{\sum_n |\tilde{u}_{t_n}(f)|^2}{|\tilde{s}(f)|^2 |\tilde{p}(f)|^2}. \tag{13}$$

This makes the study of the wavelength dependence of point spread functions feasible. The ability to measure the point spread function presents the opportunity of constructing an adaptive filter which may be applied in the time domain, removing noise and the effects introduced by the turbulent atmosphere.

4 RESULTS OF STREAK CAMERA SATELLITE RANGING

Because the streak camera is only capable of detecting modulo ranges with a one way ambiguity of roughly $1m$, a simultaneous additional range measurement is required to resolve this Ambiguity. This consists of a very sensitive avalanche photo diode [6], which is illuminated by the light leakage of a mirror in the optical receive path. The data gathered by this device was utilized to calculate the whole number part N of the ranges.

Due to the effect of image spread mentioned above the spatial filter was adjusted wider than the seeing limit. In the first experiments with satellites a centroid detection technique was used to locate satellite echoes in time. This was done by averaging the video signal, obtained by the streak-camera, over an area where the amplitude of the signal exceeds a threshold. Recovering the round trip time according to equation 2, one obtains the complete range information as shown in figure 5. For the correction of the atmospheric path delay caused by dispersion, the model of MARINI and MURRAY [3] was applied. The ordinate shows the residual ranges which remain after fitting the data to the satellite orbit, whereas the abscissa represents the elevation of the telescope in degrees. The plot shows the data corrected for the green wavelength, so the ranges measured in this wavelength domain are distributed around zero. The dashed curve refers to the path delay between green and infrared, according to the model of Marini and Murray. One can see that this model fits the infrared observations of the lower track quite well.

To analyze the distribution of collected returns more clearly, figure 6 shows two histograms over the residuals of figure 5, one corresponding to green the other to infrared data. The returns of the green wavelength show a higher standard deviation than those obtained in the infrared. This may be due to the speckle effect stated above,

as this measurement was taken with a wide field of view, and the speckle influences the green wavelength detection more than the infrared. The standard deviation in the infrared wavelength measurements nearly equals that obtained with the ground target experiment in single photon mode, shown in figure 3. For higher intensities an excellent resolution for satellite measurements could be obtained, which is comparable to that shown in figure 2.

5 SATELLITE IMPULSE RESPONSE RECON-STRUCTION

To reconstruct the satellite impulse response function of satellites by streak camera imaging, the same procedure as described above is used. The only difference is that record complete frames of intensity distributions is recorded, representing the backscattered intensity versa time within one ambiguity interval. After the removal of the streak sweep nonlinearity and the telescope invariant point correction, the frames are corrected due to the laser pulse time of flight, so that averaging the measured intensity distributions yield the satellite backscattered intensity. Averaging is applied for several reasons:

- Firstly the photoelectron level at the streak camera was found to be insufficient to reconstruct the response function of the satellite for every shot. Satellite ranging with the streak camera is still performed in single photon mode resulting in sharp peaked single photoelectron events rather than a continuous response function.

- The path delay of laser pulses reflected from different retroreflectors at the satellite causes interference of the electromagntic field at the receiver. This is the well known effect of target speckle (see DEGNAN[12]) and is due to the coherent nature of laser radiation. Introducing a diversity of satellite orientations, i.e. sampling the response function over a variety of path delay realizations, one approaches the incoherent response function.

- Due to the discrete satellite retroreflector distribution one can only find satisfying results when averaging over different satellite orientations. This permits the comparison of the measurement with the incoherent response function introduced by DEGNAN [12].

To check out the capability of measuring satellite impulse responses with the streak camera two rather different targets, AJISAI and STARLETTE were chosen. While AJISAI is about $2.2m$ in diameter STARLETTE is only $0.24m$, so there must be

Satellite	FWHM of Impulseresponse [ps]	
	1064nm	532nm
STARLETTE	245	258
AJISAI	483	403

Table 1: *Measured FWHM of impulse responses for the given wavelengths.*

a significant difference in the observed response function. Figure 7 shows the calculated incoherent impulse response function [12] for both satellites as well as the measured impulse response, averaged over all returns of one satellite pass. According to the calculation for the FWHM of AJISAI 564ps are expected, whereas STARLETTE should lead to a much sharper response of 266ps FWHM. This tendency is found in the observation for both wavelengths and is summarized in table 1. Due to the cut off effect because of the noise floor the measured values are below the ones predicted by theory. To investigate the spatial image spread caused by atmospheric turbulence as mentioned in section 3 with respect to the transmitted wavelength, the recorded streak image frames were Fourier transformed and averaged yielding the average power spectrum of the distorted intensity distribution $\sum_n |\tilde{u}_{t_n}(f)|^2$ as described by equation 12. The power spectra obtained were divided by the estimated power spectrum $|\tilde{s}(f)|^2|\tilde{p}(f)|^2$, namely the convolution of laser pulse shape and satellite response function, giving the power spectrum of the point spread function $\tilde{g}(f)$ for both wavelengths. The result is plotted in figure 8 as a function of normalized frequency for the same pass of STARLETTE as the average intensity was shown in figure 7. There is only negligible power in the low frequency domain corresponding to the frequencies occupied by the actual signal. Around 0.07 parts of the sampling frequency there is a significant peak for both wavelengths. This indicates the induction of higher frequency components in the measured intensity distribution by the point spread function. Moving up the frequency scale one can observe in principle an identical behaviour in both wavelengths, but there is a trend to higher power for higher frequencies in the 532nm wavelength domain.

6   INTENSITY TIME SERIES ANALYSIS

To characterize the transmittance properties of the atmosphere in terms of a turbulent medium the data obtained by the streak camera was subjected to further analysis. By averaging the intensity detected in each time channel where the satellite return was expected for every shot and wavelength, time series of satellite backscattered intensities are obtained for the time span of the satellite pass.

Figure 9 shows such a histogram of measured intensities. The probabilty $p(I)$ of measuring intensity I is given after GRACHERA [8] by the equation

$$p(I) = \frac{1}{\sigma_I \sqrt{2\pi}} \exp\left[-(\ln(\frac{I}{<I>}) + \frac{\sigma_I^2}{2})^2 (2\sigma^2)^{-1}\right], \qquad (14)$$

where σ_I refers to the normalized intensity variance. The dotted line in figure 9 represents equation 14 with mean and variance applied from the measurements taken. The model fits the observation quite well indicating that the atmosphere can be understood as a weak turbulent medium, i.e. $\sigma_I \ll 1$. For strong turbulence equation 14 should approach a Rayleigh probability distribution. Figure 9 was obtained from infrared data.

The treatment of the data obtained in the green channel lead almost to identical results with respect to the intensity probability distribution. However there are differences to be found looking at the time series. ISHIMARU [9] found an asymptotic solution for the power spectrum of the logarithmic intensity fluctuations in terms of the wind speed transversal to the optical path. The result for the low and high frequency limit is

$$\lim_{f \to 0} W_\chi = 0.8506 \frac{C_n^2}{V} k^{2/3} L^{7/3} \qquad (15)$$

$$\lim_{f \to \infty} W_\chi = 2.192 \frac{C_n^2}{V} k^{2/3} L^{7/3} (\frac{f}{f_0})^{-8/3}, \qquad (16)$$

where L denotes the path length in turbulence, C_n the refractive index structure constant and k the wave vector. In both limits there is a proportionality to the transversal wind speed V which acts as a transport mechanism causing the scintillation in intensity by shifting the turbulent cells across the beam path. In the presented case this turbulent transport is not due to the transversal wind velocity alone, but to the movement of the satellite tracking laser beam as well. In the high frequency limit, there is an additional dependence on the wind speed incurred by the factor

$$f_0 = \frac{V\sqrt{kL}}{2\pi}. \qquad (17)$$

This factor governs the frequency dependence of the power spectrum beginning at a certain cutoff, which is related to the transversal wind speed, or turbulent transport, as well. On the right hand side of figure 10 there is an illustration of the frequency dependence of equation 15 indicating a decay proportional to

$$\lim_{f \to \infty} W(f) \propto f^{-8/3}. \qquad (18)$$

On the left side there is a spectrum derived from satellite backscattered logarithmic intensities, where this behaviour can be found as well. According to equation 17 the

cutoff frequency at which the decay of power starts is a function of the transmitted wavelength. To provide experimental evidence figure 11 shows spectra of intensity time series obtained in the infrared and green channel. The wavelength dependent cutoff frequencies are marked by two arrows. As predicted by theory the cutoff frequency for $1064nm$ is lower than that for $532nm$. From the evaluation of two color satellite laser ranging point of view this indicates a higher variability of detectable intensity for shorter wavelengths. To analyze the correlation characteristics of intensity fluctuations of two different operating wavelengths it is convenient to derive the cross spectrum of these quantities (ISHIMARU [9])

$$Corr(\ln(I(\lambda_1)), \ln(I(\lambda_2), \tau) = \int\limits_{-\infty}^{\infty} \ln(I(\lambda_1, t)) \ln(I(\lambda_2, t + \tau)) dt \qquad (19)$$

and its Fourier transform respectively, the latter being called the coherence function

$$FT[Corr(\ln(I(\lambda_1)), \ln(I(\lambda_2)), \tau)] = \ln(I(\lambda_1, f)) \ln(I(\lambda_2, f))^*. \qquad (20)$$

Figure 12 shows the coherence function of the operating wavelengths obtained from a satellite pass of AJISAI. Again there is a sharp drop off in the area of $0.2Hz$. This is associated now with the loss of coherence of intensity fluctuations of the transmitted wavelengths. In other words, stable intensity relations between the two wavelengths can only be achieved if one averages for a time at least as large as the period associated with the cutoff frequency, i.e. 5 seconds in this case. The comparison of the correlation function obtained from two color measurements of satellites with different diameters allows an interpretation concerning the Fresnel zone mentioned in section 3. Figure 13 shows correlation functions of intensity fluctuations in different wavelengths obtained from STARLETTE and AJISAI passes. The correlation function is plotted versa the lag, labeled as τ in equation 19. The main fact which can be deduced from these measurements is that the detected intensities do not correlate for different wavelengths (correlation coefficients around 0.001). However it is quite astonishing why the correlation coefficients obtained from STARLETTE and AJISAI differ in sign for small lags around zero. For a satellite orbiting at a height of about $1000km$ the Fresnel zone is of the order of $1m$. So one finds that STARLETTE, being $0.24m$ in diameter, lies always within one Fresnel zone, wheras AJISAI, $2.1m$ in diameter, covers more than one Fresnel zone. This leads to the conclusion, that the observed effect can be interpreted in terms of aperture averaging at the satellite. Large diameter satellites are more suitable for two color laser ranging, giving better chances of simultaneous detection in different wavelength domains.

7 ACKNOWLEDGMENTS

References

[1] H. Hamal and I. Prochatzka, "Modular Streak Camera for Laser Ranging",*SPIE 1358,55*

[2] Th. Varghese, Chr. Clarke, Th. Oldham, M. Selden, Streak Camera Based SLR Receiver For Two Color Atmospheric Measurements, *Proceedings of 8th International Workshop on Laser Ranging Instrumentation*, (1992)

[3] J. W. Marini,"Correction of satellite tracking data for an arbitrary tropospheric profile", *Radio Science 7, 223-231*, (1972)

[4] M.Reinecke, H.Ruder: *Speckle Interferometrie*, Sterne u. Weltraum, 7, 246–255 (1977)

[5] U. Schreiber, S. Riepl, "Measuring atmospheric dispersion employing avalanche photo diodes", *Lidar Techniques for Remote Sensing, Chr. Werner, Editor, Proc. SPIE 2310, 2,*(1994)

[6] U. Schreiber, K. H. Haufe, J. F. Mangin, J. M. Torre and C. Veillet, "Operating the APD SP114 at the LLR station in Grasse", *Lidar Techniques for Remote Sensing, Chr. Werner, Editor, Proc. SPIE 2310,25,*(1994)

[7] J.W.Strohbehn, Editor, "Laser Beam Propagation in the Atmosphere", *Springer Verlag Berlin,*(1978)

[8] M.E.Grachera: *Similarity Relations and Their Experimental Verification*, in Laser Beam Propagation in the Atmosphere, Topics in Applied Physics, (J.W.Strohbehn, Editor), 25, Springer Verlag, Berlin, Heidelberg, New York 1978

[9] A.Ishimaru: *The Beam Wave Case and Remote Sensing*, in Laser Beam Propagation in the Atmosphere, Topics in Applied Physics. 25, Springer Verlag, Berlin, Heidelberg, New York 1978

[10] V.I.Tatarski: *The Effects of the Turbulent Atmosphere on Wave Propagation*, Israel Program for Scientific Translations Ltd., Keter Press, Jerusalem (1971)

[11] J.C Dainty: *Laser Speckle and Related Phenomena*, Spinger–Verlag, Berlin, Heidelberg, New York (1975)

[12] J.J. Degnan: *Millimeter Accuracy Satellite Laser Ranging: A Review.* Geodynamics Series 25
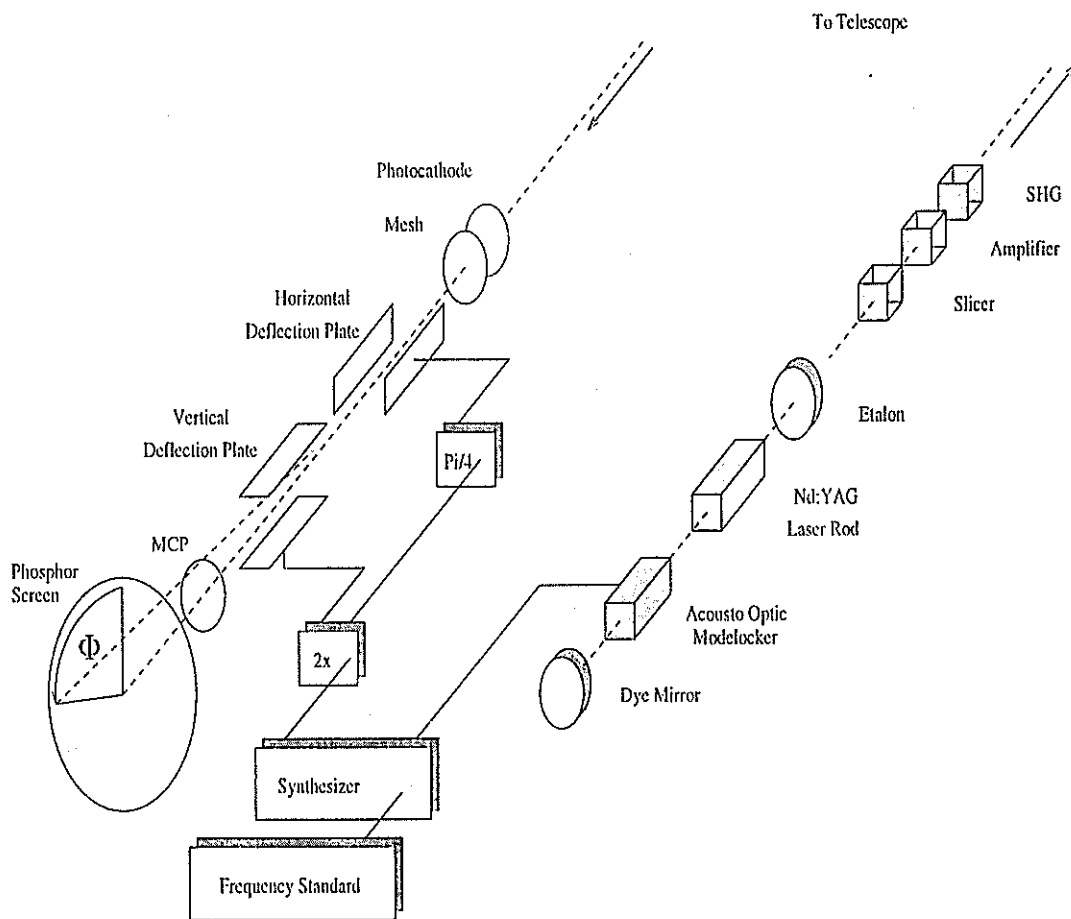
Figure 1: Experimental setup of satellite modulo ranging. The modulo range is measured in terms of the angular location Φ of photo electron traces on the phosphor screen of the streak camera.
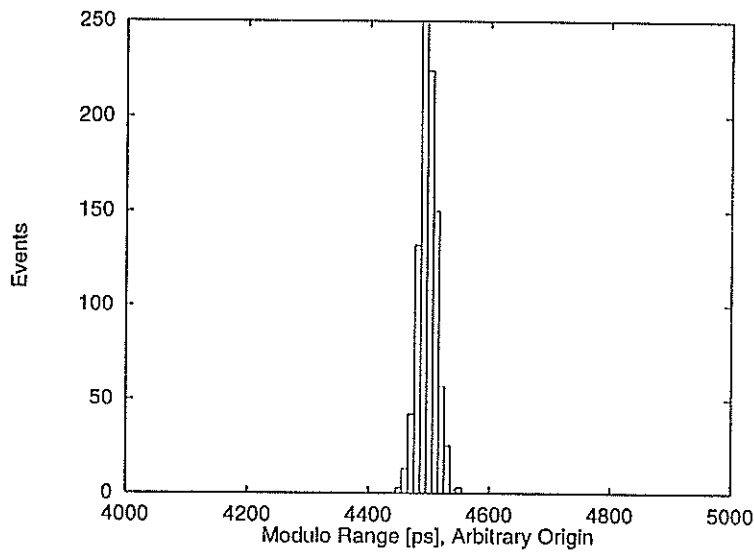
Figure 2: Histogram of 1064 nm ground target echoes. The device was operated in multi photon mode. A RMS of 14 ps was obtained.
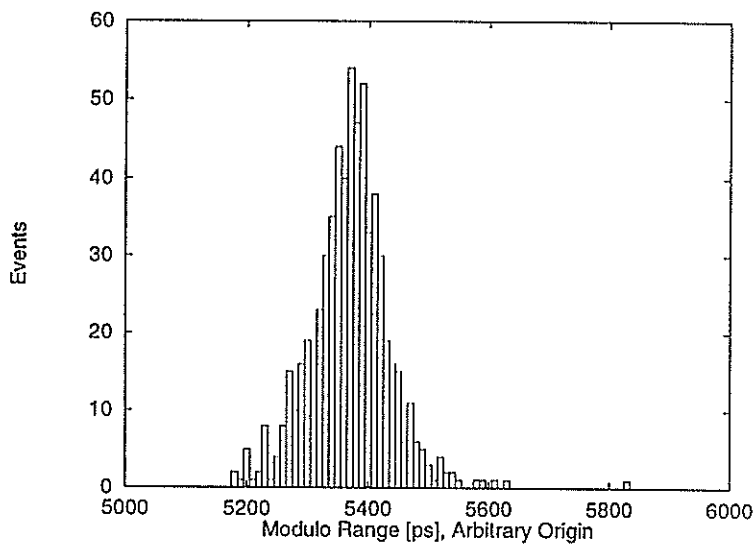
Figure 3: Histogram of 1064 nm ground target echos. The device was operated in single photon mode. A RMS of 90 ps was obtained.
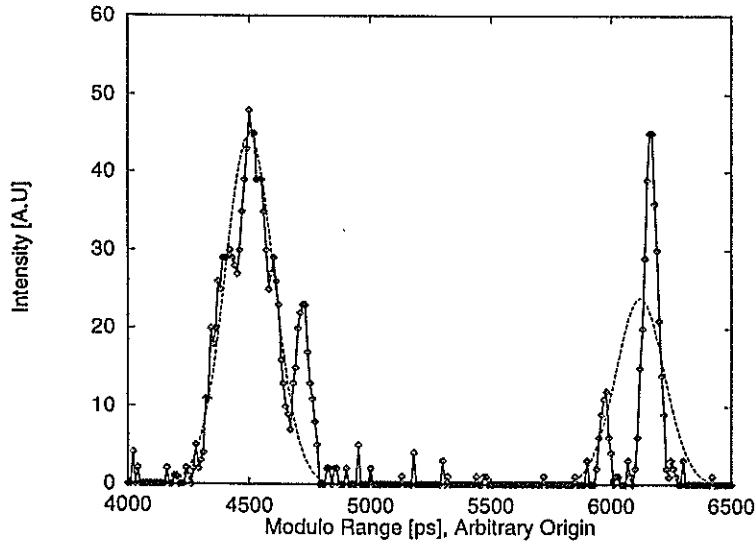
Figure 4: Dual color signal reflected from satellite STELLA. The solid line shows the infrared laser pulse on the left and the green laser pulse on the right side. The dashed line is the theoretical pulse response normalized to the intensity detected in each channel.
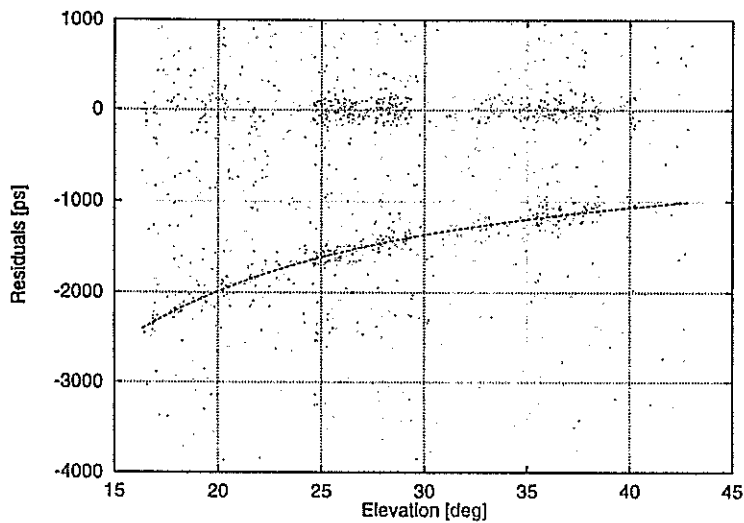
Figure 5: Range residuals obtained from ERS1 as a function of elevation. The upper trace corresponds to 532 nm, the lower trace to 1064 nm echoes. The dashed line indicates the dispersive delay predicted from surface meteorological data.
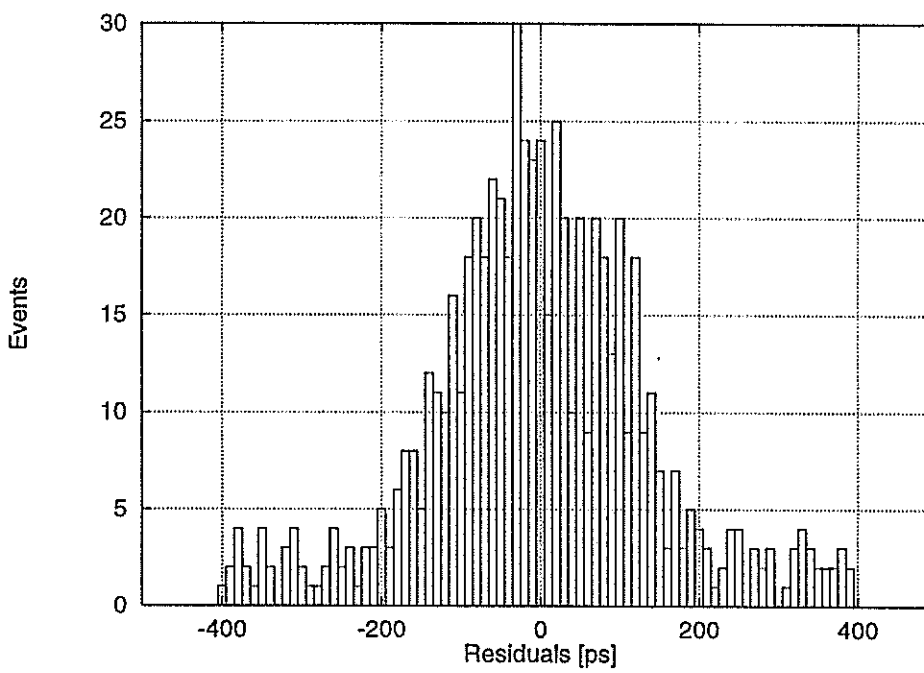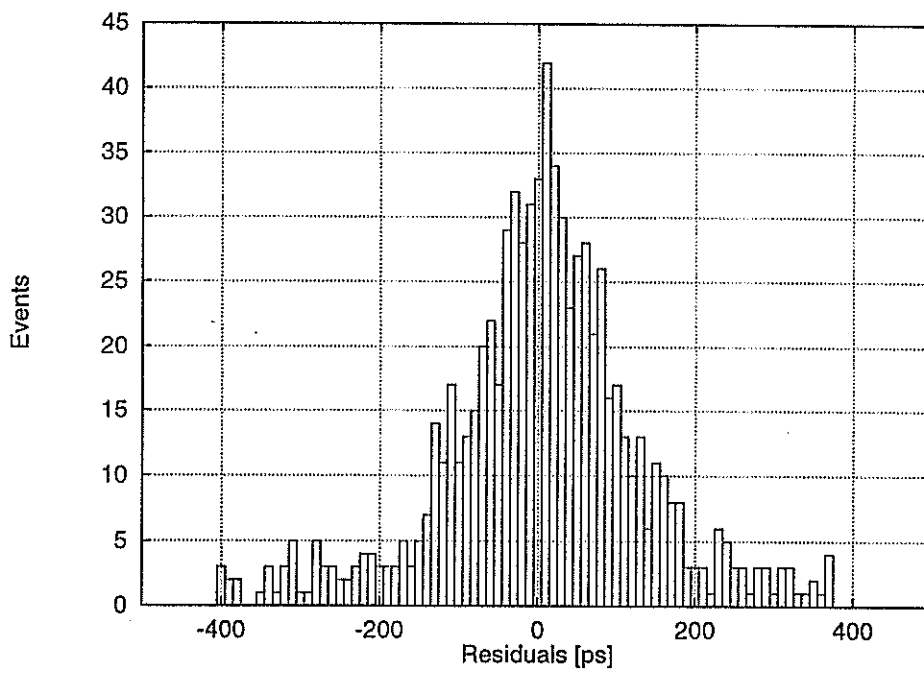
Figure 6: Residual histogram of 1064 nm (top) and 532 nm (bottom) echos, reflected by satellite ERS1

465
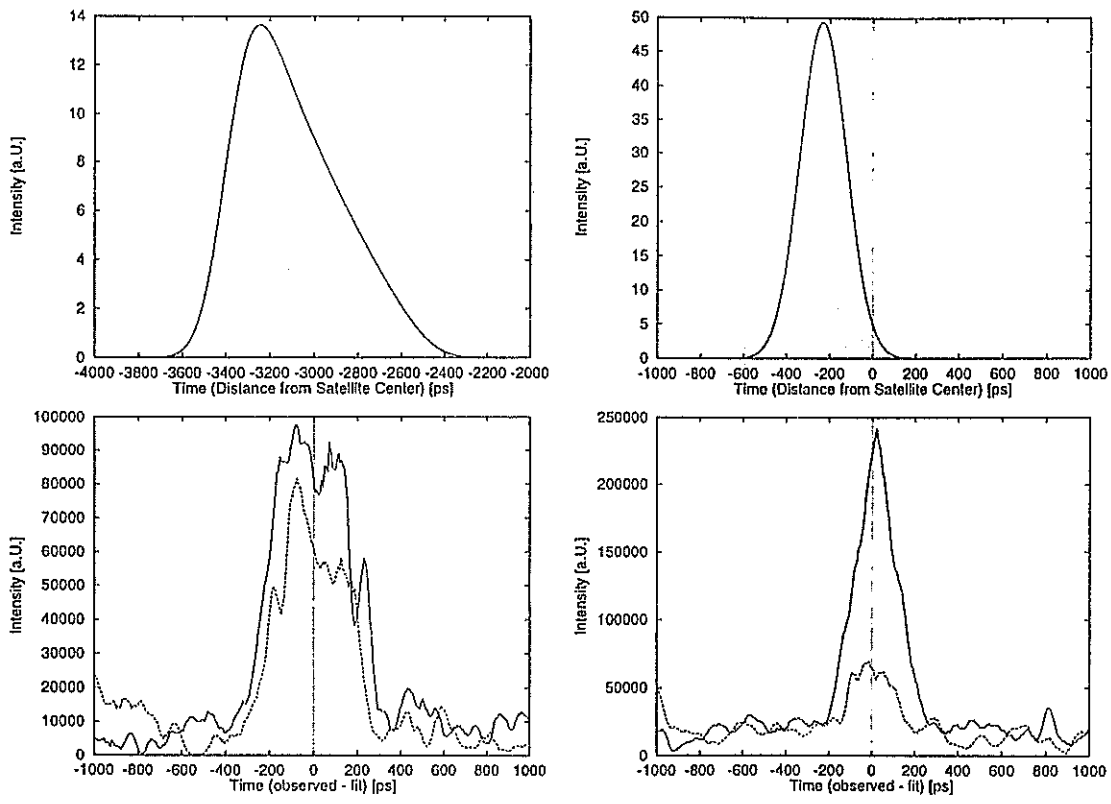
Figure 7: Theoretical impulse response function of satellite AJISAI (top left) and STARLETTE (top right) in contrast to measured impulse response (bottom left and right).
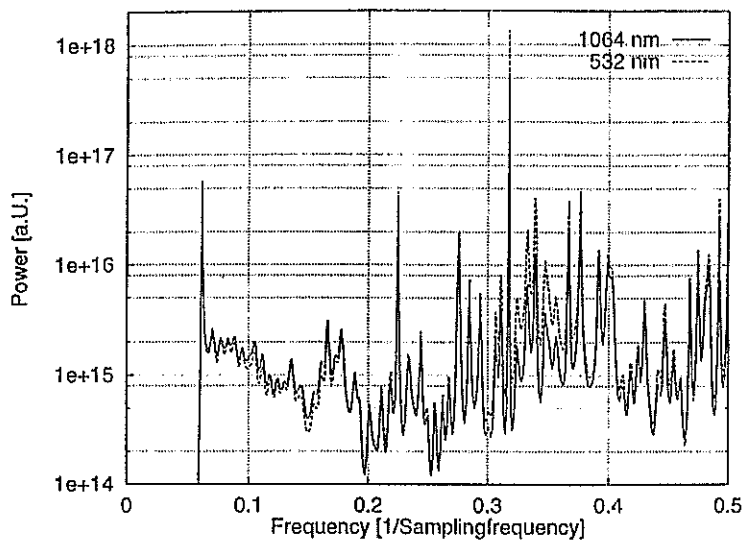
Figure 8: Power spectrum of point spread function obtained from satellite STAR-LETTE. The power spectral estimation was performed on the data that lead to the measured impulse response function shown in figure 7.
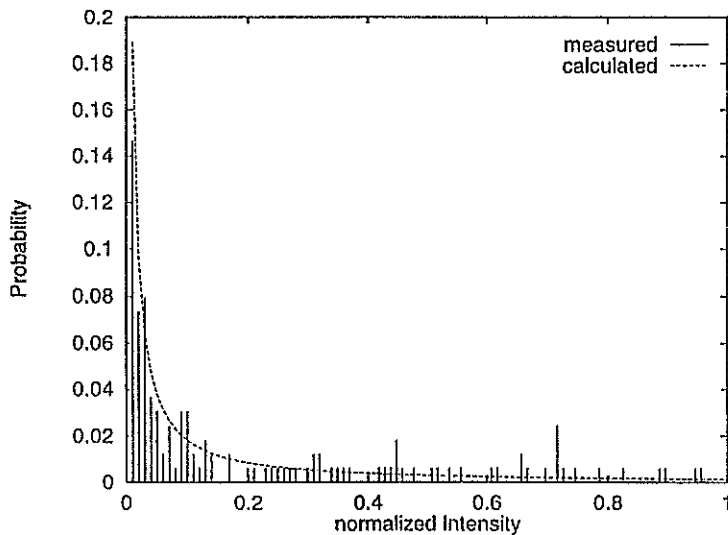
Figure 9: Histogram of detected shot by shot intensities in the infrared obtained from satellite AJISAI. The dashed line represents the theoretical expectation according to equation 14.
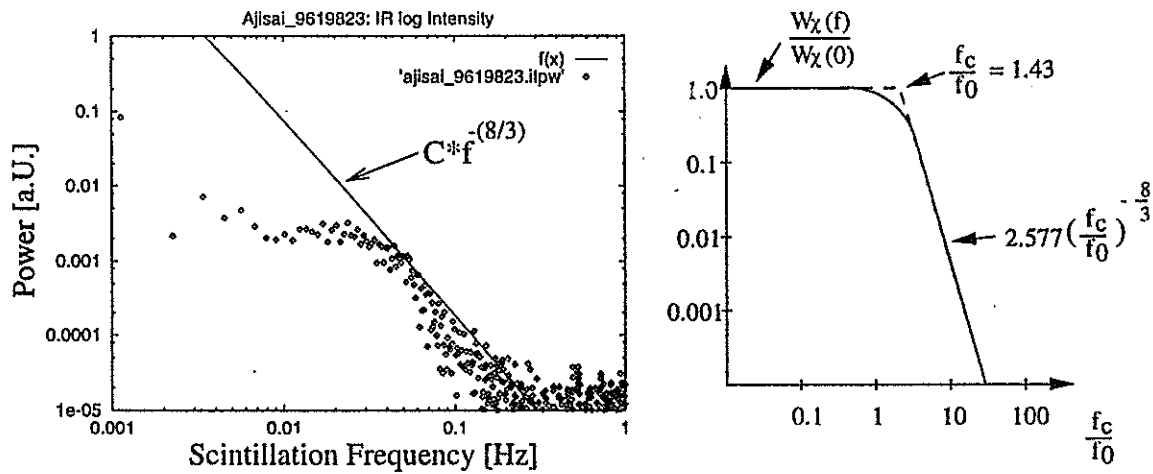
Figure 10: Frequency behaviour of the log intensity power spectrum: The left plot is obtained from measuring satellite backscattered intensities, whereas the right plot illustrates the theoretical frequency behaviour derived by ISHIMARU [9].
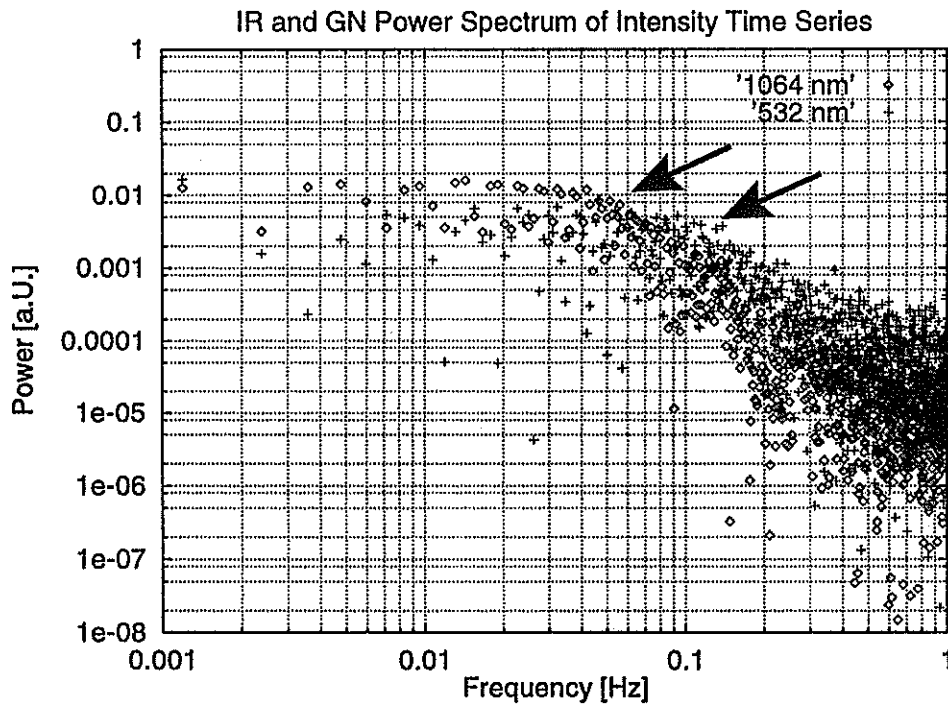
Figure 11: Power spectra of intensity fluctuations obtained from two color measurement to satellite AJISAI in the infrared and green wavelength domain. The arrows indicate the wavelength dependent cutoff where the power starts to decay with frequency.
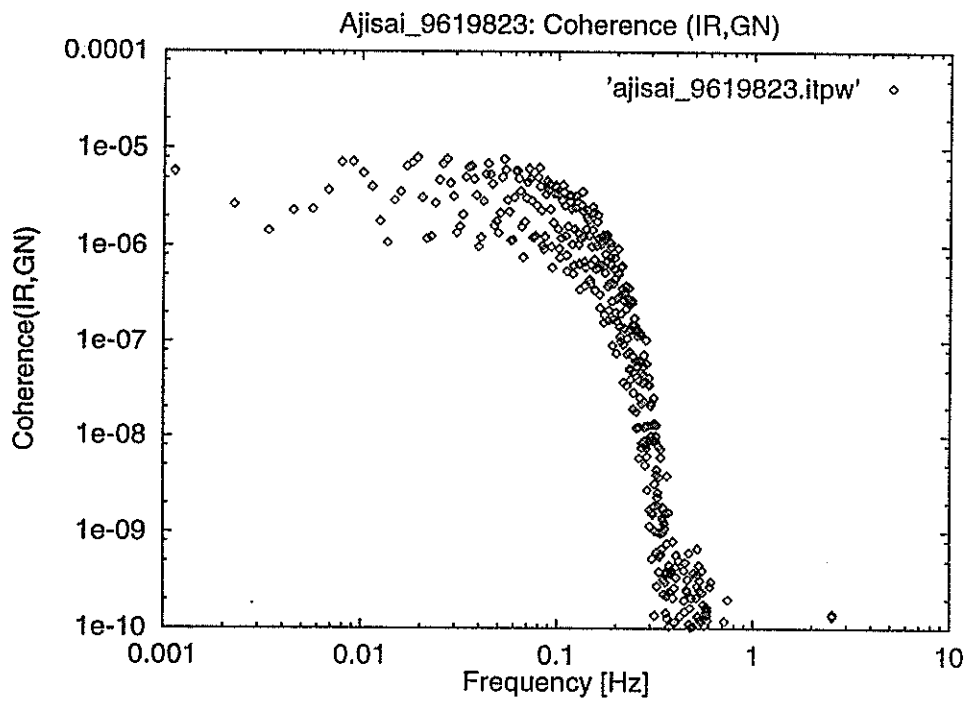
468

Figure 12: Coherence function of intensity fluctuations obtained from two color intensity time series measured during an AJISAI pass.
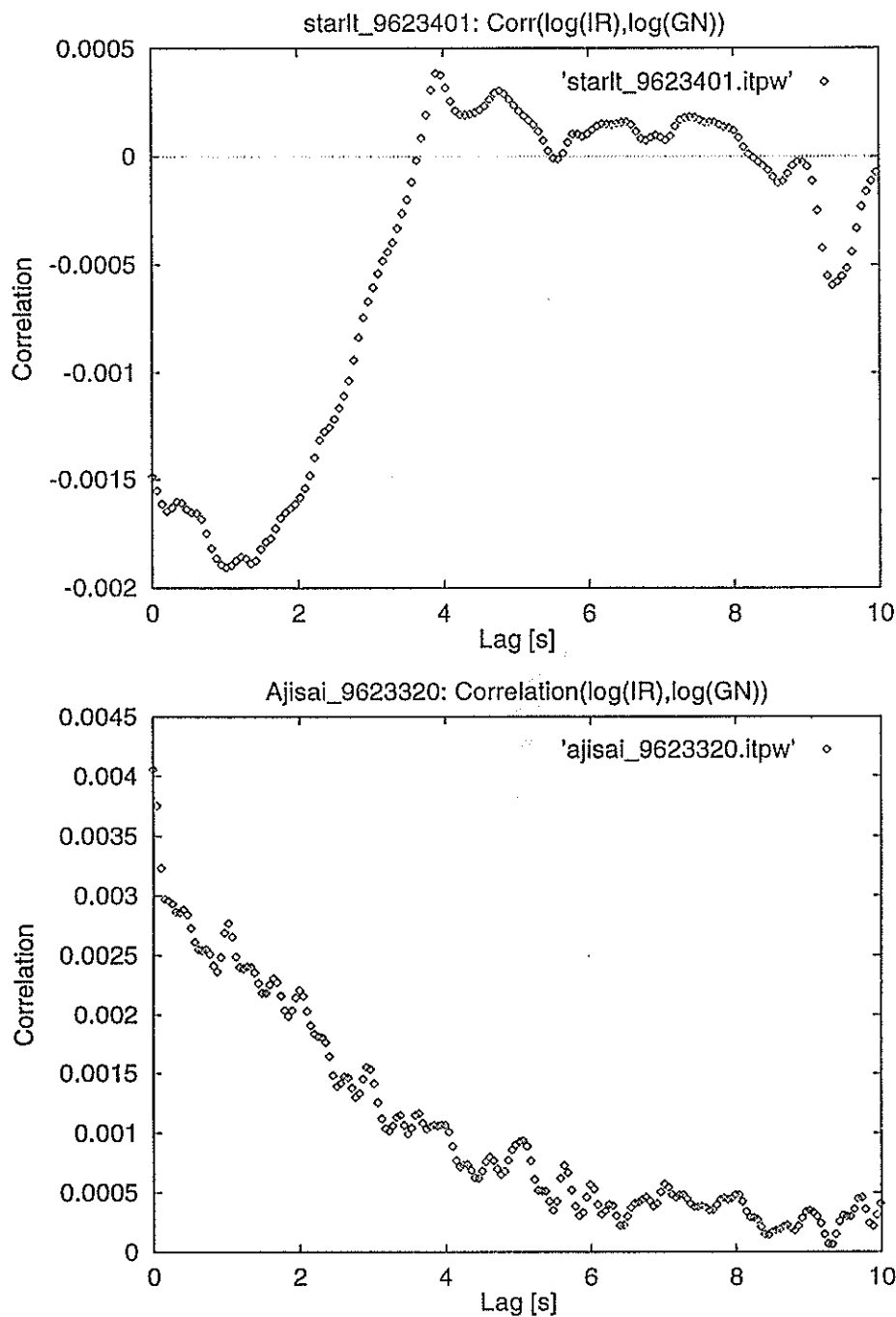
Figure 13: Correlation of intensity fluctuations of different wavelengths obtained from two color measurements to satellites of differing diameters. STARLETTE shows a slightly negative correlation at lag 0, whereas AJISAI shows a slightly positive correlation. This may be interpreted in terms of the Fresnel zone size (see text).

Water Vapour Correction of Two-Colour SLR

Reinhart Neubert

GeoForschungsZentrum Potsdam, Div.1: Kinematics and Dynamics of the Earth
Telegrafenberg A17, D-14473 Potsdam, Germany
Tel.: (49)-331-288-1153, Fax.: (49)-331-288-1111, e-mail: neub@gfz-potsdam.de

Introduction

The dispersion method to determine the atmospheric delay for SLR is now near to become practicable. At this stage we want to return to a principal systematic error source: the water vapour content of the atmosphere. As pointed out by Greene and Herring [1] using ray tracing calculations, insufficient knowledge of the atmospheric water vapour content may cause an error of more than 6 millimeters. This could partially explain the systematic effects observed in two-colour SLR by Schreiber et al. [2].
In this paper we first estimate analytically the influence of water vapour on the two-colour SLR results. In the remaining part we discuss the status of different remote sensing techniques for atmospheric water vapour.

Estimation of the influence of water vapour on SLR

For simplicity we regard the range correction $R(\lambda)$ for the zenith only:

$$R(\lambda) = \int_0^H (n-1)dh = f_d(\lambda) \cdot M_d + f_w(\lambda) \cdot M_w$$

Eq.1

where:

$$M_d = \int_0^H \rho_d(h)dh \qquad ; \qquad M_w = \int_0^H \rho_w(h)dh$$

Eq.2

are the total air masses of the dry and water vapour component, respectively. The integrals are taken from the station level to the satellite. The dimension and order of magnitude of the quantities are given in Tab.1:

Table 1: Approximate numerical values for the refractivities and air masses

Quantity	fd(0.53µm)	fw(0.53µm)	Md	Mw	fd Md	fw Mw
Unit	m³/kg	m³/kg	kg/m²	kg/m²	mm	mm
Numerical value	0.0002362	0.0003275	10 000	30 (very variabel)	2362	9.8

It can be seen that at optical frequencies the contribution of the water vapour to the zenith delay is about one centimeter only.
As has been shown by Saastamoinen [3], the total air mass M=Md + Mw can be estimated with high accuracy from the surface pressure using the fact that the atmosphere is near to hydrostatic equilibrium:

$$M = p / g_m \quad ; \qquad g_m = \dfrac{\displaystyle\int_0^\infty g(h) \cdot \rho(h) dh}{\displaystyle\int_0^\infty \rho(h) dh}$$

Eq.3

where p is the total pressure and g_m is the mean gravity computed from the height-dependent gravity g(h) using the air density as a weighting function. Thus, regarding the total air mass as a known quantity, it is useful to rewrite Eq.1 into the form:

$$R(\lambda) = f_d(\lambda) \cdot M + (f_w(\lambda) - f_d(\lambda)) \cdot M_w$$

Eq.4

Eq.4 is the kernel of the commonly used Marini-Murray formula [4]. The water vapour term in Eq.4 is proportional to the difference of the refractivities of water and dry air. This explaines the rather weak dependence of the Marini-Murray correction from humidity.
The first term in Eq.4 is called the hydrostatic term. Sometimes it is referred to as the dry component, although it contains a large part of the water vapour contribution.

The main idea of the dispersion method in optical distance measurement is to determine the refraction correction from measurements at different wavelengths directly becoming free from any assumption on the distribution of the atmospheric density. From two-colour ranging we can determine the range correction if the water vapour content is known. Adding a third optical or near infrared wavelength permits the dry and wet components to be separated, theoretically. However, the required range resolution of the three-colour method is too high to be realistic.

Introducing two wavelengths into Eq.1, we can derive the following relation by eliminating M_d

$$R(\lambda_1) = F(\lambda_1, \lambda_2) \cdot (R(\lambda_1) - R(\lambda_2)) + G(\lambda_1, \lambda_2) \cdot f_w(\lambda_1) \cdot M_w$$

Eq.5

where:

$$F(\lambda_1, \lambda_2) = \dfrac{f_d(\lambda_1)}{\left(f_d(\lambda_1) - f_d(\lambda_2)\right)} \quad ; \quad G(\lambda_1, \lambda_2) = 1 - \dfrac{f_d(\lambda_1)}{f_w(\lambda_1)} \cdot \dfrac{f_w(\lambda_1) - f_w(\lambda_2)}{f_d(\lambda_1) - f_d(\lambda_2)}$$

Eq.6

The first term in Eq.5 is the most important and depends on the differential range only. The sensitivity factor F is of the order 10 to 20 depending on the wavelength pair used. For high accuracy a small F-number is essential. The second term in Eq.5 describes the influence of the water vapour. The water vapour mass M_w must be known from some independent source with a precision depending on the sensitivity factor G (Eq.6). This factor is very weakly depending on the choice of the wavelength pair (Fig1).
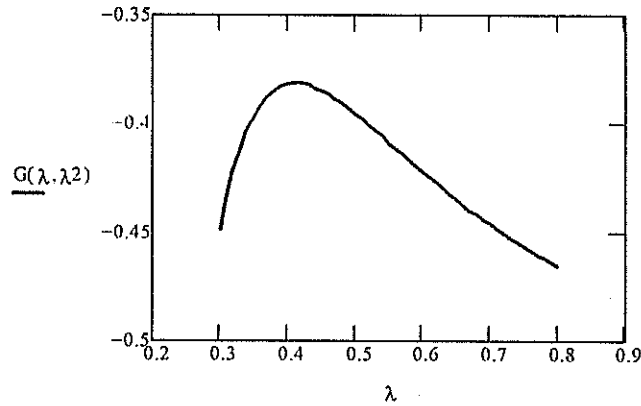
Fig.1: The sensitivity factor G versus the short wavelength (nm), if the 2nd wavelength is fixed at 1.06 µm.

If the fundamental and 2nd harmonic of Nd-YAG is used, G is about -0.4. The negative sign of G means that the range correction will be overestimated if the water vapour correction is neglected.

It migth be interesting to look at the influence of water vapour on the Marini-Murray correction, based on surface data and the assumption of hydrostatic equilibrium. For this purpose we rewrite Eq.4 :

$$R(\lambda) = f_d(\lambda) \cdot M + G'(\lambda) \cdot f_w(\lambda) \cdot M_w \qquad \text{where} \quad G'(\lambda) = \frac{f_w(\lambda) - f_d(\lambda)}{f_w(\lambda)}$$

Eq.7

This form is fully analogous to Eq.5. The water sensitivity factor G' in Eq.7 is again nearly independent from the wavelength and for the 2nd harmonic of Nd-YAG equal to 0.28. The positive sign of G' means that the hydrostatic term in Eq.5 or 7 is underestimating the range correction (this is because the refractivity of water vapour is higher than the refractivity of dry air). The conclusion of this comparison is: two-wavelength ranging is sligthly more dependent on the water vapour than the Marini-Murray formula. If the water vapour mass according to Table 1 (30 kg/m²) is adopted, we calculate the water correction term in Eq.7 to be 2.7 mm. Therefore, very rough estimates of the water mass are sufficient to be comparable with other model errors of the Marini-Murray formula.

Main aim of two-colour SLR is to obtain the range correction with higher accuracy than possible with the hydrostatic model using the surface pressure. It is believed that from surface pressure the zenith range correction can be obtained with an error of less than 1 cm. To justify the effort connected with two-colour ranging, we set the accuracy requirement of the water vapour correction to 1 mm. This corresponds to the knowledge of the water vapour mass with an error of 7.6 kg/m² or less. It is quite a low accuracy, but not reliably obtained using surface data only.

How we can get the water vapour mass?

There is a lot of efficient techniques available now achieving the accuracy requirement for SLR. One of the most promising sources is GPS. It has been shown that from the GPS residuals the water vapour content can be retrieved with sufficient accuracy [5..7]. The main reason for this is the high refractivity of water vapour for radio waves. The idea can be described as follows: The

473

zenith range correction can be treated as an unknown parameter in the least square analysis of the GPS data. This gives reasonably accurate estimates if some conditions are fulfilled: simultaneous tracking of many satellites at different elevations, inclusion of sufficient well-distributed GPS receivers, careful modelling of all instrumental effects (e.g. antenna phase center variations). The angular dependence of the atmospheric delay has to be modelled. It is assumed to be independent from azimuth in general. Introducing now surface weather data (mainly pressure), the dry and wet components of the atmospheric delay can be separated.

It has been demonstrated by comparison with other techniques that the GPS-derived water vapour masses are usually accurate within 10 per cent. As an example, we show some results obtained during a test campaign in May/June 1994 [8]. In this field test two GPS receivers, two microwave radiometers as well as a new high resolution solar spectrometer were included. The two microwave radiometers were kindly made available by B.Bürki from ETH Zürich. The measurements were taken simultaneously at GFZ Potsdam and the research campus Berlin-Adlershof. Fig.2 shows the comparison between GPS and the water vapour radiometers at both sites.
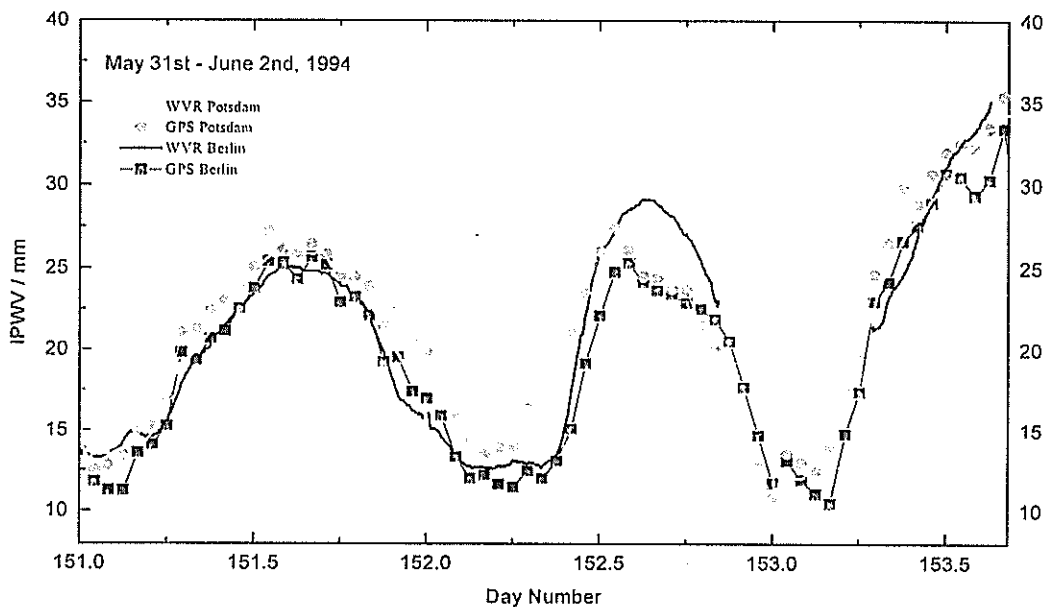

Fig.2: Integrated water vapour above the two test sites from May 31st until June 2nd estimated from GPS and measured by water vapor radiometers (WVR), from [8]

In Fig.2 the integrated precipitable water (IPW) in mm is given. This quantity is numerically identical with the columnar water vapour mass in kg/m^2. It can be seen that the deviations between both methods are smaller than the error limit of the radiometers (5%) in general, except for Berlin at day number 152.7. This isolated discrepancy could be attributed to the GPS method referring to the results of high resolution solar spectroscopy. This method which could be developed to a benchmark, consists in the observation of well isolated vibrational-rotational absorption lines of water vapour. This test has been done in cooperation with the Laboratorium fuer spektroskopische Methoden der Umweltanalytik, Berlin-Adlershof, using a double echelle spectrograph described in [9]. An example absorption spectrum is shown in Fig.3. The advantage of using high resolution in contrast to the commonly used broadband solar photometry is that there is no overlap with absorption from other atmospheric gases and that the background can be assumed to be constant within the small wavelength range. This allows simple models to be used

to retrieve the water vapour content from the spectra. The only parameters required are the laboratory-measured spectroscopic constants of the individual lines.
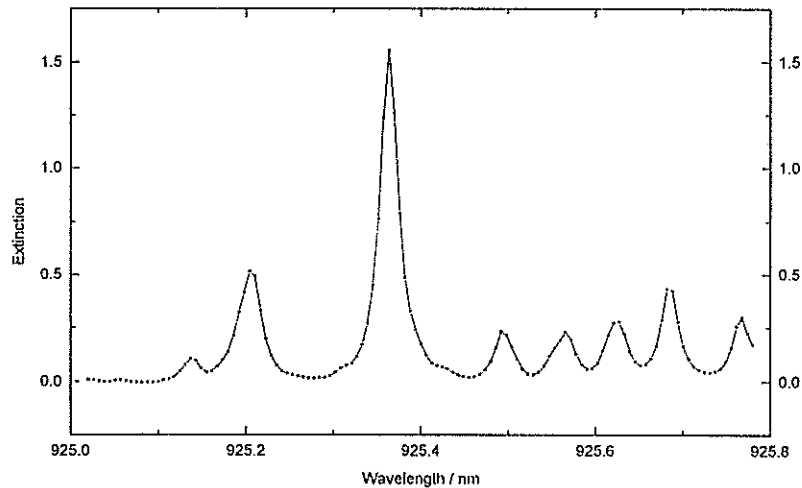

Fig.3: Typical absorption spectrum of water vapour in a small near infrared window of 1 nm width, (from [8])
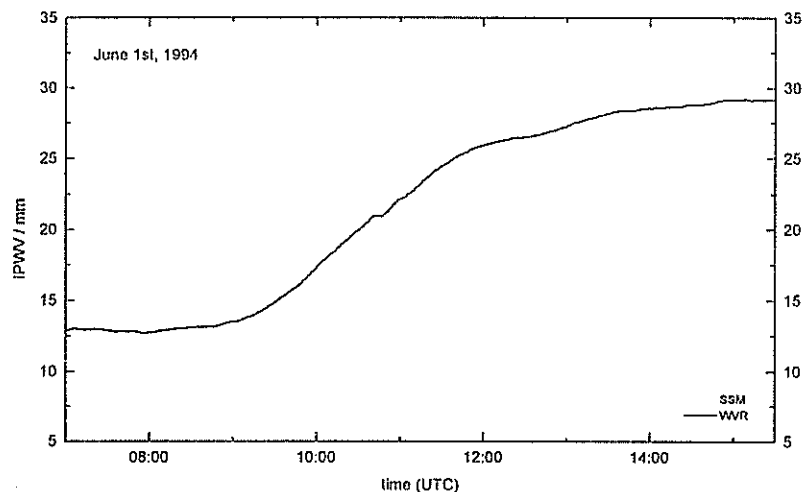

Fig. 4: Integrated water vapour for June 1st, 1994 measured by a water vapour radiometer (WVR) and a solar
      spectrometer (SSM) in Berlin-Adlershof , (from [8])

The last Fig.4 shows a comparison between the microwave radiometer and the optical spectrometer for June 1st in Adlershof. The differences are within the error limits of the radiometer. On this day GPS is giving significantly lower values (Fig.2). Because of the good agreement of the other methods it is believed that the deviation is due to the GPS method in this example. Fig.4 is interesting because of the strong change of the water vapour content within a few hours. In this case the weather data measured at the surface did not indicate a significant change of the water vapour. This demonstrates clearly that the surface data are insufficient for estimating the integrated water vapour content reliably.

Conclusion

- two-colour SLR measurements need to be corrected for water vapour
- surface weather data are not sufficient to do this correction
- a cost-effective and sufficiently accurate method for water vapour determination
  is GPS-meteorology
- high resolution optical absorption spectroscopy can be used as a benchmark to
  calibrate/control the GPS method and/or microwave radiometry

References

[1] B.A.Greene, T.A.Herring: Multiple Wavelength Laser Ranging, Proc. 6th Workshop on Laser Ranging Instrumentation, Antibes, Sept.22-26, 1986, p.581

[2] U.Schreiber, W.Maier, S.Riepl, K.H.Haufe: Measuring Atmospheric Dispersion Employing Avalanche Photo Diodes, Proc. 9th Workshop on Laser Ranging Instrumentation, Canberra Nov. 7-11, 1994, p.615

[3] J.Saastamoinen: Contributions to the Theory of Refraction, Bull. Geod. 105, p.279, 1972

[4] J.W.Marini, C.W.Murray jr.: Correction of Laser range Tracking Data for Atmospheric Refraction at Elevations above 10 Degrees , NASA Techn. Report X-591-73-531, 1973

[5] M.Bevis, S.Businger,T.A.Herring, Ch.Rocken, R.A.Anthes, R.H.Ware: GPS Meteorology: Remote Sensing of Atmospheric Water Vapor Using the Global Positioning System, JGR Vol.97, 1992, pp.15787-15801

[6] M.Bevis, S.Businger: GPS Meteorology and the International GPS Service, in: IGS Workshop 'Special Topics', Potsdam, May 1995

[7] G.Gendt: Estimation of tropospheric water vapor content by ground-based GPS receivers in: Field Campaign LINEX 96/1 : Water Vapor Observation with different Remote Sensing Techniques from April 15th to May 13th at Meteorological Observatory Lindenberg, Deutscher Wetterdienst, Arbeitsergebnisse Nr.39, Offenbach 1996

[8] B.Sierk, B.Bürki, H.Becker-Roß, S.Florek, R.Neubert, H.-G.Kahle: Tropospheric Water Vapour Derived from Radiometer, Solar Spectrometer and GPS Measurements, submitted to JGR

[9] H.Becker-Ross, S.Florek: High-resolution Spectrometer for Atomic Spectrometry, J. Anal. At. Spectrom., Vol. 10, p. 145, 1995

Acknowledgement

ATMOSPHERIC DISPERSION MONITORING
USING 0.53 um AND 1.54 um SATELLITE LASER RANGING

B.Greene
Electro Optic Systems, Pty.Ltd., Queabeyan, NSW, Australia

H.Kunimori
Communication Research Laboratory, Tokyo, Japan

K.Hamal, I.Prochazka
Czech Technical University, Prague, Czech Republic

Several attempts have been made to contribute to the existing atmospheric dispersion and optical signal propagation delay models using picosecond high precision multiple wavelength Satellite Laser Ranging (SLR) in visible region [1]. We are reporting, to our knowledge for the first time, on the two wavelengths SLR in visible at 0.53 um and in the near infrared at 1.54 um.

The SLR Observatory in Tokyo, Japan employs 1.5 meter aperture telescope. The NdYAG laser delivering 200 mJ in 140 picosecond pulses at 1.064 um is split in two beams; a second harmonic generator transmites 30 mJ at 0.53 um, the second one entering the Raman cell filled by Methane delivers 6 mJ at 1.54 um. The receiver package consists of two detectors. The Silicon based Single Photon Avalanche Diode (SPAD) detects the signal at 0.53 um. The Germanium based SPAD cooled to 77K detects the reflected signal at 1.54 um. The detectors quantum efficiency estimate is 15 % at each wavelength, their output signals in NIM form are registered in Picosecond Timing System with 10 picoseconds resolution and processed in Master Ranging Control System. The single shot temporal resolution of the entire laser ranging chain is limited by the laser pulse duration to 100 psec. The results of laser ranging to several satellites equipped by retroreflectors and orbiting at the altitudes 1 000 to 20 000 km are summarized on Figure 1, where the two wavelengths time interval is plotted as a function of satellite elevation above the horizon. The solid curve represents the Marini Murray model [2]. No discrepancy has been detected on the present resolution.

Figure 1 The 0.53 um and 1.54 um wavelength differential delay versus elevation above the horizon basen on ranging to Topex, Lageos2 and Ajisai satellite. Solid line Marini Murray model.

[1]   I.Prochazka,K.Hamal,G.Kirchner, Technical Digest of the Conference on Lasers and Electro Optics CLEO'94, Anaheim, CA, May 1994,55 (1994)
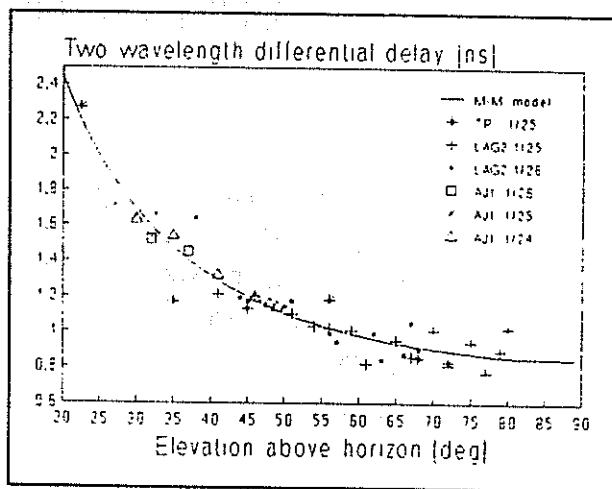
[2]   J.B.Abshire, App.Opt. Vol.19, 3436-3440 (1980)

GOALS
Subcentimeter eye safe laser ranging

- subcentimer satellite laser ranging

- eye safe operation 1.54 um

- two wavelength operation 0.53 & 1.54 um

- single photon detection

- prerequisite for system automation

KunimoriGreeneGuilfoyleHamalProchazkaKirchnerKoidl

Eyesafe Laser Ranging
ENERGY BUDGET LINK

0.53 : 1.54

	0.53 : 1.54
laser energy (mJ)	35 : 5
beam divergence	1 : 1
receiver FOV (arcsec)	12^2 : 8^2
detector QE (%)	15 : 5
T/R optics	1 : 2
photon energy	3 : 1
	----------
total machine	7 : 1
satellite cross sect.	
atmospheric transm.	
satellite ranging	8 : 1

Kunimori, Greene, Hamal, Prochazka, '96

SECOND HARMONIC BASED T/R SWITCH

K.Hamal

Czech Technical University, Brehova 7
115 19 Prague 1, Czech Republic
## fax +42 2 85762252, prochazk@mbox.cesnet.cz

B. Greene

Electro Optics Systems, PtyLtd, Queanbeyan,NSW, Australia

There are several schemes to realize a Transmit / Receive (T/R) for the coaxial SLR Coude optics, in particular the rotating disc, aperture sharing etc. Reffering to the invention presented at the workshop in Antibes, 1986, the second harmonic based T/R switch consists of the second harmonic generator and the fundamental/second harmonic dichroic mirror. The transmitted laser beam at the fundamental wavelength (1.064um) passes the dichroic mirror and the second harmonic generator to the telescope. The reflected beam from a target (0.53 um) passing the harmonic generator with negligible losses is reflected by the dicroic mirror to the receiver package. There are no moving parts, no time synchronization is needed. The minimal range distance is zero. In the particular application for the Keystone Project, the KTP crystal 10x10x3 millimeters and Silicon SPAD detector have been used. The T/R switch has been tested ranging to the target at the T/R switch output, retroreflector located inside the main telescope and to the calibration piers at various distances. The T/R switch box for Keystone is constructed to allow three color ranging at 0.53,0.35 and 1.54 micrometers simultaneously.

Indoor calibratiom, Kashima

BEXP x2 FRONT FACE REFLECTION 09-17-1996 04:36:09

Data file T5   coll. # 1

31   Cell width   .04   Tic =   0.400000
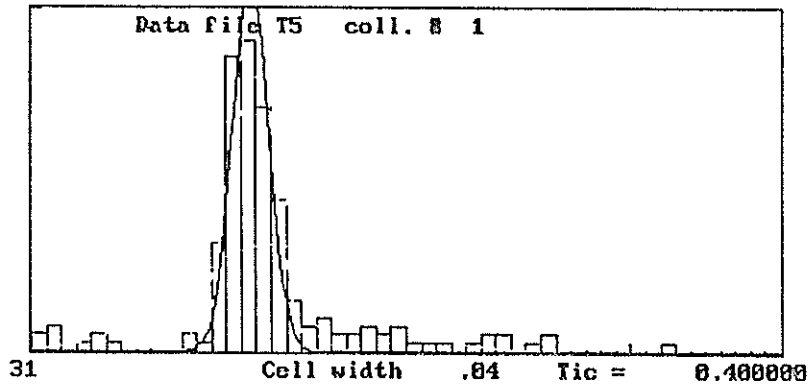
Limits	Criter.		MEAN	SIGMA	PT #
	31.000 /	33.000	31.633671	0.228239	181
	3 * SIGMA		31.597706	0.074174	151
	2.5*SIGMA		31.588030	0.054893	140
	2.0*SIGMA		31.583683	0.047358	131

Terrestrial ranging 'south pier',Kashima

4X ND + 1 A DETUNED 09-17-1996 07:45:51

Data file T15   coll. # 1

235.6   Cell width   .04   Tic =   0.320001
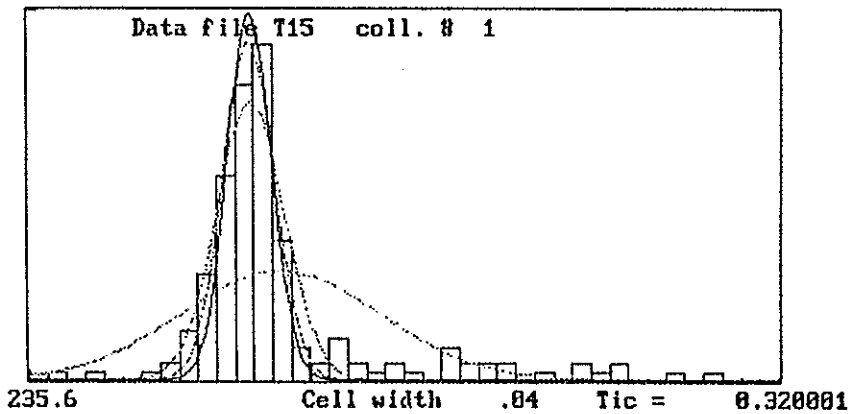
Limits	Criter.		MEAN	SIGMA	PT #
	235.600 /	237.200	236.137978	0.213180	178
	3 * SIGMA		236.071564	0.072128	153
	2.5*SIGMA		236.067642	0.055178	142
	2.0*SIGMA		236.069397	0.047269	132

480

System Automation

and

Operational Software

An assessment of the IRV model for the GPS satellites

A.T. Sinclair

Royal Greenwich Observatory, Madingley Road, Cambridge CB3 0EZ, England.

1. Introduction

The IRV format, coordinate system and force model were adopted by the Center for Space Research (CSR), University of Texas, in about 1982 as a means of providing predicted positions of Lageos for the SLR stations. They adapted the IRV system from a system previously in use at NASA. The IRV system has now been adopted for all SLR satellites, but using a higher degree and order for the lower satellites. In a paper presented at the Laser Ranging Workshop in Canberra in 1994, this author showed that the IRV model was rather inadequate for very low and very high satellites. That paper concentrated particularly on the problems for low satellites. In this paper we consider in more detail the problems for the GPS satellites, in view of the important contribution that SLR can make by providing a completely independent check on the accuracy of the precise IGS orbits.

2. Deficiencies of the IRV force model

The IRV force model is fairly basic, in order to reduce the computer time needed by the on-site numerical integration program, which is used for generating the predicted orbit. With the computer power now available this has become a minor consideration. However for most satellites in use for SLR it still serves it purpose adequately, and so it has been retained, as it would be big job to carry out any changes through the wide variety of software implementations that are in use throughout the SLR network. The IRV model is described in the Newsletter of the SLR Subcommission of the CSTG, June 1995, pp 33-36.

The technique of forming IRVs is to generate a precise orbit over a period of perhaps 2 weeks, by fitting an orbit integrated using an elaborate and precise force model to SLR data or some other data (e.g., the phases of the GPS broadcast signals or the GPS broadcast elements), and then run this orbit ahead over the prediction period, of perhaps several months. The simpler IRV orbit is then fitted to the precise orbit over periods of one day, resulting in a series of initial positions and velocities at 0 hours of each day of the prediction period. Thus an SLR station can take the position and velocity for the current day, and need only run its integrator for at most perhaps a little over 24 hours, if a pass happens to start near midnight (UT) and continue into the next day.

The simple IRV orbit will of course not give a perfect fit to the precise orbit, but for most of the SLR satellites the errors are only a few metres, which are of no consequence. The GPS satellites suffer a fairly large solar radiation pressure force which is not included in the IRV force model. Figure 1 shows a typical plot of the resulting errors of the IRV orbit, which can reach about 50 metres along-track and 40 metres radially. (The errors are discontinuous at the end of each day, but in these plots the discontinuities have been joined by a straight line.) The along-track error causes an angular displacement of the GPS satellite of less than 1 arcsec, which is of no consequence whatever from the point of view of pointing an SLR telescope at the satellite. For such high satellites the along-track error has a much reduced effect on the range, by a factor of 10 or more. Hence the range errors of the IRV orbit can be up to a little over 40 metres, requiring a

Figure 1 GPS36. Residuals of IRV orbit (1-day spans) from the precise orbit.
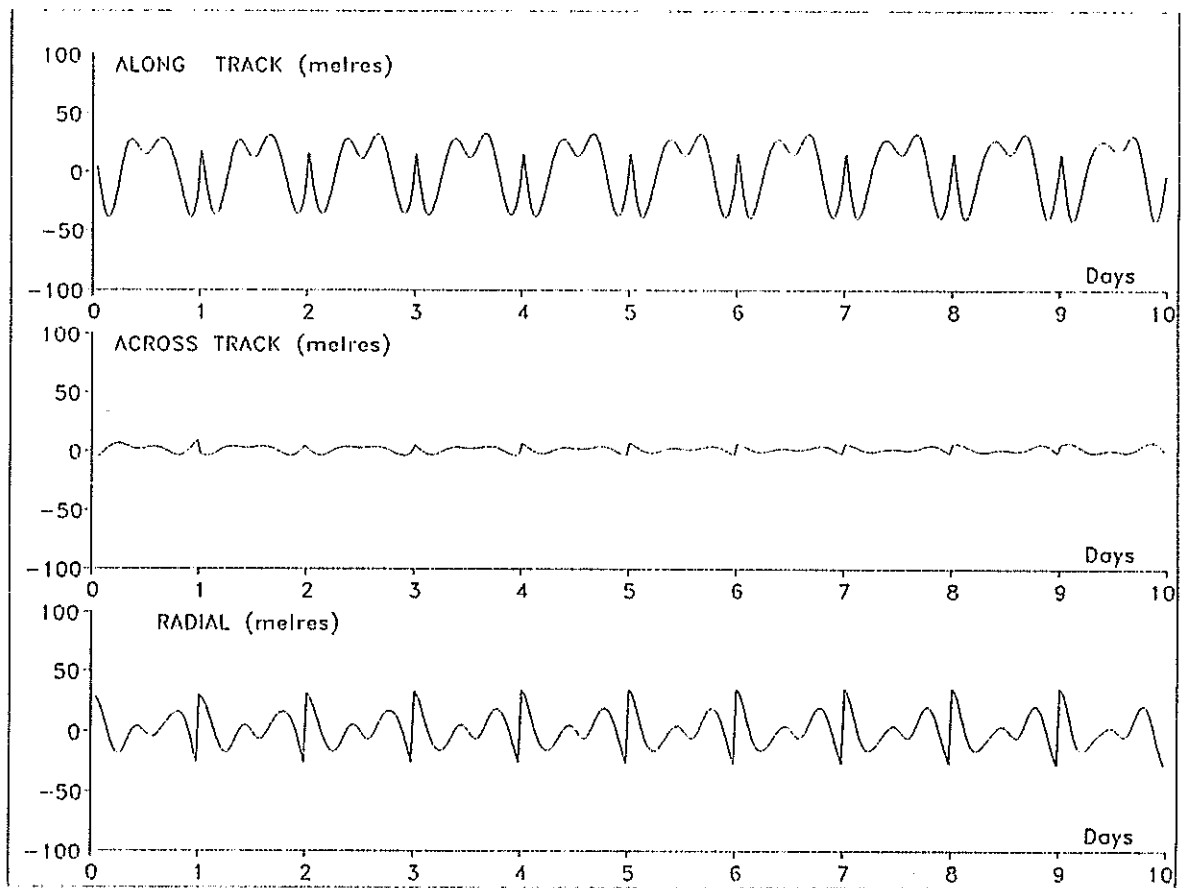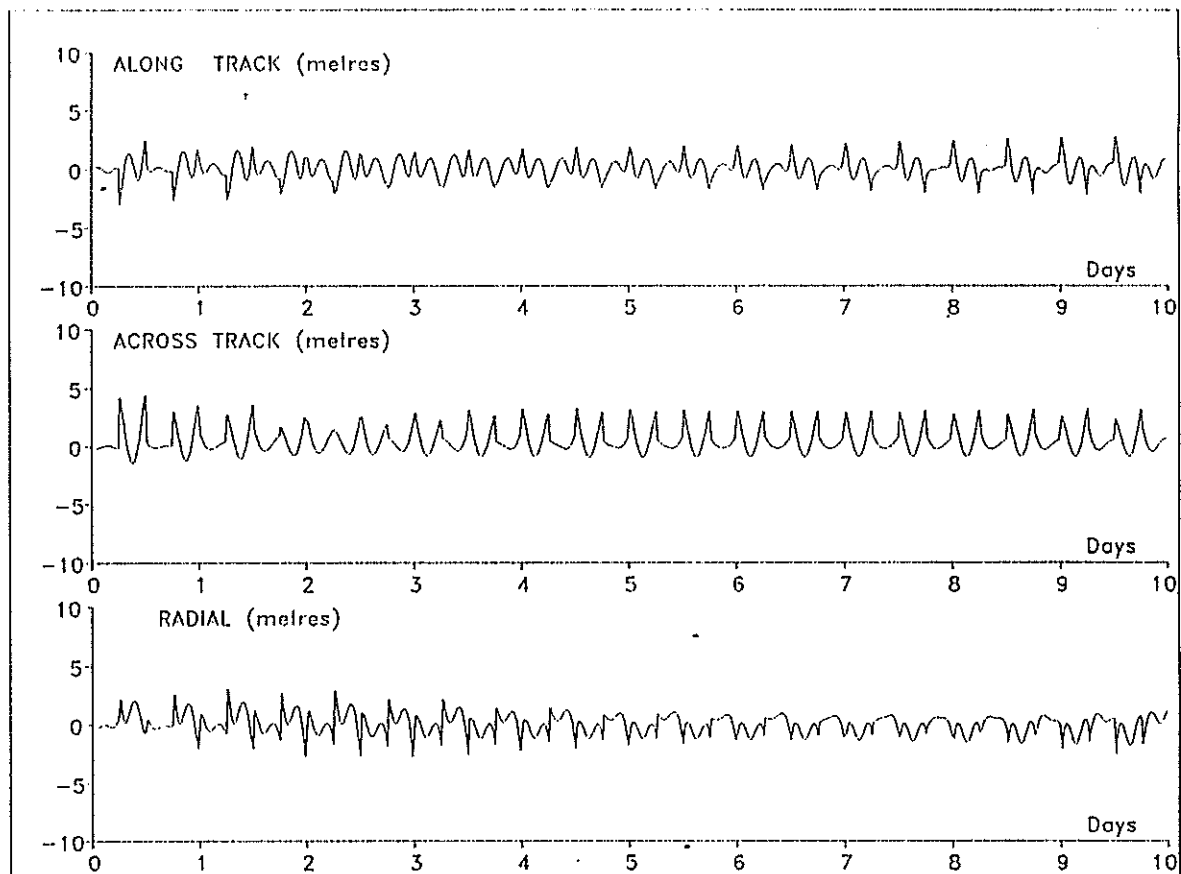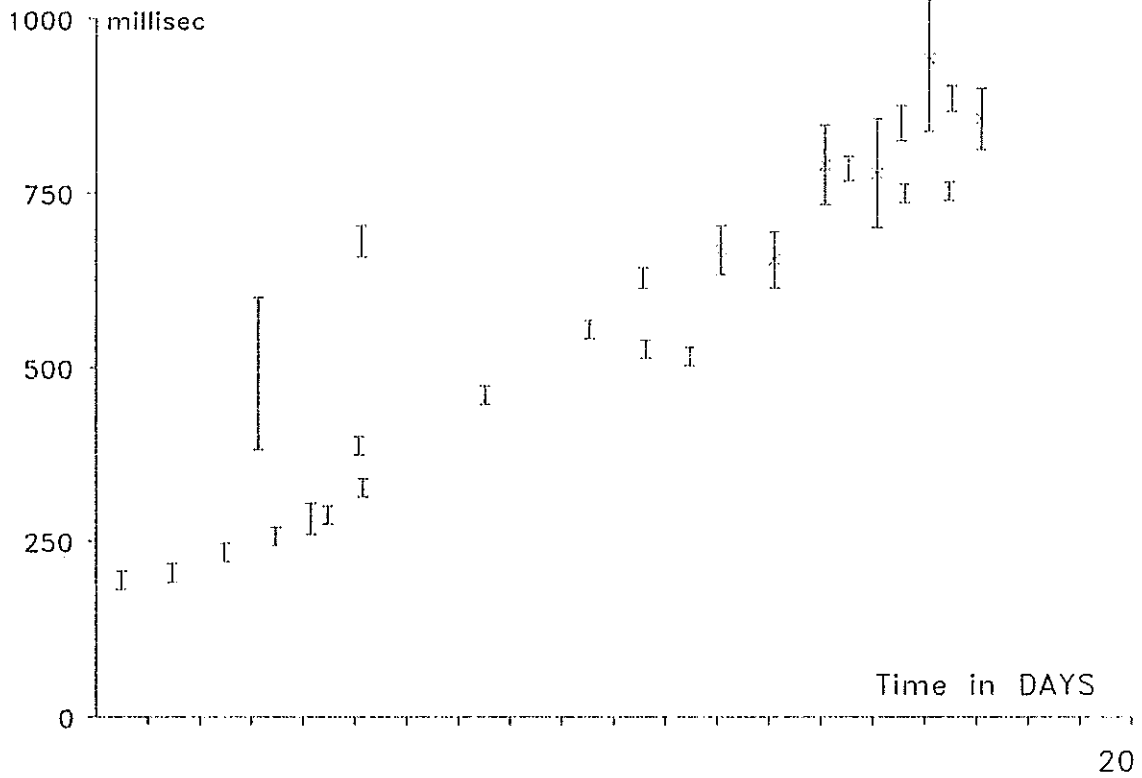

Figure 2 GPS36. Residuals of IRV orbit (1/4 day spans) from the precise orbit.
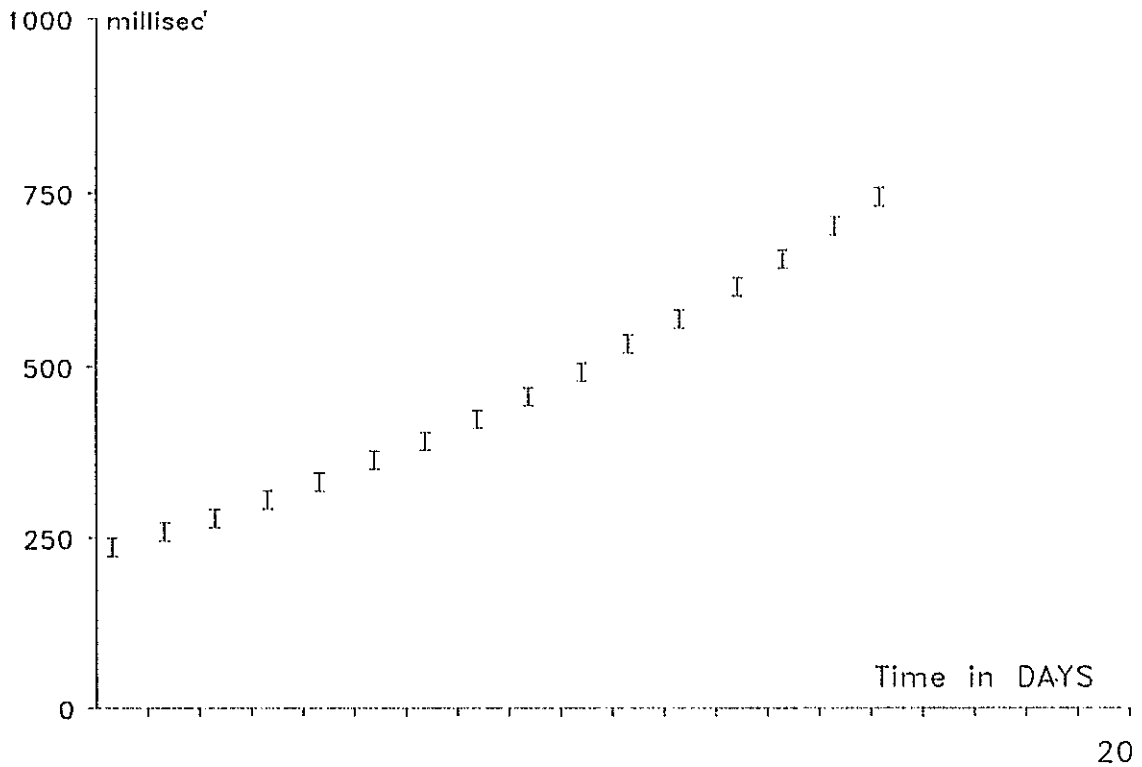
Figure 3   GPS36. Time biases determined from SLR data. Sept 1–19.
Using IRVs of 1/4 day span.

Figure 4   GPS36. Time bias of IRVs determined by comparison with
the broadcast elements. Sept 1–19.

range gate of about ± 300 ns around the predicted range. This is more than is desirable for such high satellites, in view of their very weak return signal.

In a paper presented at the Canberra Workshop (1994) this author examined several possible methods of overcoming the deficiencies of the IRV force model for low and high satellites, and concluded that a method that is simple to implement by the stations is to reduced the span over which the IRV orbit is fitted to the precise orbit. For the GPS satellites it is effective to fit over quarter-day spans, and so there will be four sets of IRVs for each day, and all the station has to do is to select the set for the quarter of the day in which it starts tracking the pass, and use this set in exactly the same way as it would use a normal set of IRVs. Figure 2 shows typical residuals of quarter-day IRVs from the precise orbit for GPS36. The residuals are much reduced, and give range differences from the precise orbit less than about 10 metres.

Of course this error of misfit of the IRV orbit to the precise orbit is only one part of the error of the predictions. There is also the larger contribution due to the degradation of the predicted orbit compared with the actual orbit. We consider this in the next section.

3. Time bias corrections

All predicted orbits deteriorate with time, with the error being primarily along-track. It has been found to be a successful scheme to determine from SLR passes as they are obtained the current along-track error, expressed as a time-bias, to fit a low order polynomial through these values, and to use this for predicting the time bias for subsequent passes. It is more convenient for the stations to use a single set of IRVs for several weeks rather than changing it frequently, perhaps as often as daily. Also it appears to be rather more successful to use a set of IRVs with a well-determined time bias history, even if the time bias is large, rather than frequent changes to new sets of IRVs, which no doubt have small time biases, but with no knowledge of the rate of change.

There are several problems with this scheme as applied to GPS satellites. For these high satellites the range measurements are only weakly dependent on the along-track error, and hence give a poor determination of the along-track error. Also the misfit error of the IRVs discussed above contributes to the difference of the range measurement from the prediction, and hence adds more scatter to the along-track error that is deduced from the range measurement. Figure 3 shows the typical scatter of time bias values for a set of IRVs for GPS36, derived from the SLR tracking data alone.

For the GPS satellites there are other sources of orbit information in addition to the SLR data. The broadcast elements give the positions of the satellites to about 5 metres accuracy. Figure 4 shows the time biases the IRVs of GPS 36 over the same time period as in Figure 3, but derived each day from the broadcast elements received by the ROGUE GPS receiver at Herstmonceux. It is seen that the overall trend is much the same as derived from the SLR data, but with considerably reduced scatter. A single GPS receiver only receives the elements that are valid for the part of the orbit in view by that receiver, and this can produce a small bias in the values determined for the time biases. However the effect is not too serious, and does not seem justify the effort of setting up an automatic system to obtain the elements from another receiver. In this way the time biases of the IRVs of GPS35 and GPS36 are determined at Herstmonceux shortly after 0^h UT each day, for both the IRVs sets produced by RGO and by ATSC, and time bias polynomials derived from these values are placed in the RGO ftp directory.

Figure 5 shows the actual range residuals that would have been obtained by the SLR stations, using the IRVs with the time bias correction derived from the broadcast elements. The range residuals reach nearly 50 metres, and so a range gate of at least ± 350 ns would be needed.

The IRVs used for this plot and for deriving the time bias polynomial used the quarter-day spans. If the standard 1-day spans are used then the range residuals are only slightly worse, perhaps reaching 60 metres. The reason for this rather insignificant improvement of the quarter-day IRVs is that the precise predicted orbit itself develops an error signature compared with the actual orbit that cannot all be absorbed by an along-track correction. Figure 6 shows this typical error signature, with the along-track component removed, after a prediction span of 31 days. Clearly, improving the fit of the IRV orbit to the precise orbit will not help a lot if the precise orbit itself has significant errors that are not absorbed by the along-track correction.

Thus the main limitation of the present system is the use of a long time span of one or two months for the predicted orbit, and in order to improve it is necessary to restrict the predictions to shorter time spans ahead.

4. Predictions derived from GPS precise orbits

There are a number of analysis groups that routinely generate precise orbits for the GPS satellites from the received phases of the broadcast coded signals. These orbits form one of the products of the International Geophysical Service (IGS). Some of these groups also form predicted orbits, valid for the current day and the next day or so. These predicted orbits are accurate to probably better than a metre, and would in effect be perfect predictions for the purpose of SLR tracking. These orbits are in the form of rectangular coordinates referred to the Greenwich meridian and true equator of date. The best thing that a station could do would be to use these directly in its prediction software, if it could manage to do so. An alternative is to fit the IRV orbit model to these predicted orbits, so that the IRVs can be used in the normal software at the stations. Inevitably this will degrade the accuracy of the predictions, due to the misfit of the IRV model. As was discussed in Section 2, this misfit can cause range residuals of up to 40 metres using the standard IRVs fitted over one-day spans. This is not significantly better than what is being achieved by the present system of long prediction spans with time bias corrections. Thus to be worthwhile it is also necessary to improve the fit of the IRVs, and as we have discussed, an easy way of implementing this is to use fit spans of a quarter-day.

The Center of Orbit Determination in Europe (CODE), at the Astronomical Institute of the University of Bern, generates several predicted orbit products, and at my request and also that of Erricos Pavlis, who was working along similar lines on behalf of the NASA stations, CODE now generate a predicted orbit spanning 72 hours, valid for the current day and the following two days, and this is placed in their ftp directory by about 17:00 each day. At RGO these are used to form IRVs for the current day and the following two days. These are fitted over 8-hour spans, starting at 0^h, 6^h, 12^h and 18^h of each day , with the 2-hour overlap being to permit tracking of a pass to continue without deterioration of accuracy if it should cross a quarter-day point. Each set of IRVs gives the position and velocity at 0^h, and so is used in exactly the same way as normal IRVs. Figure 7 shows the range residuals that would have been obtained by SLR stations tracking GPS35 for several passes in October 1996. The final pass shown, and two other outlying points, are all bad data, as has been verified by a precise orbit fit. The residuals of the good data are all less than 10 metres.

Figure 5   GPS36. Residuals of SLR data from IRVs, with time bias polynomial applied.
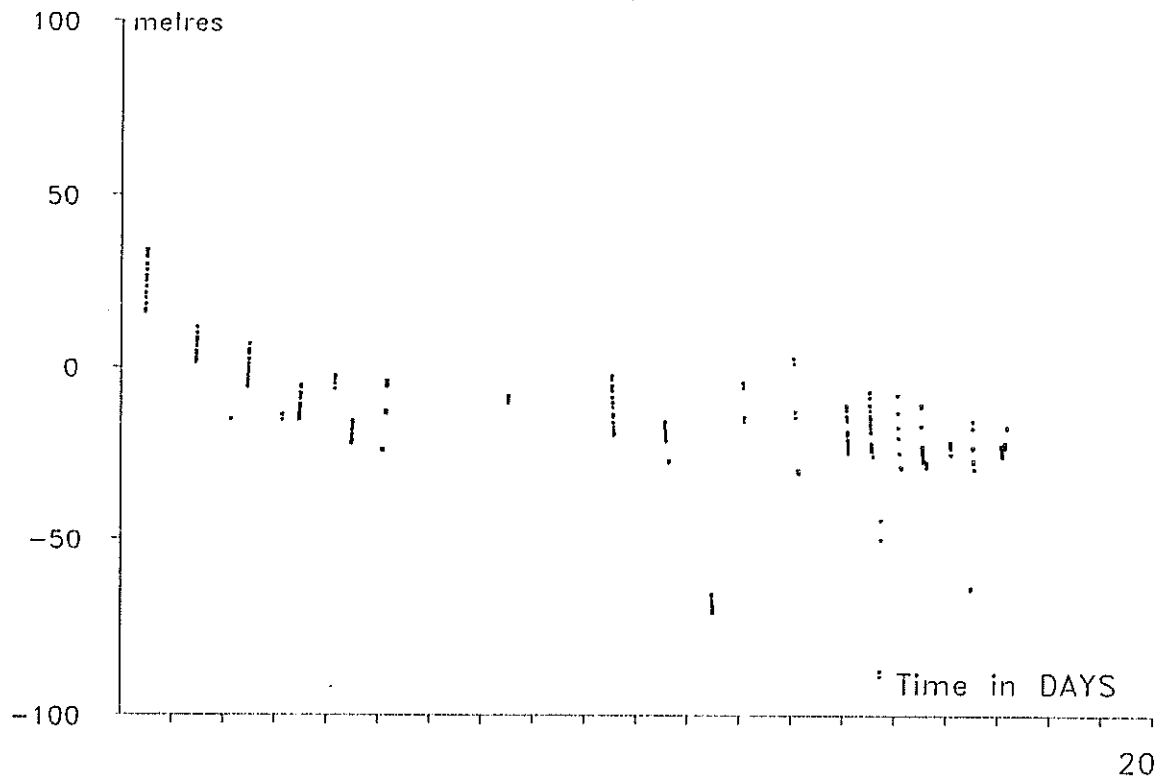
Figure 6   GPS36. Comparison of predicted orbit (with time bias applied) with the actual orbit after 31 days.
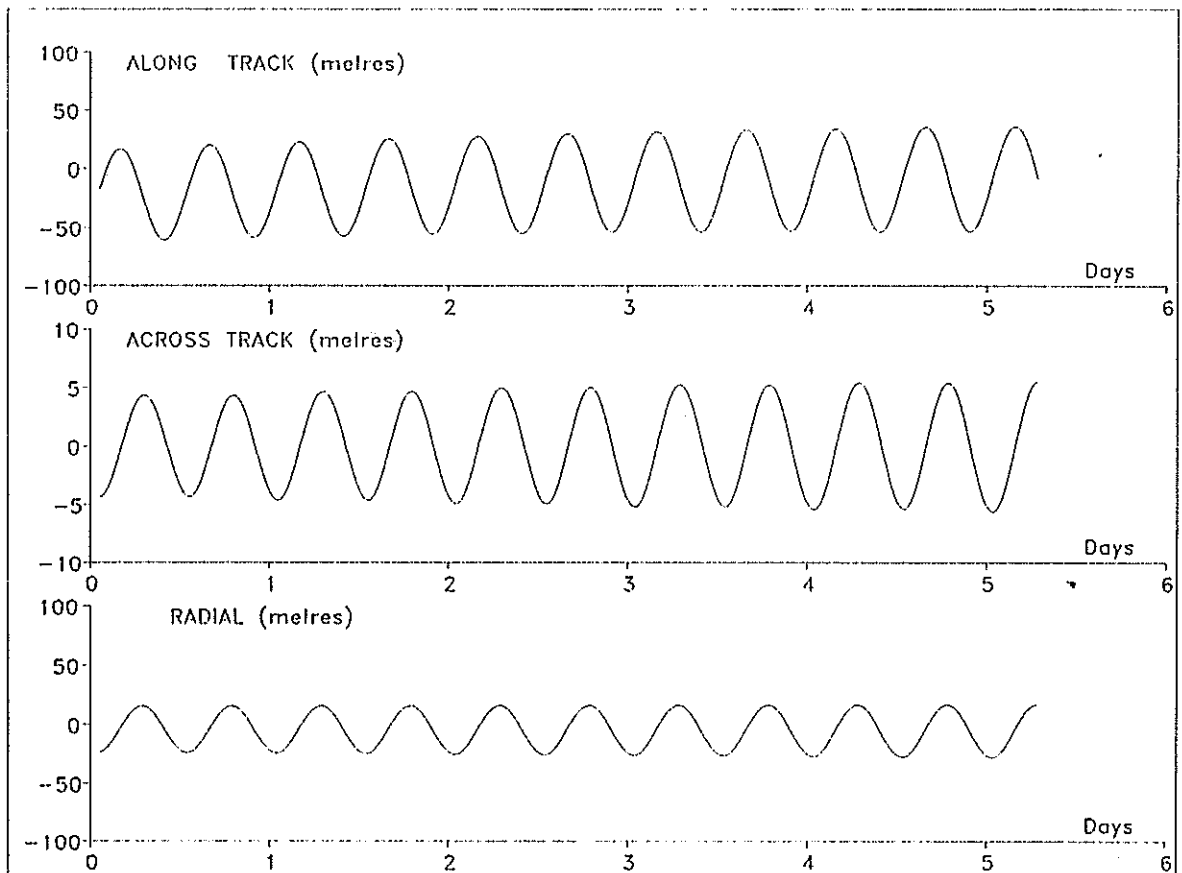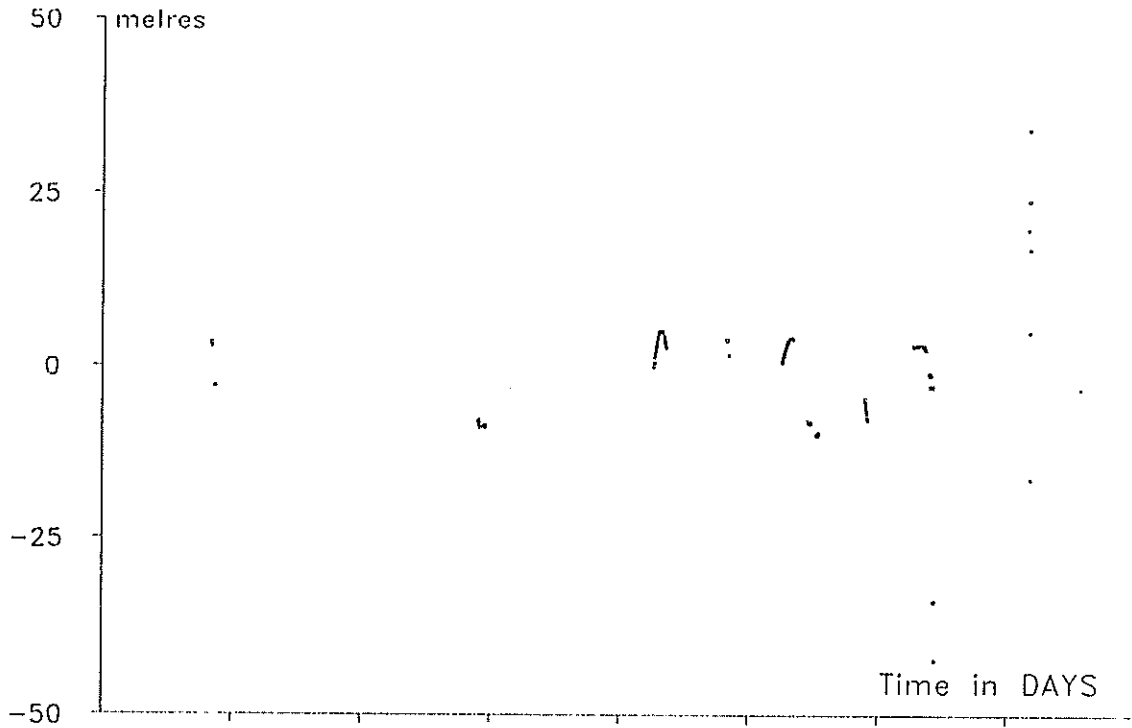
Figure 7   GPS35. Residuals of SLR data from IRVs based on
              CODE predicted orbit. 1996 Oct 17—25.

8

5. Conclusions

The present SLR prediction system for GPS satellites of using IRVs fitted over one-day spans, and running the predicted orbits ahead for a month or so, with time-bias corrections determined daily from the broadcast elements, is fairly close to the best that can be done using such long prediction spans. This system gives a negligible pointing error of less than 1 arcsec, but requires a range gate width of about ± 450 ns.

Improvement can be made by using predictions over a short time span, and the best short term predictions available are those generated using GPS data as contributions to the IGS. The best way to use these would be directly, but if they are used indirectly using the IRV system then is necessary to improve the misfit error of the IRV model, such as by using fits over quarter-day spans.

The GFZ/D-PAF Orbit Prediction System with Emphasis on the Low Flyer GFZ-1

Z. Chen, R. König
GeoForschungsZentrum Potsdam (GFZ),
Div.I: Kinematics and Dynamics of the Earth,
GFZ/D-PAF c/o DLR, Oberpfaffenhofen, Germany

Abstract: Since July 1991, the GFZ/D-PAF orbit prediction system provides regular orbit predictions for several satellites to the SLR community. During this five years practice many improvements towards automatisation and quality have been achieved in the system. The orbit prediction accuracy is increasing continuously. A short report about the orbit prediction quality for ERS-2 as well as for the completed ERS-1 and Meteor-3 tracking campaigns is given.

The launch of GFZ-1 in April 1995 has challenged the orbit prediction system to be capable in handling extremely low flying satellites. A drag function in addition to the tuned IRVs was designed and introduced to the SLR community to account for the missing drag model in the SLR station integrators. Although the modelling of the Earth's gravity field and of the surface forces in GFZ-1 precise orbit determination is quite difficult, the quality of GFZ-1 orbit predictions is sufficient for tracking purposes; experiences made in the last one and a half years are reported. The dependence of the orbit prediction quality on the solar activity and its predictions is investigated. Also demonstrated are the benefits of concentrations of laser stations (f.i. in Europe) for such difficult missions in case of poor weather periods for the maintenance of the acquisition loop.

1. Introduction

Since the launch of ERS-1 in July 1991, the GFZ/D-PAF orbit prediction system provides orbit predictions for several satellites to the SLR community. The orbit predictions consist of tuned IRVs, SAO-elements, the time bias functions, and the drag functions. The time bias function accounting for the along-track errors of the orbit predictions was introduced to ERS-1 for the first time, meanwhile it is well established. The drag function was dedicated to GFZ-1 to account for along-track error residuals due to the missing drag model in the station integrator which are not covered by IRV tuning.

During five years of experience many improvements have been achieved in the system. The accuracy of orbit predictions has been increasing continuously enabling the prolongation of orbit prediction lengths. For satellites at altitudes like that of ERS-1/-2 or higher, the orbit prediction generation runs fully automatically. For new tracking campaigns, the acquisition loop can be installed within a few days. For the low flyer GFZ-1, orbiting at the lowest altitude ever in SLR history, orbit predictions in appropriate quality for tracking have been generated and distributed for one and a half years.

The following chapter 2 deals with the quality of orbit predictions for the ERS-2 and for the completed ERS-1 and Meteor-3 tracking campaigns. The generation of GFZ-1 orbit predictions

which is more complicated will be discussed in chapter 3. A brief survey of these missions may be found in *Kramer* [1992]. Finally, a conclusion is given in chapter 4.

2. Quality of Orbit Predictions for ERS-1/-2 and Meteor-3

The ERS-1 laser tracking campaign started on July 17th, 1991, and terminated on July 28th, 1996. During the five years 20,201 laser passes from 69 stations have been acquired. The generation of ERS-1 orbit predictions is described in *König* [1989]. *Figure 1* displays the along-track errors of ERS-1 orbit predictions including time bias function updates. The vertical dashed lines in *Figure 1* indicate orbit manoeuvre events. The major part of large inaccuracies can be found after the manoeuvres due to under- or overperformance of the manouevres. In the first 250 days the accuracy was heavily affected by frequent manoeuvres and also by large solar and geomagnetic activity. The overall along-track error can be assessed at about 12 ms for the whole tracking campaign or at about 5-6 ms after the initial 8 months period of high solar and geomagnetic activity.
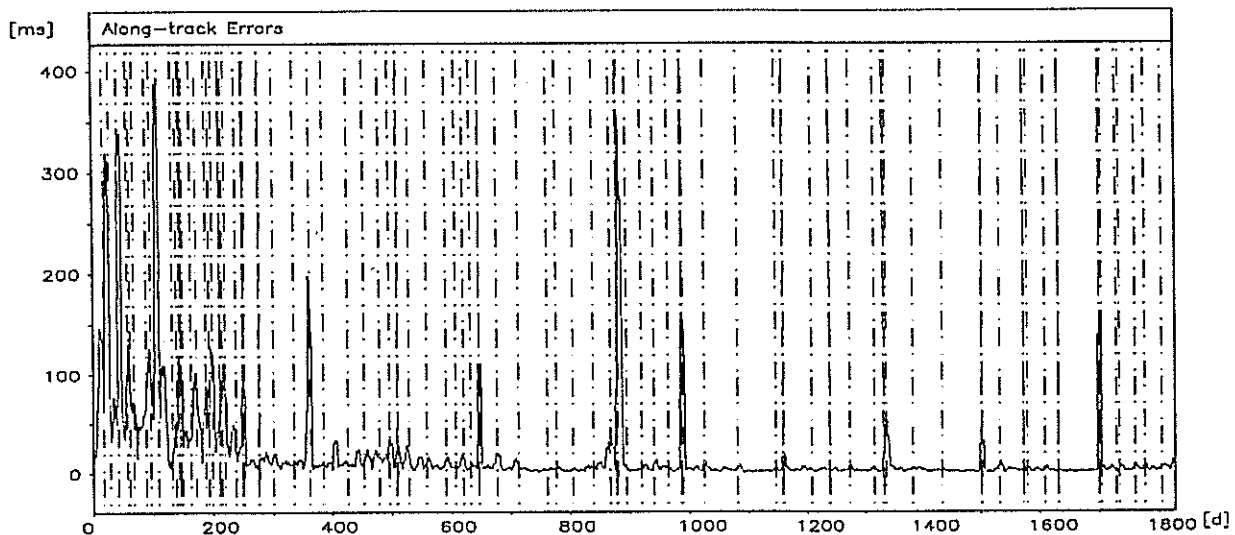
Figure 1: ERS-1 Orbit Prediction Accuracy in Along-Track Direction (91/07/17 - 96/07/27).

The steady accuracy improvements are traced back to the following facts:

- the improvements in the modelling of Earth's gravity field and of surface forces,
- the decline of the solar and geomagnetic activity as shown in *Figure 2*,
- software upgrades for precise orbit determination.

Due to the increasing accuracy, the prediction period could be expanded from 1 week at the beginning to 3 weeks at the end of the tracking campaign.

The ERS-2 satellite was launched on April 21st, 1995. The procedure of orbit prediction generation is the same as for ERS-1. Since the launch 7,200 passes from 42 stations have been acquired. The quality of the orbit predictions is very similar to ERS-1 during their common operation phase. Since the along-track error development is small in general, each

orbit prediction can be maintained for about 3 to 4 weeks if no manoeuvre happens. It is also sufficient to update the along-track error estimate by 1 to 2 time bias functions per week. However, it could become necessary to increase the frequency of orbit prediction updates again, when solar and geomagnetic activity move into their cyclic maximum expected for the year 2001.
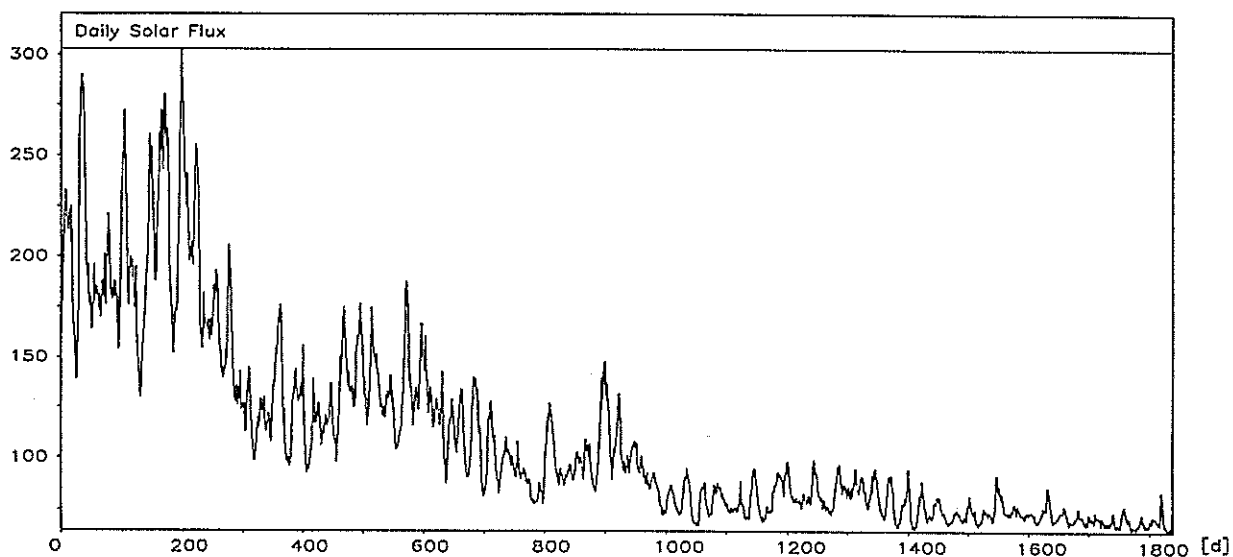

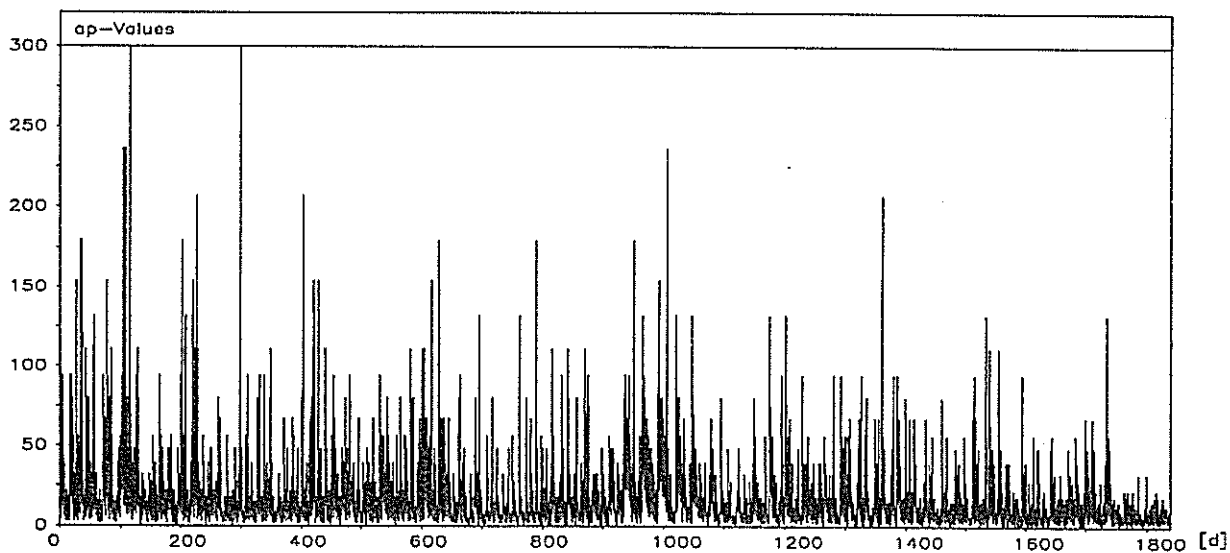*Figure 2a:* Solar Activity (91/07/17 - 96/07/27).

Figure 2b: Geomagnetic a_p Indices (91/07/17 -96/07/27).

The Meteor-3 laser tracking campaign in support of the PRARE validation covered the period from January 1994 to October 1995. Due to the relative high altitude of the spacecraft, the orbit prediction generation could be carried out in a more relaxed way than in case of ERS-1/-2. Typically orbit predictions were released after 3 weeks and time bias functions at weekly frequency. The along-track errors of the orbit predictions including time bias function updates

remained in general below 10 ms.

3. GFZ-1 Orbit Predictions

GFZ-1 is a pure laser satellite orbiting since April 19th, 1995. The primary mission goal is to improve Earth's gravity field models. Therefore a very low altitude, even the lowest altitude orbit ever flown by geodetic missions, was chosen for GFZ-1. *Dow* [1996] reports to the United Nations on the usefulness of new targets including GFZ-1 for the development of new gravity field models.

GFZ-1 is a very fast moving target. For a tracking station, its apparent angular velocity is about twice as large as for ERS-1/-2. With decreasing orbital altitude and increasing solar activity, the drag pertubations exerted on GFZ-1 will dynamically increase in the course of the 4 years mission. This will put more stringent demands on acquisition procedures in the future. More details about GFZ-1 orbit perturbations and prediction problems can be found in *König, Chen* [1994] and *Reigber, König* [1994]. *König et al.* [1996] give an extended report on various mission aspects.

GFZ-1 data analysis is exclusively based on laser tracking data. Since the launch more than 2,733 laser passes have been acquired. *Figure* 3 displays the number of tracking passes per week. Obviously the tracking record is highly correlated with Northern daylight or nighttime tracking phases, because

- most GFZ-1 tracking stations are located on the Northern hemisphere,
- GFZ-1 visibility changes with an approximately monthly period from daytime to nighttime; Daytime acquisition phases for the Northern hemisphere concur with nighttime phases for the Southern hemisphere and vice versa,
- particular, during sparse tracking periods usually concurrent with Northern daylight phases, orbit prediction accuracy degrades preventing quick acquisition in blind tracking mode.

The GFZ-1 orbit predictions are generally derived from laser tracking data. Only in case of lack of tracking data, the orbit predictions are based on AFIT (Air Force Institute of Technology, Massachusetts) twoline-elements. GFZ-1 orbit predictions consist of tuned IRVs, SAO-elements, time bias functions, and drag functions. The drag function [*Chen, König, 1995*] in addition to the tuned IRVs was designed and introduced to the SLR community in time before the GFZ-1 tracking campaign commenced. By using the drag function, the daily deviation in along-track direction of the integrated orbit based on the tuned IRVs can be reduced from about 22 ms to approximately 7 ms in these days of low solar activity. In the upcoming high solar activity phase, the application of the drag function will become indispensable.

It was found that using 1-2 days worths of laser tracking data for orbit predictions yields better orbit prediction qualities than 3-4 days worths of data do. This may be deduced from a corruption of atmospheric density scaling by older data. Nevertheless, the along-track orbit
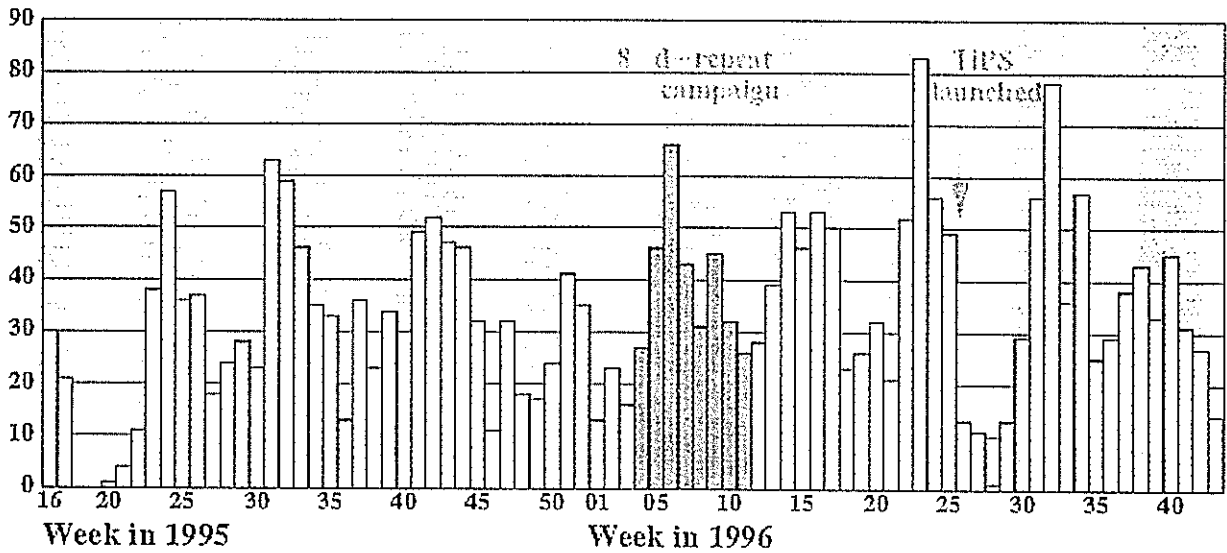
Number of Passes

Figure 3: Acquired GFZ-1 SLR Passes per Week.

prediction errors rise very fast (see Table 1). Therefore orbit predictions are generated twice per week in order to keep the orbit prediction accuracy at a sufficient level.

	1d	2d	3d	4d
Time Bias [ms] Development	20 ± 20	73 ± 70	152 ± 119	207 ± 144

Table 1: Along-Track Error Development of GFZ-1 Orbit Predictions (95/04/21 - 96/10/14)

GFZ-1 orbit predictions have been updated by time bias functions once per day, if necessary and possible twice per day. The time bias functions are determined not only from recent tracking data, but also from orbit comparisons using recent 1-2 day tracking data and updated solar and geomagnetic activity parameters. This method is useful because

- very short passes at low elevations yield instable time bias estimates,
- the GFZ-1 orbit responds very quickly to changes in solar and geomagnetic activity.

The assessment from both methods gives more confidence in the time bias function which is finally delivered to the SLR community. However, in periods when only sparse tracking data are available, both methods may yield very different, even opposite trends for the time bias development. In such a case, a definitive decision does not come easy.

Figure 4 displays the along-track errors of GFZ-1 orbit predictions including time bias function updates since launch. Extremly large errors occured mostly during operation downtimes. In general the along-track errors size at the level of 20-25 ms during the first two

days and at 45 ms after 3 to 4 days as depicted in Table 2.

	1d	2d	3d	4d
along-track errors [ms]	± 20	± 25	± 44	± 46

Table 2: Accuracy of GFZ-1 Orbit Predictions Including Time Bias Function Updates (95/04/21 - 96/10/14).

In general the accuracy seems to be appropriate for daylight ranging. It should be stressed here that the drag function must be applied by the stations, because its extreme values reach up to 50 ms.
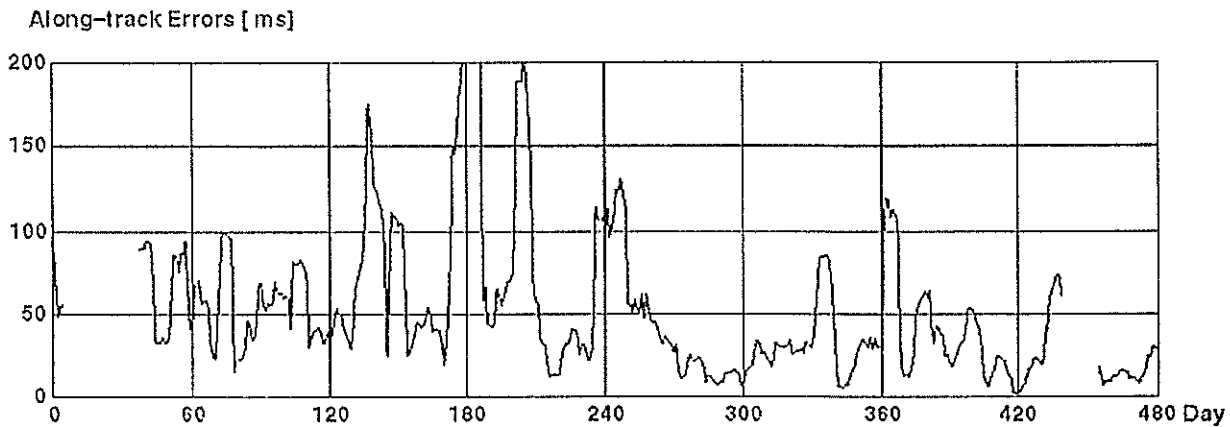
Along-track Errors [ms]

Figure 4: Accuracy of GFZ-1 Orbit Predictions from Laser Tracking (7 day moving mean, 95/04/20 - 96/10/17).

Figure 4 shows two large gaps in May 1995 and in July 1996. In May 1995, the satellite went into its first daylight visibility phase on the Northern hemisphere. Due to missing tracking support from the Southern hemisphere at that time and due to the rather new and demanding acquisition requirements, the tracking record went to zero. The orbit predictions had to be derived from AFIT twoline-elements. Tracking commenced again in June as the satellite moved back to nighttime visibility on the Northern hemisphere.

In the beginning of July 1996 very poor weather governed whole Europe. Due to unknown reasons GFZ-1 was not acquired in other parts of the world. So the orbit predictions had to be generated from AFIT twoline-elements again. The accuracy of GFZ-1 orbit predictions based on twoline-elements is much poorer than from laser tracking data deduction. The along-track errors range from 100 - 200 ms to 1 s. Also the radial and cross-track errors may reach hundreds of meters. Daylight tracking in view of this poor quality becomes immense difficult.

The quality of GFZ-1 orbit predictions is highly dependent on the quick transfer of Q/L data from the tracking stations to the data analysis center. Some European SLR stations route the GFZ-1 Q/L data immediately after acquisition directly to GFZ/D-PAF. At CDDIS a special facility was set up to allow hourly access of GFZ-1 Q/L data from some NASA stations . So all in all a considerable amount of GFZ-1 Q/L data can be analyzed within a few hours after acquisition.

One of the dominant factors for the limited quality of GFZ-1 orbit predictions originates from the uncertainties of the atmospheric models. Therefore the influences of solar and geomagnetic activity predictions on GFZ-1 orbit predictions in July and August 1995 were investigated. During the investigation period, the geomagnetic and solar activities are part of the low phase of the solar cycle. The accuracies of the activity predictions are good enough for orbit predictions for satellites at higher altitudes like ERS-1/-2. For GFZ-1, serious problems in orbit prediction accuracy result. GFZ-1 orbit predictions are extremly sensitive to fluctuations of the geomagnetic a_p indices and to the prediction errors of the a_p values and of the solar flux. Any peaks in the a_p series as well as small errors can give rise to large time bias deviations. A practical way to keep the time bias within certain limits is to keep the orbit prediction period short and to update the predictions as frequent as possible.

Figure 5 displays the GFZ-1 tracking record separately in three regional groups: Europe, North America, and Southern hemisphere plus Pacific. The geographic distribution of GFZ-1 passes is quite varying. More than half of all passes were tracked by a few European stations, at a level of about 3 passes per day. About 1 pass per day was acquired from North America or from the Southern hemisphere plus Pacific. Tracking from Asia came quite sporadically. The concentration of tracking passes from Europe turned out beneficial for such a difficult mission like GFZ-1. During sparse tracking phases (may be due to daylight ranging or due to bad weather conditions) a continental cluster of stations trying to range nearly simultaneously at the same target helps to increase the possibility that one of the stations can acquire the satellite. Thus at least the acquisition loop can be maintained. In general the European stations contribute to a better timely coverage of the observation of GFZ-1's orbital motion. However, from the viewpoint of precise orbit determination and Earth's gravity field modelling, it is highly desirable that the tracking records from other parts of the world would increase to 2-3 passes per day. All stations capable of GFZ-1 tracking are kindly asked to consider the possibility of putting highest priority on GFZ-1 tracking whenever feasible.

4. Conclusions

ERS-2 high quality orbit predictions are nowadays generated automatically. In contrast, GFZ-1 orbit predicition generation still needs large personal engagement. However, GFZ-1 orbit prediction accuracy is increasing thanks to the installation of fast data transfer procedures, due to frequent orbit analyses and due to improvements in analysis techniques. The accuracy in along-track direction remains sufficient for daylight ranging as long as a minimum of about 2 passes per day are acquired. To meet the daylight ranging accuracy requirements the drag function must be applied by the stations. The most important factor for keeping the orbit prediction accuracy at a high level, is the fast and continuous flow of tracking data, especially during the Northern daylight tracking phases. From the viewpoint of precise orbit and gravity
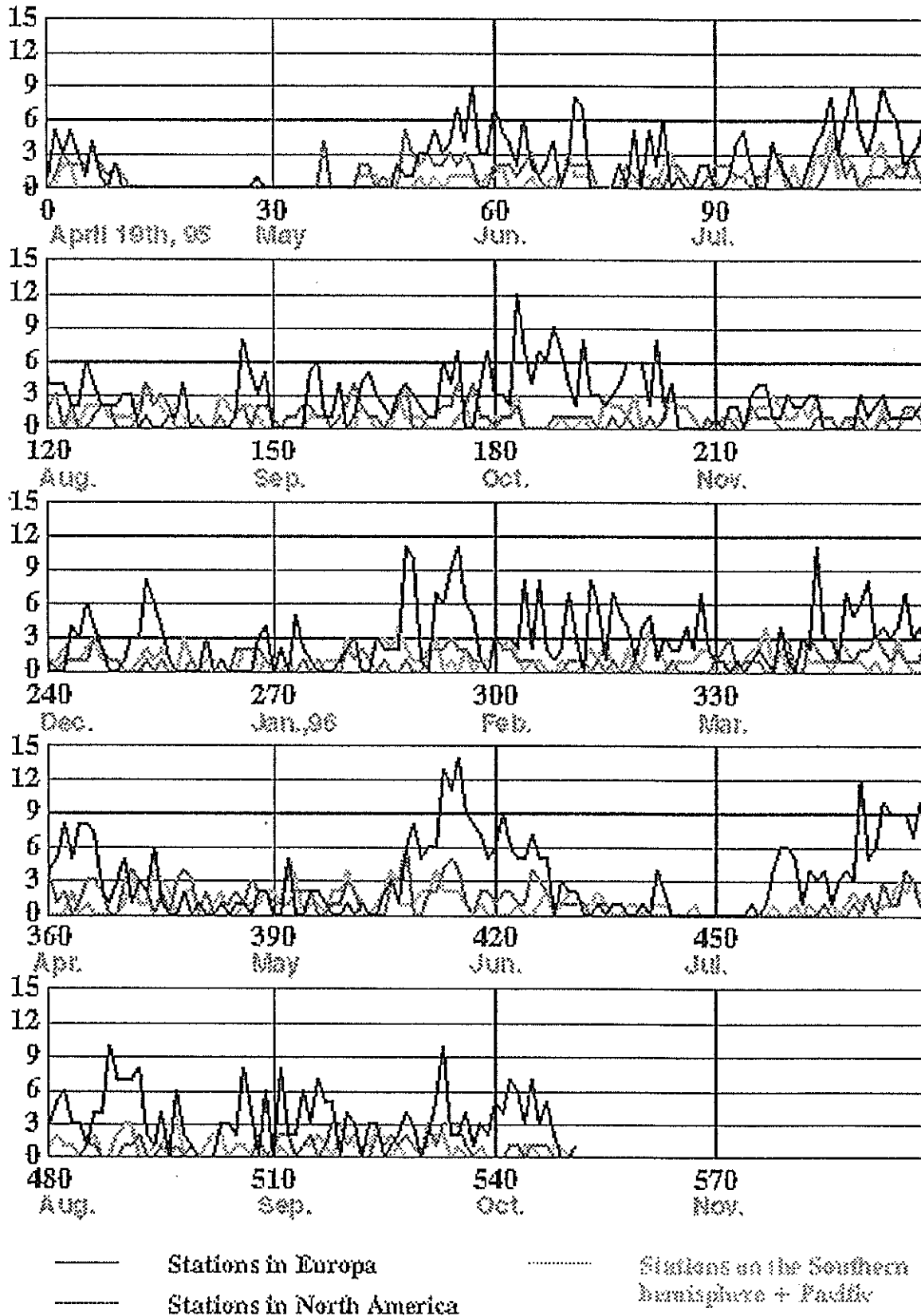
No. of Passes

Figure 5: Distribution of GFZ-1 Laser Passes in three regional Groups.

field restitution, a more geographically balanced and a more timely continuous distribution of the tracking data would be desirable.

References

Chen, Z., and R. König: *Drag function for GFZ-1 IRVs*. In: Sinclair, A.T. (Ed.), Proceedings of Annual Eurolas Meeting, Munich, March 1995, pp. 85-88, Royal Greenwich Observatory, Cambridge, 1995

Dow, J.M.: *COSPAR Report to UN for 1996*. ESA/ESOC, 1996.

König, R.: *Predictions for ERS-1*. In: Veillet, C. (Ed.), Proceedings of 7th International Workshop on Laser Ranging Instrumentation, pp. 385-392, Grasse, 1989

König, R., Bode, A., Chen, Z., Grunwaldt, L., Neubert, R., Reigber, Ch., Schwintzer, P.: *The GFZ-1 Mission: Design, Operations and First Results*. In: Scientific Technical Report STR96/09, GeoForschungsZentrum Potsdam, Germany, 1996.

König, R., and Z. Chen: *Probable Qualities of GFZ-1 Orbit Predictions*. In: Proceedings of 9th International Workshop on Laser Ranging Instrumentation, Canberra 1994, in print.

Kramer, H.J.: *Earth Observation Remote Sensing, Survey of Missions and Sensors*. Springer, Berlin, 1992.

Reigber, Ch., and R. König: *Gravity and Atmosphere Aspects by the Low Altitude Target GFZ-1*. In: Proceedings of 9th International Workshop on Laser Ranging Instrumentation, Canberra 1994, in print

Matera Laser Ranging Observatory System

Tenth International Workshop on Laser Ranging

Shanghai Observatory, Chinese Academy of Sciences

November 11-15, 1996

AlliedSignal Technical Services Corp.
Michael Selden

*Italian Space Agency (ASI)*
Dr. Giuseppe Bianco

Abstract:

The Matera Laser Ranging Observatory (MLRO) system is being developed by AlliedSignal Technical Services Corporation for the Agenzia Spaziale Italiana. (ASI). The contract began at the beginning of 1994 and is entering the integration phase of its development. A brief system description and a report of progress will be discussed.

Introduction

This paper is divided into three parts. The first section will discuss the MLRO system characteristics and some of its features. The second section will discuss the current status of the major subsystems and the overall stage of the system development. The third section will describe some of the measures which have been taken to improve both the quality of the delivered product and the overall engineering process. ATSC and the ASI have worked closely together to ensure there is a clear understanding of the system requirements, its design, and to make the development process as open as possible to create a partnership relationship with the goal of producing the finest system possible.

System Characteristics and Features

The MLRO is a no-compromise, multi-mission system designed to perform satellite / lunar laser ranging while supporting advance (experimental) development as well as astronomical applications. It is designed to facilitate highly-automated calibrations, diagnostics and verification testing to ensure that the system will continue to operate at a high performance level. The MLRO is expected to not only meet, but exceed its specifications. A diagram showing the MLRO subsystems is illustrated in Figure 1.
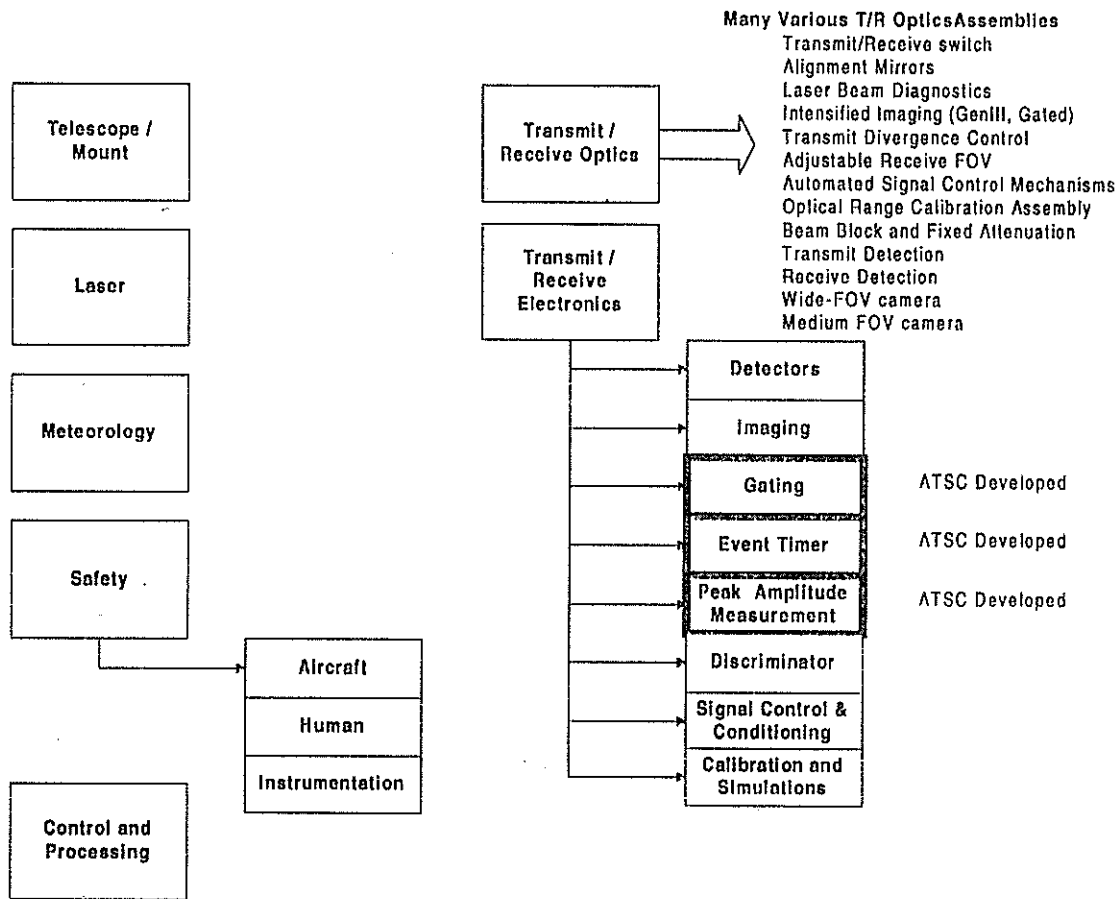
Figure 1: Primary MLRO Subsystems and Assemblies

The MLRO employs a multi-photoelectron approach to SLR. It is a large-aperture system with an MCP-PMT detection approach using a 100 milli-Joule per pulse transmit energy at a 10 Hz repetition rate. It has been designed to accommodate a two-color ranging upgrade and can be easily adapted to accommodate a multi-kHz repetition rate if desired.

Telescope

The MLRO telescope is a 1.5 meter astronomical-quality telescope (manufactured to ATSC-specification by Contraves USA). The primary mirror exhibits a $\lambda/66$ wavefront error and the secondary exhibits a $\lambda/88$ wavefront error. The system uses a full-aperture, common transmit/receive approach and will have an internal calibration target attached to the end of the telescope for real-time system delay measurements. The telescope encoder system resolution is 0.03 arcsecond and the repeatability was measured at the sub-arcsecond level. A picture of the telescope is illustrated in Figure 2.
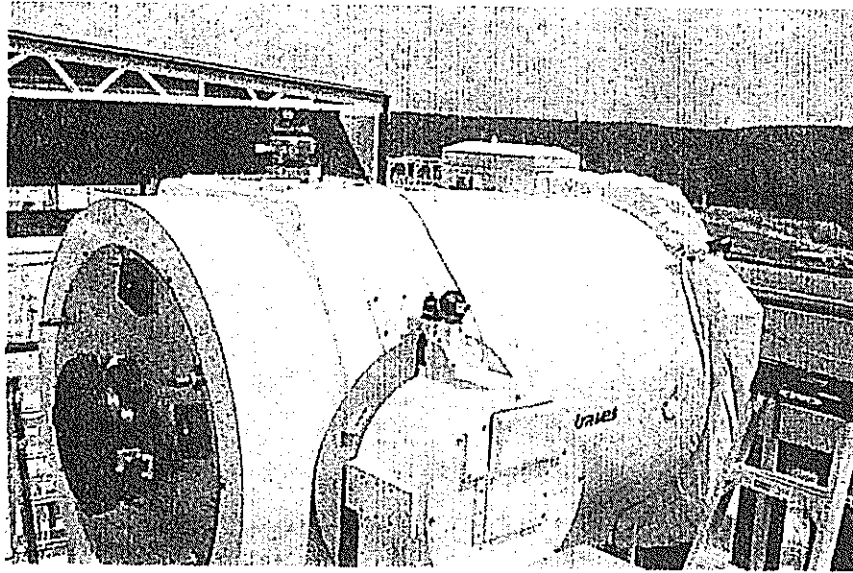
Figure 2: MLRO Telescope installed in the STALAS building at GGAO

Laser

The MLRO laser is a hybrid using a Lightwave CW mode-locked laser to produce a 100 MHz pulse train from which a pulse may be selected. This pulse is switched into a Continuum regenerative amplifier, then switched-out at a precisely-determined time. The output pulse travels through two power amplifiers. The resultant pulse is < 50 ps duration with 100 mJ energy. A picture illustrating the laser is presented in Figure 3.
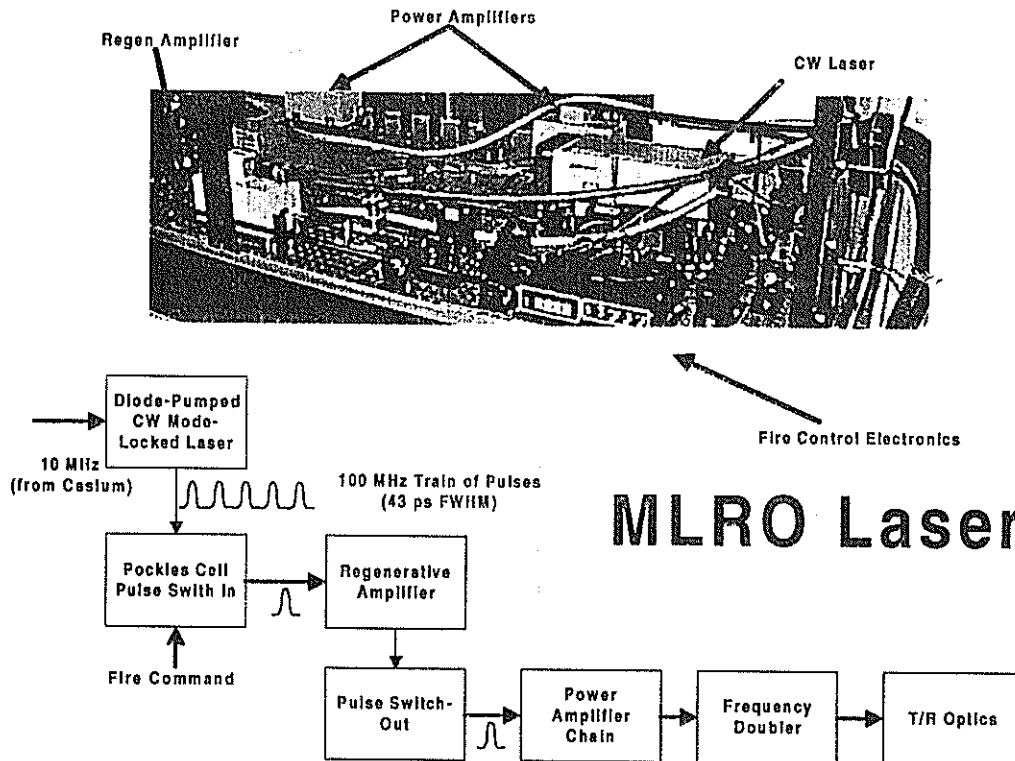

Figure 3: MLRO Laser